

Probing the effects of external irradiation on low-mass protostars through unbiased line surveys[★]

J. E. Lindberg^{1,2★★}, J. K. Jørgensen¹, Y. Watanabe³, S. E. Bisschop¹, N. Sakai³, and S. Yamamoto³

¹ Centre for Star and Planet Formation, Niels Bohr Institute and Natural History Museum of Denmark, University of Copenhagen, Øster Voldgade 5-7, DK-1350 Copenhagen K, Denmark

² NASA Goddard Space Flight Center, Astrochemistry Laboratory, Mail Code 691, 8800 Greenbelt Road, Greenbelt, MD 20771, USA
e-mail: johan.lindberg@nasa.gov

³ Department of Physics, The University of Tokyo, 7-3-1 Hongo, Bunkyo-ku, Tokyo, 113-0033, Japan

Received March 30, 2015; accepted September 7, 2015

ABSTRACT

Context. The envelopes of molecular gas around embedded low-mass protostars show different chemistries, which can be used to trace their formation history and physical conditions. The excitation conditions of some molecular species can also be used to trace these physical conditions, making it possible to constrain for instance sources of heating and excitation.

Aims. We study the range of influence of an intermediate-mass Herbig Be protostar. We also study the effect of feedback from the environment on the chemical and physical properties of embedded protostars.

Methods. We followed up on an earlier line survey of the Class 0/I source R CrA IRS7B in the 0.8 mm window with an unbiased line survey of the same source in the 1.3 mm window using the Atacama Pathfinder Experiment (APEX) telescope. We also studied the excitation of the key species H₂CO, CH₃OH, and *c*-C₃H₂ in a complete sample of the 18 embedded protostars in the Corona Australis star-forming region. Radiative transfer models were employed to establish abundances of the molecular species.

Results. We detect line emission from 20 molecular species (32 including isotopologues) in the two surveys. The most complex species detected are CH₃OH, CH₃CCH, CH₃CHO, and CH₃CN (the latter two are only tentatively detected). CH₃CN and several other complex organic molecules are significantly under-abundant in comparison with what is found towards hot corino protostars. The H₂CO rotational temperatures of the sources in the region decrease with the distance to the Herbig Be star R CrA, whereas the *c*-C₃H₂ temperatures remain constant across the star-forming region.

Conclusions. The high H₂CO temperatures observed towards objects close to R CrA suggest that this star has a sphere of influence of several 10 000 AU in which it increases the temperature of the molecular gas to 30–50 K through irradiation. The chemistry in the IRS7B envelope differs significantly from many other embedded protostars, which could be an effect of the external irradiation from R CrA.

Key words. stars: formation – ISM: individual objects (R CrA) – ISM: molecules – astrochemistry – radiative transfer

1. Introduction

The molecular composition of the envelopes of deeply embedded low-mass protostars can be used to trace their history and physical conditions. As a result of observations of these sources as well as of chemical modelling, the relevance and origin of many of these molecules are now relatively well understood (see e.g. Herbst & van Dishoeck 2009). The studied molecules include organic, silicon- and sulphur-bearing, and deuterated species (e.g. Blake et al. 1994; van Dishoeck et al. 1995; Schöier et al. 2002). Jørgensen et al. (2004) correlated the presence and abundance of nine molecular species, discovering strong correlations between some species and anti-correlations between others. This enabled constructing an empirical chemical network of molecular species.

Data from spectroscopy observations of molecular emission lines can also be used to trace the physical properties of protostellar envelopes. The rotational temperature of the molecular gas, which can be used as a proxy for the kinetic temperature of the gas given certain assumptions, can be measured by excitation diagrams of the observed molecules (see e.g. Goldsmith & Langer 1999; Jørgensen et al. 2005b). By comparing the rotational temperatures of different molecular species, insights about their distribution and formation paths can be gained. Isotopical ratios can also be used as tracers of formation history.

During the past decade, the existence of an inner ($R \lesssim 100$ AU) hot region in the envelopes of deeply embedded low-mass protostars with a chemistry similar to that of high-mass hot cores has been proposed. These dense ($n > 10^6$ cm⁻³) regions are referred to as hot corinos (Ceccarelli 2004), and they are characterised by the presence and relatively high abundance of complex organic molecules such as CH₃OH, CH₃OCH₃, and CH₃OCHO (Bottinelli et al. 2004a, 2007; Jørgensen et al. 2005a). High angular resolution interferometric observations show that complex organics are often concentrated in the inner $\lesssim 1''$ ($R \lesssim 50$ – 100 AU) of low-mass protostars (e.g. Bot-

[★] Based on observations with the Atacama Pathfinder EXperiment (APEX) telescope. APEX is a collaboration between the Max Planck Institute for Radio Astronomy, the European Southern Observatory, and the Onsala Space Observatory.

^{★★} NASA Postdoctoral Program Fellow.

tinelli et al. 2004b; Kuan et al. 2004; Jørgensen et al. 2005a; Bisschop et al. 2008; Maury et al. 2014) – most likely reflecting that they evaporate from the icy dust grains at high temperatures ($T \gtrsim 100$ K). IRAS 16293-2422 is considered as the prototypical hot corino, but at least three more such sources have been discovered.

Sakai et al. (2008, 2009b) found that the chemistry towards two deeply embedded low-mass protostellar sources was distinctly different from that of the hot corinos. The two sources L1527 and IRAS 15398-3359 are dubbed warm carbon-chain chemistry (WCCC) sources. They are characterised by comparably high abundances of long carbon-chain molecules such as HC_3N , C_4H , and C_6H , and at the same time by low or moderate abundances of complex organic species. The difference between the chemical properties observed towards hot corinos and WCCC sources could be an effect of different collapse timescales (Sakai et al. 2009b; Sakai & Yamamoto 2013). This mechanism has been verified by chemical modelling (Hassel et al. 2008).

The presence of complex organic molecules in low-mass star formation is, however, not unique to the hot inner regions of deeply embedded protostars. The spectral signatures of several complex organic molecules have recently been detected towards the prestellar core L1689B, with temperatures ~ 10 K (Bacmann et al. 2012). Complex organic molecules have also been found towards protostellar outflows such as that of L1157, with similarly low temperatures (Arce et al. 2008).

The transitional Class 0/I protostar R CrA IRS7B is located in the R CrA cloud (NGC 6729) within the Corona Australis (CrA) star-forming region. At a distance of 130 pc (Neuhäuser & Forbrich 2008), this is one of the nearest low-mass star-forming regions, making it ideal for the study of the envelope and core chemistry of the individual sources by single-dish (sub)mm observations. The population of young stellar objects (YSOs) in the region was inventoried through multi-wavelength studies by Peterson et al. (2011), who identified 116 YSOs and classified them according to their spectral slope following the definitions of Greene et al. (1994). Out of these sources, 14 were found to be Class I sources or younger, and 5 were found to be flat-spectrum sources (transitional sources between Class I and Class II). Most of these deeply embedded sources are concentrated in the R CrA cloud, within a few 1000 AU from the Herbig Be star R CrA. Lindberg & Jørgensen (2012) found large-scale H_2CO emission in the region, exhibiting gas temperatures > 30 K. The high temperatures, which cannot be explained by internal radiation from the low-mass stars, were suggested to be a result of external irradiation from R CrA.

Watanabe et al. (2012) presented an unbiased line survey of R CrA IRS7B in the 0.8 mm window and a few scans in the 0.7 mm window, using the Atacama Submillimeter Telescope Experiment (ASTE) 10 m telescope. These observations showed enhancements of the radicals CN and C_2H , which trace photon-dominated regions (PDRs). Furthermore, neither any complex organic molecules characteristic for hot corino chemistry (except the ubiquitous CH_3OH) nor any long carbon chains characteristic for WCCC were detected. High-resolution Atacama Large Millimeter/submillimeter Array (ALMA) observations towards R CrA IRS7B also indicate an absence or unusually low abundances of the complex organic species CH_3CN and CH_3OCH_3 (Lindberg et al. 2014a).

This paper complements the work by Watanabe et al. (2012) by adding an unbiased line survey in the 1.3 mm window, which increases the number of detected molecular species as well as the number of molecular transitions in many of the excitation

diagrams, and thus also the range of E_u in those diagrams. We also investigate other similar protostellar sources in Corona Australis to study the spatial variations of the chemical and physical properties in the star-forming region. This paper finally uses radiative transfer modelling of the emission from several of the species to establish molecular abundances for comparison with other sources.

Section 2 describes the observational methods and data reduction strategy. Section 3 describes the spectra resulting from the observations, and Sect. 4 discusses rotational diagrams, radiative transfer models, and isotopologue ratios of many of the observed molecules. Section 5 discusses the large-scale heating in the CrA region and the chemistry of the envelopes. Section 6 lists our conclusions.

2. Observations

2.1. APEX unbiased line survey of R CrA IRS7B

The observations were carried out with the Atacama Pathfinder Experiment 12 m telescope (APEX; Güsten et al. 2006) in position-switching mode in August and October 2010. The frequency range between 217.9 GHz and 245.5 GHz was covered with 17 spectral setups on the SHeFI (Swedish Heterodyne Facility Instrument) receiver APEX-1 (Vassilev et al. 2008). This survey was unbiased in the sense that it covered a wide spectral range without targeting any particular molecular species. In addition, we used parts of the APEX-1 data that were observed by Lindberg & Jørgensen (2012) in April 2010 to cover the range between 217.2 GHz and 217.9 GHz. All observations were centred at the sub-mm/IR point source (Class 0/I YSO) IRS7B in the R CrA cloud (see Table 1 for coordinates). The two sets of observations have an overlap around 218 GHz, which we used to investigate the calibration accuracy. The small differences found in the line intensities can all be explained with a calibration uncertainty $\leq 10\%$.

For all new scans reported in this work, rms levels between 21 and 35 mK channel^{-1} were reached with velocity resolutions ranging between 0.17 km s^{-1} and 0.15 km s^{-1} (122 kHz), corresponding to rms levels of 8–14 mK $(\text{km s}^{-1})^{-1}$. The scan from Lindberg & Jørgensen (2012), which here was used to cover 217.2 GHz–217.9 GHz, is not as deep as the new data presented here. It has an rms level of 84 mK channel^{-1} , or 35 mK $(\text{km s}^{-1})^{-1}$.

Because of unstable quasi-sinusoidal baselines in the observed spectra (see Vassilev et al. 2008), we had to perform relatively advanced baseline fitting after carefully identifying channels containing any spectral line emission. The exact method used for this baseline fitting is described in Appendix A. The calculation and subtraction of baselines were performed using our own scripts as described in the appendix, but Gaussian line fitting and calculations of line strengths were afterwards performed using the GILDAS CLASS package¹. To account for some smaller features left after the baseline subtractions, a zeroth-order baseline was subtracted locally around all fitted lines before the extraction of line parameters.

All line intensities are given in the T_{mb} (main beam brightness temperature) scale, which means that the antenna temperatures T_A^* are corrected with the APEX main beam efficiency $\eta_{\text{mb}} = 0.75$. The beam sizes of the observations range between

¹ GILDAS CLASS (Continuum and Line Analysis Single-dish Software) is developed by the IRAM institute, Grenoble, France, and can be downloaded from <http://www.iram.fr/IRAMFR/GILDAS>.

Table 1. Observed sources and the rms of the observations in the APEX surveys of CrA. See Table 2 for spectral window parameters.

Source name ^a	RA (J2000.0)	Dec (J2000.0)	YSO Class ^b	rms [mK (km s ⁻¹) ⁻¹]		
				1.4 mm	0.9 mm	0.8 mm
IRS7B	19 01 56.40	-36 57 28.1	I	11 ^c	13	40
CrA-46	18 55 56.32	-37 00 07.1	Flat	19
CrA-3	18 59 43.92	-37 04 01.1	Flat	19	32	...
CrA-5	19 00 15.55	-36 57 57.7	I	10	21	27
LS-RCrA1	19 01 33.56	-37 00 30.3	Flat	20	22	...
Haas4	19 01 40.67	-36 56 04.9	Flat	16	20	...
IRS2	19 01 41.56	-36 58 31.2	I	7	14	...
IRS5A	19 01 48.03	-36 57 22.2	I	11	18	36
IRS5N	19 01 48.46	-36 57 14.7	I	11	15	38
IRS1	19 01 50.68	-36 58 09.7	I	12	20	34
IRS7A	19 01 55.32	-36 57 21.9	I	...	14	38
CrA-24	19 01 55.60	-36 56 51.1	I	20	20	36
SMM 2	19 01 58.54	-36 57 08.5	I	20	15	36
CXO42	19 02 01.96	-36 54 00.0	I	8	17	...
CrA-44 ^d	19 02 58.67	-37 07 35.9	I	12	19	...
CrA-33	19 03 01.03	-37 07 53.4	Flat	19	16	...
VV CrA	19 03 06.80	-37 12 49.1	I	9	12	...
CrA-37	19 03 55.24	-37 09 35.9	I	20	15	...

Notes. ^(a) We use the notation of Peterson et al. (2011) for all sources except IRS5A, IRS5N, and SMM 2, for which we use the notation of Lindberg & Jørgensen (2012) and Lindberg et al. (2014b). These are referred to as CrA-19, CrA-20, and CrA-43, respectively, by Peterson et al. (2011). ^(b) Assigned from the spectral index α (Peterson et al. 2011). Class I sources are Class I or younger. ^(c) Only partially covered by the IRS7B line survey. The observations do not cover 216.1–217.2 GHz, and the 217.2 GHz–217.9 GHz portion is covered only at a lower S/N level (37 mK (km s⁻¹)⁻¹). ^(d) Also known as IRAS 32.

26'' and 29'' depending on the observed frequency. All errors given in this work are at the 1 σ level if not otherwise stated.

As a complement to the APEX observations, we use the spectral lines detected in the ASTE 0.8 mm and 0.7 mm observations of Watanabe et al. (2012). This enables a more accurate excitation analysis of the various molecular species thanks to the larger range of E_u in the used transitions. The beam size of these ASTE observations ranges between 21'' and 23'' for the 0.8 mm window, and between 16'' and 17'' for the few lines in the 0.7 mm window. For the 0.8 mm window in particular, the beam size is quite similar to that of the APEX observations, meaning that the two sets of observations cover roughly the same spatial region. From previous SMA observations we know that the spatial extent of the molecular line emission is similar to or larger than these beams (Lindberg & Jørgensen 2012). For this reason, and to be consistent with Watanabe et al. (2012), we thus calculated beam-averaged column densities. When combining data points with different beam sizes in excitation diagrams, this means that we assumed that the beam-averaged column densities are similar in both beams, or in other words, that the emission is extended and uniform.

2.2. Unbiased survey of H₂CO, CH₃OH, and c-C₃H₂ in CrA

In addition to the unbiased line survey of IRS7B discussed above, IRS7B and 17 other protostellar sources within the Corona Australis star-forming region were observed in more narrow frequency bands using the APEX telescope. The selected sample consists of all sources defined as Class I sources (or younger) or flat-spectrum sources in the survey of YSOs in CrA conducted by Peterson et al. (2011). Only the faint Class I source CXO34 was excluded because of its close proximity to the two

Table 2. Observational parameters of the APEX observations (this work; IRS7B line survey and CrA source survey) and the ASTE line survey of IRS7B (Watanabe et al. 2012).

Window	Frequency range [GHz]	Beam size	
		[']	[AU]
IRS7B survey	217.2–245.5 ^a	26–29	3300–3800
	1.4 mm	29	3700
	0.9 mm	19	2400
	0.8 mm	17	2200
ASTE 0.8 mm	332.0–364.0	21–23	2700–3000
ASTE 0.7 mm	435.0–437.0	17	2300
ASTE 0.7 mm	459.2–461.2	16	2100

Notes. ^(a) The 217.2 GHz–217.9 GHz portion is only covered at a low S/N level. ^(b) In most sources only 361.8–364.3 GHz, due to high noise levels and baseline issues in the upper sideband.

much stronger sources IRS7A and IRS7B, which would cause confusion. The observed protostellar sources are shown on a map in Fig. 1, and their positional data are listed in Table 1. The observations were performed in up to three frequency setups: 216.1–220.1 GHz (1.4 mm), 336.9–340.9 GHz (0.9 mm), and 361.8–365.8 GHz (0.8 mm), see also Table 2. The frequency setups were chosen to cover a wide E_u range of H₂CO, CH₃OH, and c-C₃H₂ lines. The 1.4 mm window was observed with the SHeFI APEX-1 receiver and the other two windows with the SHeFI APEX-2 receiver (Vassilev et al. 2008). Observations in the higher-frequency windows were only executed for sources with a significant number of detected lines (see Table 1 for de-

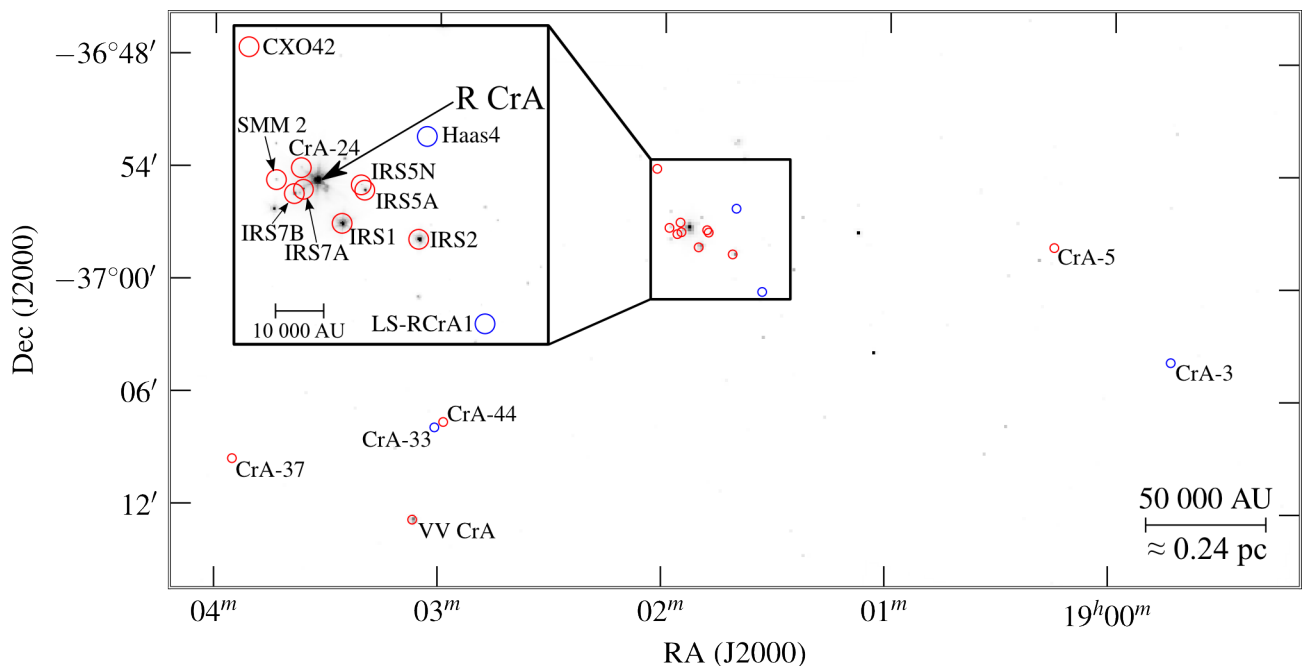


Fig. 1. Overview of the observed sources in the H_2CO , CH_3OH , and $c\text{-C}_3\text{H}_2$ survey. The circles show the APEX beam size in the 1.4 mm window. Red circles denote Class 0/I objects and blue circles are flat-spectrum sources. CrA-46 is located $\sim 40'$ (~ 1.5 pc) west of the right edge of the plot. The inset shows a zoom-in of the region around R CrA enlarged by a factor ~ 2 . The greyscale background is a *Spitzer* 4.5 μm image. (A colour version of this plot is available in the online journal.)

tails on observed spectral windows). The observations were carried out in September and November 2011. This survey is unbiased in the sense that it covers (nearly) all embedded sources in CrA, albeit only in a limited number of spectral setups, targeting certain molecular species.

All line intensities are given on the T_{mb} scale. The APEX main beam efficiency $\eta_{\text{mb}} = 0.75$ for the 1.4 mm window and $\eta_{\text{mb}} = 0.73$ for the 0.9 mm and 0.8 mm windows. The unsmoothed spectra have 76 kHz channel widths (corresponding to 0.10 km s^{-1} for the 1.4 mm window, 0.067 km s^{-1} for the 0.9 mm window, and 0.063 km s^{-1} for the 0.8 mm window). The rms levels when smoothed to 1 km s^{-1} channels are listed in Table 1. In the 1.4 mm window, the rms level is between $7 \text{ mK (km s}^{-1})^{-1}$ and $20 \text{ mK (km s}^{-1})^{-1}$, which can be compared to a noise level of $11 \text{ mK (km s}^{-1})^{-1}$ for the 1.4 mm window in the IRS7B survey (above).

Like in the observations described in Sect. 2.1, the spectra in this survey also have unstable baselines, and the same baseline corrections as were used for the IRS7B data were applied (see Appendix A). The 0.8 mm band was particularly affected by unstable baselines with both wide and narrow features. In the lower sideband of the 0.8 mm observations these effects could mostly be accounted for, but in the upper sideband the features were too strong to make proper use of the spectra except for in smaller stable chunks. Thus, only a few spectral lines were identified in this sideband, and then only in the sources where the strongest line emission was found.

3. Results

3.1. IRS7B line survey

We detect 102 spectral lines in the IRS7B line survey between 217.2 GHz and 245.5 GHz. We successfully identify 87 of the detected lines, and the identifications correspond to 16 molecular species (25 if counting isotopologues separately). The online

database Splatalogue² was used for line identification. The detected spectral lines and their parameters are listed in Table B.1 in Appendix B. A compressed version of the APEX spectrum of the IRS7B observations can be found in Fig. 2, and a full spectrum is available in Appendix C (Figs. C.1–C.8).

In Fig. 3, we compare the line emission observed towards IRS7B in a window around 227 GHz with the emission detected towards a typical high-mass hot core and a typical low-mass hot corino source. This simplistic comparison shows that the hot corino bears more resemblance to the hot core than to IRS7B.

Many of the species detected towards IRS7B were previously detected in the ASTE survey (Watanabe et al. 2012), but we detect six molecular species not detected in that survey: HNCO , H_2CCO , CH_3CCH , CH_3CHO , CH_3CN , and HC_3N . HC_3N was previously detected in SMA/APEX observations (Lindberg & Jørgensen 2012), but the five other species have, to the best of our knowledge, not previously been detected towards IRS7B. The CH_3CN and CH_3CHO detections are only tentative: For CH_3CN , only two faint spectral lines are seen, and the two lines at 239.133 GHz and 239.138 GHz, expected to be of similar intensity, are not detected. For CH_3CHO , three lines are detected at $3\text{--}6\sigma$ levels, but three lines at 219.820 GHz, 232.691 GHz, and 235.684 GHz, expected to be at least as strong, are non-detected. We also detect some isotopologues not seen in the ASTE survey: ^{13}CN , C^{15}N , ^{13}CO , C^{18}O , ^{13}CS , C^{33}S , and DNC .

We find that all identified spectral lines have LSR velocities in the range $5.0\text{--}6.6 \text{ km s}^{-1}$ (median 5.7 km s^{-1}). The line widths show a somewhat larger variation, with the lowest values around 1 km s^{-1} for species like ^{13}CN , $c\text{-C}_3\text{H}_2$ and CH_3CCH , and the highest values above 6 km s^{-1} for CS and CO . The median line width for the non-blended lines to which a Gaussian could be fitted is 2.0 km s^{-1} .

Of the 102 detected lines, 15 are unidentified. A handful of these are on the $3\text{--}5\sigma$ level, and could thus be flukes, but a few

² <http://splatalogue.net/>

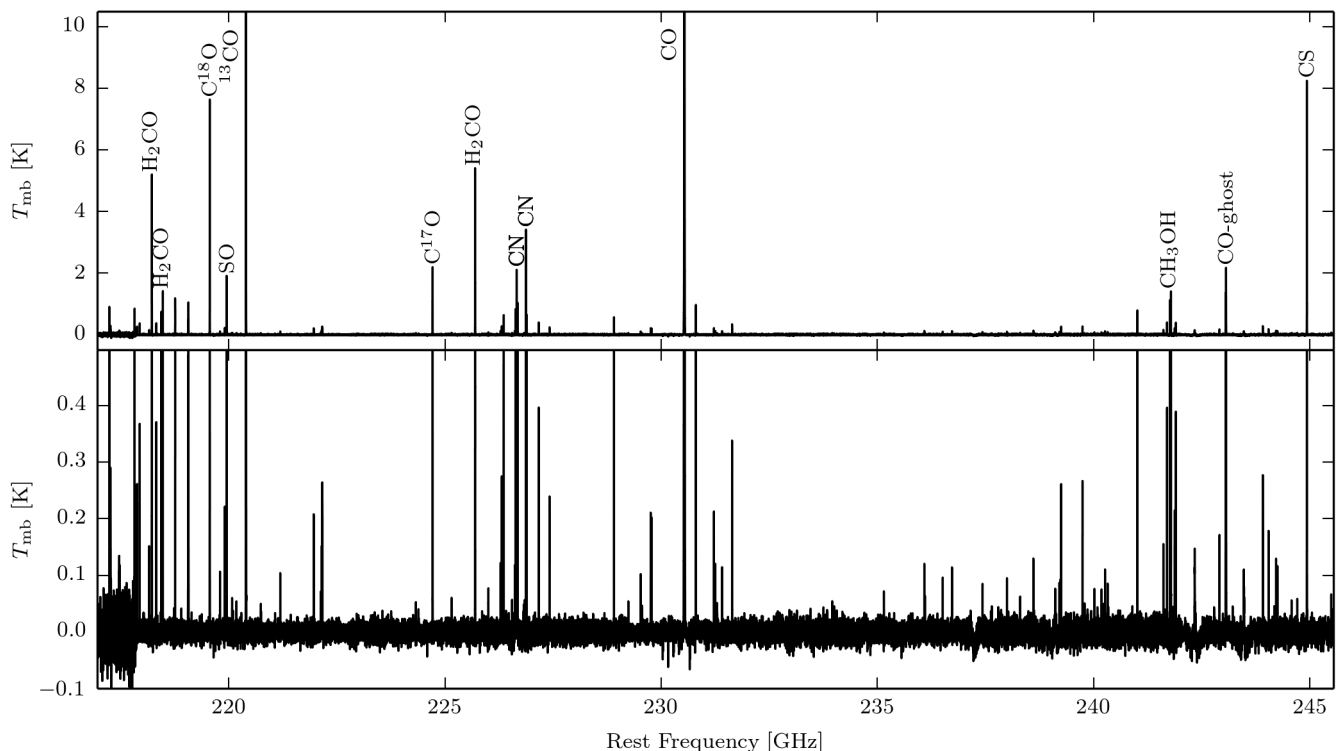


Fig. 2. 1.3 mm spectrum of IRS7B, cut at 10.5 K (top panel) and 0.5 K (bottom panel). A high-resolution spectrum can be found in Appendix C.

U lines are strong. In Appendix E we demonstrate our attempts to identify these U lines.

3.2. H_2CO , CH_3OH , and $c\text{-C}_3\text{H}_2$ survey in CrA

Of the 18 targeted sources in this survey, only CrA-46 shows no spectral line emission at all. Towards an additional four sources, only CO isotopologues were detected, but towards the remaining 13 sources several different molecular species were detected. The species that were detected towards at least one of the sources in this source survey are H_2CO , H_2^{13}CO , CH_3OH , $c\text{-C}_3\text{H}_2$, C^{18}O , C^{17}O , DCO^+ , HC^{18}O^+ , SiO , SO , ^{34}SO , CN , ^{13}CN , C^{15}N , C^{34}S , C_2D , DCN , HNC , and H_2CS . The detected spectral lines and their parameters are listed in Tables B.2–B.22 in Appendix B, except for the IRS7B parameters, which are given together with the results of the IRS7B line survey in Table B.1. The spectra can be found in Figs. D.1–D.41 in Appendix D.

With the exception of SiO , which traces shocked gas at high absolute velocities relative to the protostar, all spectral lines have LSR velocities in the range $4.6\text{--}6.6\text{ km s}^{-1}$ towards all sources where spectral lines are detected (CrA-24 and SMM 2 have two velocity components, however, which is discussed below). This confirms the conclusion of Peterson et al. (2011) that all sources where we detect line emission are situated in the same star-forming region, none of them representing background sources.

In CrA-24 and SMM 2, the H_2CO , CH_3OH , SO , and SiO spectral lines show two velocity components: one low-velocity component with LSR velocities in the range $1.2\text{--}3.1\text{ km s}^{-1}$ (outflow component) and one component in agreement with the other sources, with LSR velocities in the range $4.6\text{--}6.4\text{ km s}^{-1}$ (on-source component). The SiO emission is strongest in the low-velocity component, while the other species are stronger in the

on-source component. The low-velocity component is probably an effect of a spatial overlap with a large-scale ($\sim 10\,000\text{ AU}$) outflow originating in IRS7B, extending in a north-eastward direction. This outflow has been detected in SEST mapping observations of the $\text{CH}_3\text{OH } 2_{-2} \rightarrow 1_{-1}$, E and $2_0 \rightarrow 1_0$, A+ transitions at 96.7 GHz (Miettinen et al., in prep.). Traces of this outflow can also be seen in ALMA observations of CH_3OH lines at 340 GHz (Lindberg et al. 2014a). For the CrA-24 and SMM 2 data, we separated the line emission of the two velocity components by fitting two Gaussians to each spectral line. The total line intensities, the on-source components, and the outflow components are reported in three separate tables for each of these two sources in Appendix B. The lines of all species except H_2CO , CH_3OH , SO , and SiO show only one velocity component, which is consistent with the on-source component. These lines are only listed in the tables with total line intensities.

We note that most sources with a large number of line detections are found in the R CrA cloud. CrA-44 and VV CrA also show large numbers of line detections, while the remaining sources far from R CrA show relatively few line detections.

4. Analysis

4.1. Rotational diagram analysis – IRS7B

We performed a rotational diagram analysis (see e.g. Goldsmith & Langer 1999) of several of the detected molecular species. This analysis requires the assumptions that the gas is in local thermal equilibrium (LTE) and that all lines are optically thin. In addition to the APEX data, we included ASTE data previously reported by Watanabe et al. (2012) in the fits. We performed this analysis for all the molecular species detected towards IRS7B for

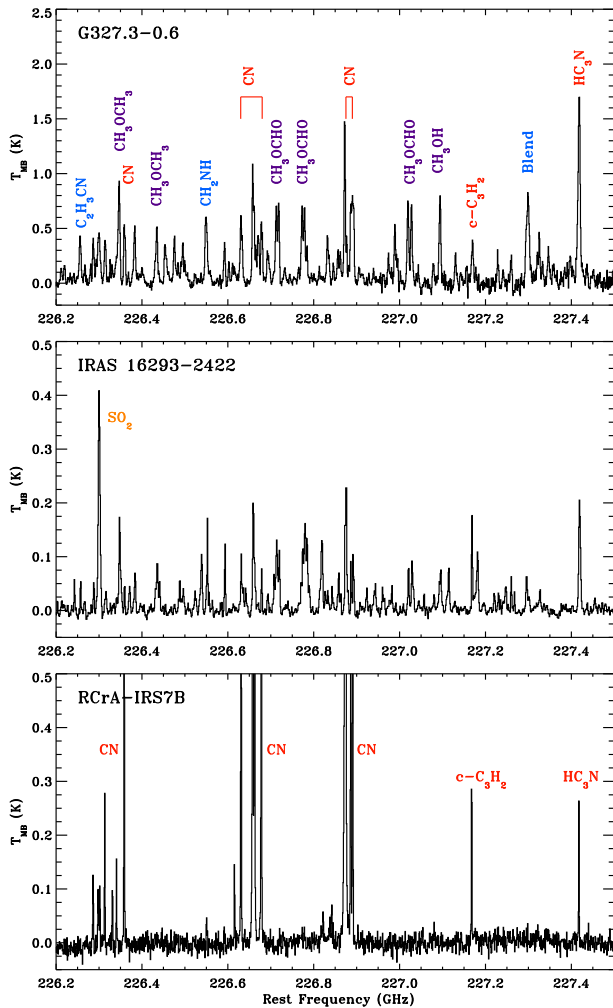


Fig. 3. Single-dish spectra around 227 GHz of the hot core G327.3-0.6 (top; observed with APEX; Bisschop et al. 2013; Bisschop et al., in prep.), the hot corino IRAS 16293-2422 (middle; observed with IRAM 30 m; Caux et al. 2011), and R CrA IRS7B (bottom; this work). The labels in the upper plot correspond well to the lines also seen in the middle plot. The colours denote oxygen-bearing (purple), nitrogen-bearing (blue), sulphur-bearing (yellow), and typical WCCC and PDR (red) species. (A colour version of this plot is available in the online journal.)

which at least two transitions with significantly different E_u were detected (a minimum E_u difference of 15 K was chosen to avoid making rotational diagram fits with large errors). This includes H_2CO , D_2CO , H_2^{13}CO , CH_3OH , CH_3CCH , H_2CS , SO , SO_2 , CS , C^{34}S , CN , DCN , HC_3N , C_2H , $c\text{-C}_3\text{H}_2$, and CH_3CHO . To establish approximate column densities, we also performed fits for H_2CCO , HNCO , and CH_3CN assuming a fixed temperature of 30 ± 5 K. We also fixed the rotational temperature to 30 ± 5 K for CH_3CHO because the three detected lines are relatively faint. The temperature 30 K was chosen to match the rotational temperatures measured for other organic species. We excluded CO and its isotopologues because their lines are probably optically thick. We used the CDMS (Müller et al. 2001) and JPL (Pickett et al. 1998) databases to retrieve molecular spectroscopy data.

From previous interferometric observations we know that the line emission in the region is very extended in comparison with

the APEX and ASTE beams (Lindberg & Jørgensen 2012), and we therefore calculated beam-averaged column densities. This requires the assumption that the column densities are relatively uniform across the range of beam sizes. Since the 0.9 mm and 0.8 mm band APEX observations of IRS7B partially coincide with the ASTE survey, we tested this assumption by comparing line strengths of lines covered in both surveys. We find that lines of H_2CO , H_2CS , HNC , DCN , and most CN lines are within errors between the two measurement sets, but lines of C^{17}O , C^{34}S , and CH_3OH are 1.5–2.3 times stronger in the ASTE data. This might be explained by the different spatial distribution of these molecules in combination with the difference in the APEX and ASTE beam sizes – the interferometric observations of Lindberg & Jørgensen (2012) show that the CH_3OH emission peaks $\sim 15''$ south of IRS7B, and this emission probably contributes more to the signal in the larger ASTE beam than in the APEX beam. When lines were available from both datasets, the ASTE data were used instead of the APEX data because the S/N ratio is higher in the ASTE data and because the APEX 1.3 mm beam size is more similar to the ASTE 0.8–0.9 mm beam sizes than the APEX 0.8–0.9 mm beam sizes. Three H_2CO lines detected in the APEX 0.8 mm observations with frequencies just above the upper boundary of the ASTE survey (364 GHz) were included, however. To account for the calibration uncertainty of the observations, we introduced a 10% calibration error in addition to the rms noise.

For the H_2CO and H_2^{13}CO lines we assumed an ortho-to-para ratio of 1.6 (see Dickens & Irvine 1999; Jørgensen et al. 2005b), for D_2CO we assumed the statistical value of 2, and for $c\text{-C}_3\text{H}_2$, H_2CS , and H_2CCO we assumed ortho-to-para ratios of 3 (Lucas & Liszt 2000; Minh et al. 1991; Ohishi et al. 1991). For the molecules with A and E states (CH_3OH , CH_3CCH , CH_3CN , and CH_3CHO), we used the statistical A/E ratios as provided by the CDMS database.

Mangum & Wootten (1993) showed that line ratios of H_2CO transitions with the same J_u -level are excellent probes of the kinetic temperature of the molecular gas. However, line ratios of transitions involving different J_u -levels also strongly depend on the density $n(\text{H}_2)$. This is further discussed in Appendix F. To account for this effect, we calculated rotational temperatures for each J_u -level separately. We then used the weighted average of these two as the H_2CO temperature, and found the column density $N(\text{H}_2\text{CO})$ and the molecular density $n(\text{H}_2)$ by comparing the measured $3_{03} \rightarrow 2_{02}$ and $5_{05} \rightarrow 4_{04}$ line strengths and RADEX estimates of these transitions (see Appendix F for a thorough description of the method used). The H_2 number density towards IRS7B is found to be $(8.9 \pm 1.0) \times 10^5 \text{ cm}^{-3}$.

The same problem probably applies to H_2^{13}CO and D_2CO , but the low number of detected lines, their low S/N levels, and the lack of collisional data for these species make it difficult to perform fits on the separate J_u -level transitions. The fits to these two isotopologues are thus highly uncertain.

The results of all the IRS7B rotational diagram fits are listed in Table 3, and the rotational diagrams are shown in Fig. 4. The rotational temperatures of the different molecules are found to vary between 10 K and 40 K. From their rotational temperatures, the molecules can be divided into two groups: on one hand the nitrogen-bearing species (i.e. cyanides) and unsaturated hydrocarbon molecules at 10–17 K, and on the other hand, the oxygen-bearing organic molecules and sulphur-bearing species at 19–40 K. H_2^{13}CO , however, has a lower rotational temperature, but the fit is made with only three lines, involving transitions with different J_u .

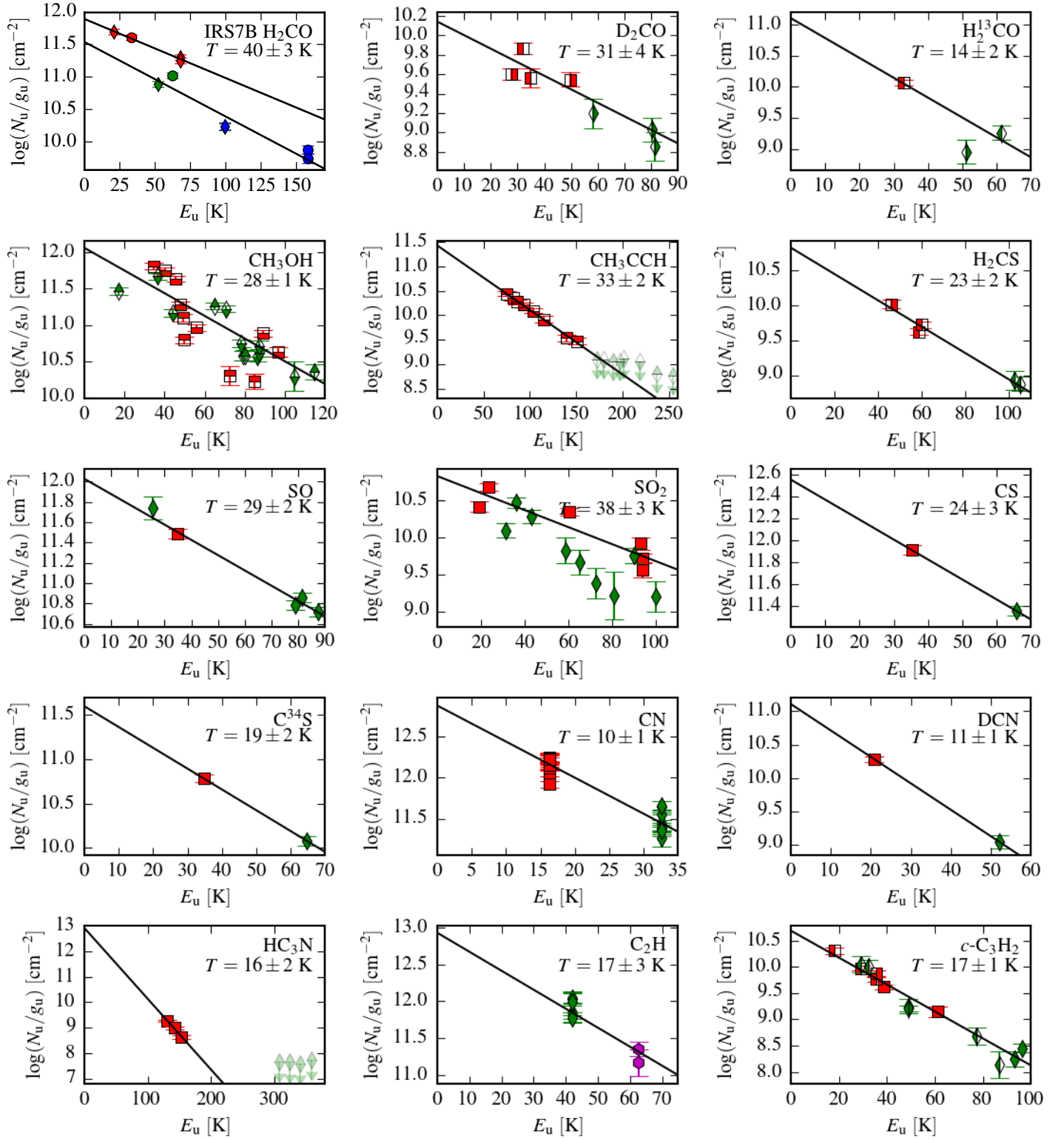


Fig. 4. Rotational diagrams of molecular species detected towards IRS7B. Red square data points are 1.3 mm lines observed with APEX, blue circle data points are 0.8 mm lines observed with APEX (this work); green diamond data points are 0.8 mm lines observed with ASTE, and magenta hexagon data points are 0.7 mm lines observed with ASTE (Watanabe et al. 2012). Upper limit data points are semi-transparent. For H_2CO , H_2^{13}CO , D_2CO , $c\text{-C}_3\text{H}_2$, and H_2CS , the ortho lines are filled in the left half, the para lines are filled in the right half, and lines that are blends of ortho transitions and para transitions are completely filled. For CH_3OH and CH_3CCH , the A lines are filled in the top half and the E lines are filled in the bottom half. (A colour version of this plot is available in the online journal.)

The rotational diagram of CH_3OH shows a considerable scatter (see Fig. 4), which like in the case of H_2CO suggests non-LTE conditions. To be able to accurately evaluate the tempera-

ture and column density of this species, we employed non-LTE RADEX models. From interferometric observations, we know that H_2CO and CH_3OH are present in the same spatial regions

Table 3. Rotational diagram parameters for IRS7B.

Molecule	T_{rot} [K]	N_{rot} [cm ⁻²]
H ₂ CO ^a	40.3 ± 2.9	(1.0 ± 0.1) × 10 ¹⁴
D ₂ CO	31.2 ± 4.2	(1.8 ± 0.3) × 10 ¹²
H ¹³ CO	13.6 ± 1.8	(3.4 ± 1.3) × 10 ¹²
CH ₃ OH	27.6 ± 0.9	(1.6 ± 0.1) × 10 ¹⁴
CH ₃ CCH	32.9 ± 2.1	(1.1 ± 0.2) × 10 ¹⁴
H ₂ CS	23.2 ± 2.1	(8.4 ± 2.1) × 10 ¹²
SO	28.9 ± 1.9	(7.1 ± 1.1) × 10 ¹³
SO ₂	38.0 ± 2.5	(1.8 ± 0.2) × 10 ¹³
CS	23.8 ± 2.6	(7.3 ± 1.8) × 10 ¹³
C ³⁴ S	18.5 ± 1.9	(6.4 ± 1.7) × 10 ¹²
CN	9.9 ± 0.3	(1.8 ± 0.1) × 10 ¹⁴
DCN	10.9 ± 0.9	(2.6 ± 0.6) × 10 ¹²
HC ₃ N	15.6 ± 1.9	(6.1 ± 6.6) × 10 ¹⁴
C ₂ H	16.9 ± 2.8	(2.8 ± 1.2) × 10 ¹⁴
<i>c</i> -C ₃ H ₂	16.9 ± 0.7	(8.5 ± 0.9) × 10 ¹²
HNCO	30 ^b	(5.1 ± 1.9) × 10 ¹²
CH ₃ CN	30 ^b	(8.7 ± 3.9) × 10 ¹¹
CH ₃ CHO	30 ^b	(1.6 ± 0.7) × 10 ¹³

Notes. ^(a) The H₂CO fit is a weighted average of the $J_u = 3$ and $J_u = 5$ fits. The two fits were also used to estimate the H₂ number density, $n(\text{H}_2) = (8.9 \pm 1.0) \times 10^5 \text{ cm}^{-3}$. ^(b) For these species, the E_u of the observed lines are in too narrow a range for the rotational temperature to be accurately calculated, or all detected lines are of a very low S/N level. We assumed a temperature of $30 \pm 5 \text{ K}$ (based on the rotational temperatures of similar species) to be able to estimate the column densities of these molecules.

around IRS7B (Lindberg & Jørgensen 2012), and we therefore assumed the H₂ density calculated from the H₂CO excitation analysis ($n(\text{H}_2) = 8.9 \times 10^5 \text{ cm}^{-3}$).

Our CH₃OH models show that with the expected physical properties, a scatter in the CH₃OH rotational diagram similar to what we observe should appear due to non-LTE excitation of the molecule. We performed a least- χ^2 fit with the temperature and column density as free parameters. The errors used in the χ^2 calculations are a combination of the rms error and a 10% calibration uncertainty. We find that the lowest χ^2 is achieved for $T = 28 \text{ K}$ and $N(\text{CH}_3\text{OH}) = 2.1 \times 10^{14} \text{ cm}^{-2}$. The best-fit temperature and column density are similar to the rotational diagram solution (see below). Figure 5 shows a contour plot of the reduced- χ^2 values of fit.

The median line width of the nitrogen-bearing and hydrocarbon species (1.6 km s^{-1}) is slightly lower than the median line width of the organic and sulphur-bearing species (2.1 km s^{-1}). The median LSR velocity is not significantly different between the two groups of molecules. The differences in temperature and velocity dispersion suggest that the two groups of molecules have different spatial origins. Interestingly, molecules from the two groups were identified as having two different spatial distributions in interferometric spectral line mapping of the region (Lindberg & Jørgensen 2012): the warmer molecules H₂CO and CH₃OH were found in two ridges north and south of the YSOs in the R CrA cloud, whereas the cooler molecules DCN, CN, *c*-C₃H₂, and HC₃N were found to peak in an east-west band around the protostars and/or in a faint outflow extending northwards from IRS7B. CH₃CCH does not exhibit the expected properties – despite being an unsaturated hydrocarbon and hav-

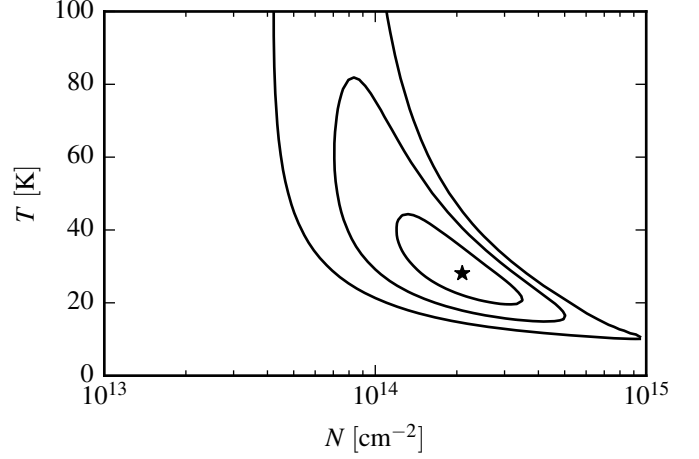


Fig. 5. Reduced- χ^2 fit to the CH₃OH lines observed towards IRS7B assuming $n(\text{H}_2) = 8.9 \times 10^5 \text{ cm}^{-3}$. The contours indicate 1σ , 2σ , and 3σ certainty. The star symbol shows the best fit.

ing a small velocity dispersion, it does have a rotational temperature similar to the second group of molecules, so its nature in relation to the other species remains unclear.

4.2. Rotational diagram analysis – other sources

Rotational diagrams of H₂CO, CH₃OH, and *c*-C₃H₂ were produced for the sources included in the CrA survey where at least two lines of the respective molecule were detected. For sources with only one detected line of a given species, upper limits of the rotational temperature and lower limits of the column density were calculated. As above, we assumed ortho-to-para ratios of 1.6 for H₂CO and 3 for *c*-C₃H₂, and an A/E ratio of 1 for CH₃OH. For the IRS7B rotational diagrams in this section we used only the APEX observations, and only those parts of the IRS7B survey that are also covered by the source survey, to avoid any bias between IRS7B and the other sources, even though more lines are available for IRS7B in the full line survey and the ASTE data. Thus, the rotational diagram parameters for IRS7B reported in this section are not identical to those in the previous section. We used the same calibration uncertainty of 10% as in the rotational diagrams for IRS7B.

Since no mm line interferometry data are available for most of the sources in the sample, we cannot determine the spatial extent of the molecular line emission. We therefore used the same approach as for IRS7B, calculating the beam-averaged column densities.

As discussed in Sect. 4.1, H₂CO rotational diagrams must treat transitions involving different J_u -levels separately. In the sources where lines from both the $J_u = 3$ and $J_u = 5$ levels are detected, we thus calculated two rotational temperatures and used the weighted average of these. We then estimated the column density and the number density with the method described in Appendix F. We find that towards the sources where we could measure the H₂ density, it is between $4 \times 10^5 \text{ cm}^{-3}$ and 10^6 cm^{-3} , except for towards the outflow component of SMM 2, where the density is lower. It is difficult to constrain the densities and column densities for the outflow components of SMM 2 and CrA-24, since the densities are low and the column densities are high, which enhances both the optical depth effects and the non-LTE effects.

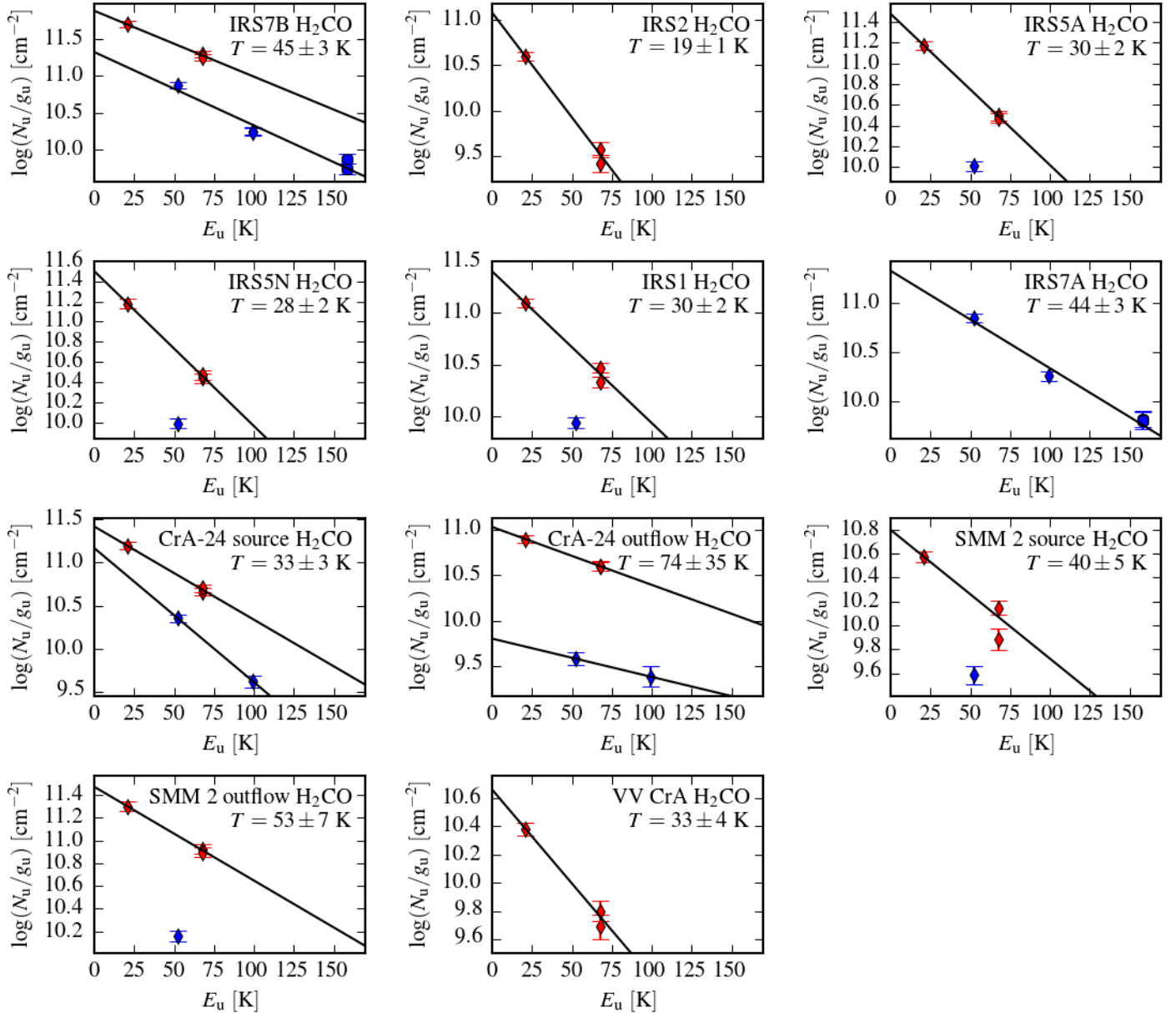


Fig. 6. H_2CO rotational diagrams of the sources in the CrA survey where at least two H_2CO lines were detected. The ortho lines are filled in the left half and the para lines are filled in the right half. Red square data points are 1.3 mm lines and blue circle data points are 0.8 mm lines, all observed with APEX. (A colour version of this plot is available in the online journal.)

The rotational diagrams are shown in Figs. 6–8 and the fitted parameters are listed in Tables 4–5. In Fig. 9, the derived H_2CO , CH_3OH , and $c\text{-C}_3\text{H}_2$ rotational temperatures are plotted versus the estimated distance to R CrA (the statistically most likely distance assuming a uniform three-dimensional spherical cloud with appropriate error bars are used to illustrate the uncertainty of projected distances). We find that the H_2CO temperatures show a large spread throughout the cloud (19–74 K), the CH_3OH temperatures show a smaller spread (12–46 K), while the $c\text{-C}_3\text{H}_2$ temperatures are uniform around 9–16 K. In the sources CrA-24 and SMM 2, the two velocity components of the H_2CO and CH_3OH spectral lines (corresponding to on-source and outflow emission, see Sect. 3.2) are treated separately. The H_2CO temperatures of the outflow components are significantly higher than the H_2CO temperatures of the on-source components. This is different for CH_3OH . Furthermore, the CH_3OH temperatures do not show the same wide range of temperatures as the H_2CO , even

though these molecules have been shown to co-exist on large scales towards IRS7B (Lindberg & Jørgensen 2012). However, CH_3OH observed in low-density outflow regions has been found to be extremely sub-thermally excited (Bachiller et al. 1995), and the CH_3OH rotational temperature is not very sensitive to local increases in kinetic temperature (Bachiller et al. 1998). As seen in the CH_3OH rotational diagram of the IRS7B survey (Fig. 4), this molecule shows a large scatter in the rotational diagram due to non-LTE effects. This shows that it is difficult to interpret CH_3OH rotational diagrams containing as few as three data points. We therefore choose not to discuss the CH_3OH rotational temperatures any further.

The large spread in the H_2CO temperatures might have been caused by optical depth effects, in particular for the H_2CO $3_{03} \rightarrow 2_{02}$ line. We investigated this using the H_2^{13}CO $3_{12} \rightarrow 2_{11}$ transition, which is detected towards seven of the studied sources. We assumed the ISM value for the $^{12}\text{C}/^{13}\text{C}$ ratio (69 ± 6 ; Wilson

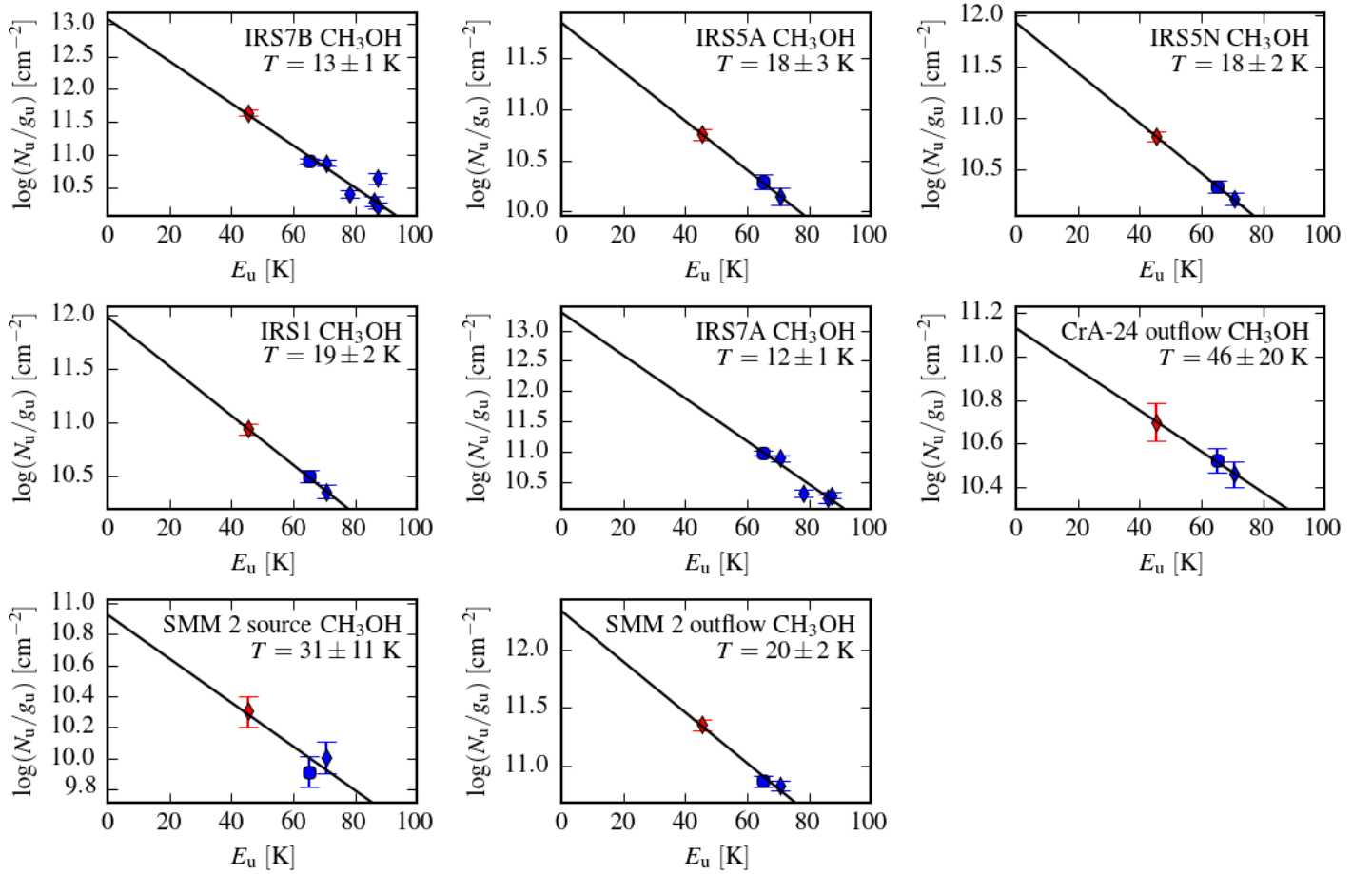


Fig. 7. CH_3OH rotational diagrams of the sources in the CrA survey where at least two CH_3OH lines were detected and a positive rotational temperature could be fitted. The A lines are filled in the top half and the E lines are filled in the bottom half. Red square data points are 1.3 mm lines and blue circle data points are 0.9 mm lines, all observed with APEX. (A colour version of this plot is available in the online journal.)

1999), an ortho-to-para ratio of 1.6, and excitation temperatures derived from the respective H_2CO rotational diagrams. For a majority of the sources, we find that this line ratio corresponds to optical depths τ of the H_2CO $3_{03} \rightarrow 2_{02}$ line between 0.3 and 0.8. For IRS2 and the SMM 2 on-source component the numbers are higher (1.1 and 2.2), but it should be noted that these numbers are uncertain since the H_2^{13}CO $3_{12} \rightarrow 2_{11}$ line is at a low S/N-level in these sources. The SMM 2 on-source value may also have errors originating in the separation between the on-source and outflow components. We conclude that the estimated H_2CO optical depths are so low that the detected spread in temperatures must be real.

The $c\text{-C}_3\text{H}_2$ rotational temperatures are found to be constant at around 10–15 K for all sources. Non-LTE analysis using RADEX (van der Tak et al. 2007) shows that the observed line strengths are consistent with LTE and low optical depths, and we therefore expect that the measured rotational temperatures reflect the kinetic temperature of the $c\text{-C}_3\text{H}_2$ gas. The H_2CO temperatures are found to be strongly elevated compared to the $c\text{-C}_3\text{H}_2$ temperatures ($T(\text{H}_2\text{CO}) \sim 30\text{--}50$ K) in the sources close to R CrA (see Fig. 9). This is further discussed in Sect. 5.

4.3. Molecular abundances in IRS7B and other protostars

4.3.1. Rotational diagrams

The only complex molecules detected towards IRS7B are CH_3OH , CH_3CCH , CH_3CN , and CH_3CHO , the latter two only tentatively detected. In typical hot corino sources, complex organic molecules are present at comparably high abundance levels. To investigate whether the relatively low number of complex organic molecules detected towards IRS7B is significant, we compared relative abundances (and upper limits for non-detections) of organic molecules in IRS7B with the typical hot corino source IRAS 16293-2422, the WCCC source L1527, the quiescent source B1-b, and the L1157 outflow. To account for the uncertainty and difference in the sizes of the emission regions of the different sources, we normalised the abundances with that of CH_3OH . We estimated the relative abundances by calculating the ratio of column densities as calculated from the rotational diagrams (see Table 3), thus assuming LTE and optically thin lines. The large uncertainties on some of the column density measurements will, however, introduce large uncertainties in these ratios.

To estimate upper limits on abundances of molecules not detected in IRS7B, we used Splatalogue and the line survey of IRAS 16293-2422 (Caux et al. 2011) to identify the strongest lines in the covered spectral bands. Assuming a temperature of 30 K and a line width of 2 km s^{-1} , we calculated the abundance that would generate a line that would just reach the 3σ

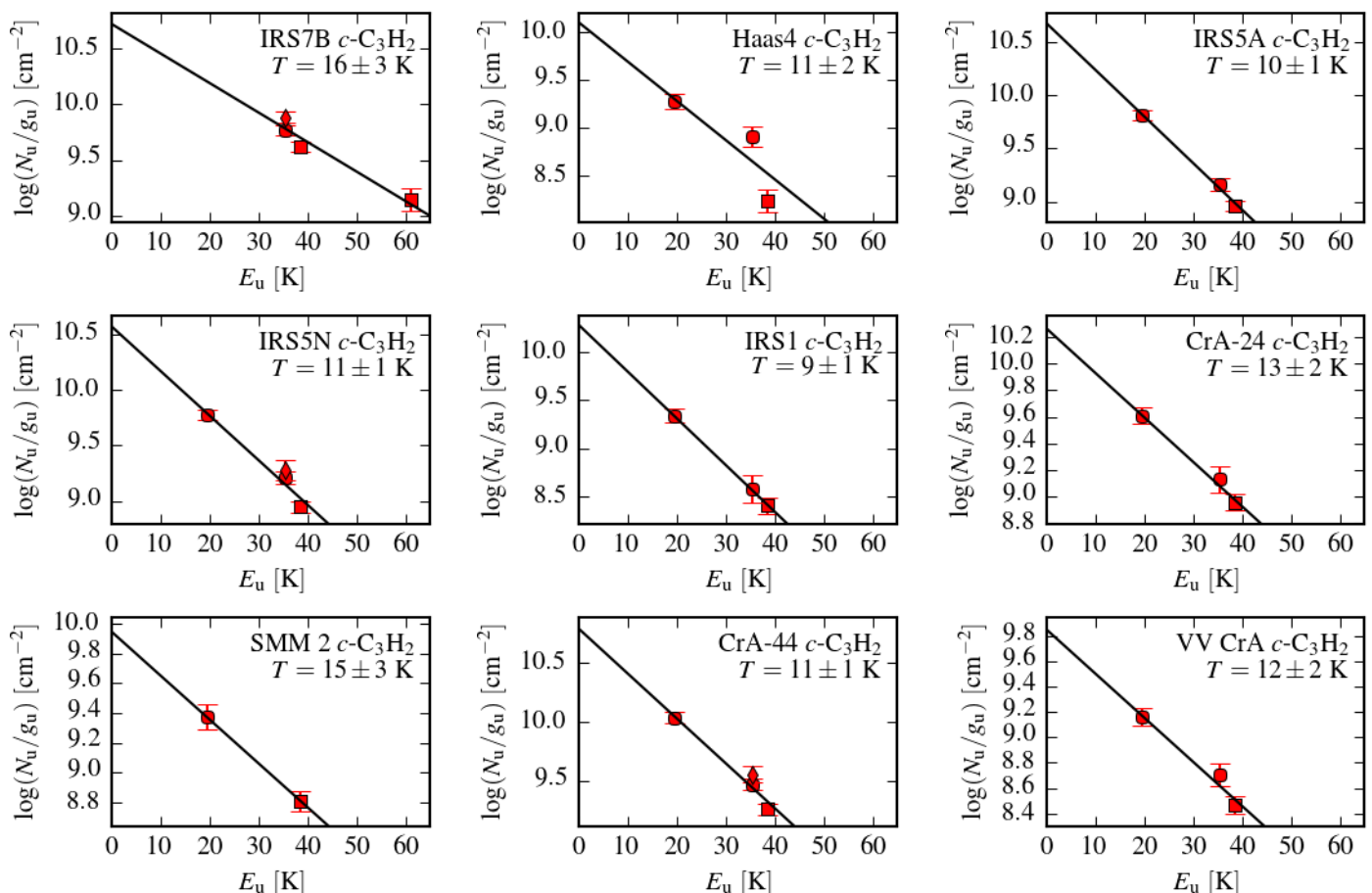


Fig. 8. c -C₃H₂ rotational diagrams of the sources in the CrA survey where at least two c -C₃H₂ lines were detected. The ortho lines are filled in the left half, the para lines are filled in the right half, and the lines that are blends of ortho transitions and para transitions are completely filled. All data points are 1.3 mm lines observed with APEX. (A colour version of this plot is available in the online journal.)

detection limit in the APEX or ASTE observations of the band covering that certain line. In some ambiguous cases, several lines with similar line characteristics were tested, and the one generating the lowest upper limit was used. The lines used were for CH₃OCHO the 227.560–227.564 GHz octuplet and for HCOOH the 220.038 GHz line. For CH₃OCH₃ we found that the 225.599 GHz quadruplet produced the best upper limit in the APEX survey, but the 358.447–358.457 GHz octuplet covered by the ASTE survey (Watanabe et al. 2012) provided an upper limit three times lower, so this line was used instead. It is difficult to calculate upper limits of the abundances of complex organic molecules relative to CH₃OH in the CrA source survey because the CH₃OH excitation is poorly understood in these sources (see Sect. 4.2).

The resulting abundance ratios or upper limits of a selection of molecules measured towards IRS7B, the hot corino IRAS 16293-2422, the WCCC source L1527, the quiescent protostar B1-b, and the L1157 outflow are shown in Table 6 and in Fig. 10.

We note that several of the organic species are significantly less abundant towards IRS7B compared to IRAS 16293-2422, including CH₃CN, CH₃OCH₃, CH₃OCHO, and HCOOH, which makes the chemical parameters of IRS7B more similar to the L1157 molecular outflow and the quiescent source B1-b, although the CH₃OH gas is much warmer towards IRS7B (28 ± 1 K towards IRS7B, 10 ± 5 K towards B1-b, and 12 ± 2 K towards the L1157 outflow). Simpler organic species like H₂CO,

H₂CCO, and HNCO have similar abundances towards IRS7B and IRAS 16293-2422, whereas unsaturated hydrocarbons and cyanides (c -C₃H₂, CN, HC₃N, and C₂H) are over-abundant towards IRS7B compared to IRAS 16293-2422. The unsaturated hydrocarbons c -C₃H₂ and C₂H are, however, under-abundant towards IRS7B compared to the WCCC source L1527, and C₄H is non-detected towards IRS7B (Sakai et al. 2009a). This shows that IRS7B is not a WCCC source. The given upper limits, as well as the values calculated for H₂CCO, HNCO, CH₃CN, and CH₃CHO, were calculated under the assumption that the temperature of these species is 30 K. A lower temperature would increase the ratios for these species.

Interferometric observations of CH₃OH show that this emission is present on large scales around IRS7B, in particular in two extended ridges north and south of IRS7B (Lindberg & Jørgensen 2012), which are partially covered by the APEX and ASTE beams. These beam-averaged abundance ratios therefore probably reflect the composition of that large-scale molecular gas heated by R CrA (Lindberg & Jørgensen 2012), rather than the compact inner envelope of IRS7B.

4.3.2. Radiative transfer modelling

We used the radiative transfer code RATRAN (Hogerheijde & van der Tak 2000) to model the line strengths of some of the molecular species detected towards IRS7B. The one-dimensional envelope and temperature model made by Lindberg

Table 4. Rotational diagram parameters for H₂CO in the survey of CrA sources. Sources where the fit could not be performed are excluded. The H₂ densities n and column densities N were measured by the method described in Appendix F, which can only be made for the sources where both the $3_{03} \rightarrow 2_{02}$ and the $5_{05} \rightarrow 4_{04}$ lines have been detected. To facilitate comparison between IRS7B and the other sources, only the lines covered by the source survey are included, which explains why IRS7B shows different values here and in Table 3.

Source name	$T_{J_u=3}^a$ [K]	$T_{J_u=5}^b$ [K]	T_{av}^c [K]	n [cm ⁻³]	N^d [cm ⁻²]
IRS7B	48.8 ± 6.2	43.8 ± 2.7	45.3 ± 3.4	7.7×10^5	1.0×10^{14}
Haas4	< 24.3
IRS2	18.9 ± 1.3	...	18.9 ± 1.3
IRS5A	29.8 ± 2.4	...	29.8 ± 2.4	4.0×10^5	3.7×10^{13}
IRS5N	28.4 ± 2.1	...	28.4 ± 2.1	3.9×10^5	3.9×10^{13}
IRS1	29.5 ± 2.4	...	29.5 ± 2.4	4.6×10^5	2.8×10^{13}
IRS7A	...	43.6 ± 3.1	43.6 ± 3.1
CrA-24 source	40.3 ± 4.3	28.0 ± 3.1	33.2 ± 2.7	1.3×10^6	2.6×10^{13}
CrA-24 outflow	68.6 ± 12.9	103.7 ± 68.1	74.2 ± 34.7	... ^e	... ^e
SMM 2 source	40.4 ± 5.3	...	40.4 ± 5.3	6.3×10^5	6.6×10^{12}
SMM 2 outflow	52.6 ± 7.3	...	52.6 ± 7.3	< 2 × 10 ^{5e}	> 6 × 10 ^{13e}
CXO42	< 87.5
CrA-44	< 21.2
CrA-33	< 54.5
VV CrA	32.7 ± 3.7	...	32.7 ± 3.7

Notes. ^(a) Rotational temperatures of the transitions with $J_u = 3$. ^(b) Rotational temperatures of the transitions with $J_u = 5$. ^(c) Weighted average of the two previous, if they are both measured, otherwise the same as the only one measured. ^(d) The total H₂CO column density assuming an ortho-to-para ratio of 1.6. ^(e) For these sources, the column density and H₂ density could not be constrained from the $3_{03} \rightarrow 2_{02}/5_{05} \rightarrow 4_{04}$ ratio.

Table 5. Rotational diagram parameters for CH₃OH and *c*-C₃H₂ in the survey of CrA sources. Sources where neither of the fits could be performed are excluded. To facilitate comparison between IRS7B and the other sources, only the lines covered by the source survey are included, which explains why IRS7B shows different values here and in Table 3.

Source name	CH ₃ OH		<i>c</i> -C ₃ H ₂	
	T [K]	N^a [cm ⁻²]	T [K]	N^b [cm ⁻²]
IRS7B	13.5 ± 0.6	$(4.5 \pm 1.0) \times 10^{14}$	16.5 ± 2.6	$(8.6 \pm 3.2) \times 10^{12}$
Haas4	10.6 ± 1.7	$(1.1 \pm 0.5) \times 10^{12}$
IRS2	< 16.2	> 1.2 × 10 ¹³
IRS5A	18.1 ± 2.6	$(4.5 \pm 2.1) \times 10^{13}$	9.9 ± 0.8	$(3.7 \pm 0.9) \times 10^{12}$
IRS5N	17.7 ± 2.2	$(5.3 \pm 2.2) \times 10^{13}$	10.9 ± 0.9	$(3.3 \pm 0.8) \times 10^{12}$
IRS1	18.9 ± 2.4	$(6.7 \pm 2.6) \times 10^{13}$	8.9 ± 1.0	$(1.3 \pm 0.5) \times 10^{12}$
IRS7A	12.2 ± 0.9	$(6.4 \pm 3.0) \times 10^{14}$
CrA-24	13.0 ± 1.7	$(2.1 \pm 0.7) \times 10^{12}$
CrA-24 source
CrA-24 outflow	46.3 ± 20.2	$(4.4 \pm 2.7) \times 10^{13}$
SMM 2	14.7 ± 2.9	$(1.2 \pm 0.5) \times 10^{12}$
SMM 2 source	30.6 ± 11.4	$(1.4 \pm 1.0) \times 10^{13}$
SMM 2 outflow	19.9 ± 2.3	$(1.6 \pm 0.6) \times 10^{14}$
CrA-44	11.4 ± 0.9	$(6.0 \pm 1.4) \times 10^{12}$
CrA-33	< 14.4	> 2.2 × 10 ¹³	< 10.7	> 5.8 × 10 ¹¹
VV CrA	12.5 ± 1.8	$(7.8 \pm 2.9) \times 10^{11}$

Notes. ^(a) The CH₃OH column density assuming an A/E ratio of 1. ^(b) The *c*-C₃H₂ column density assuming an ortho-to-para ratio of 3.

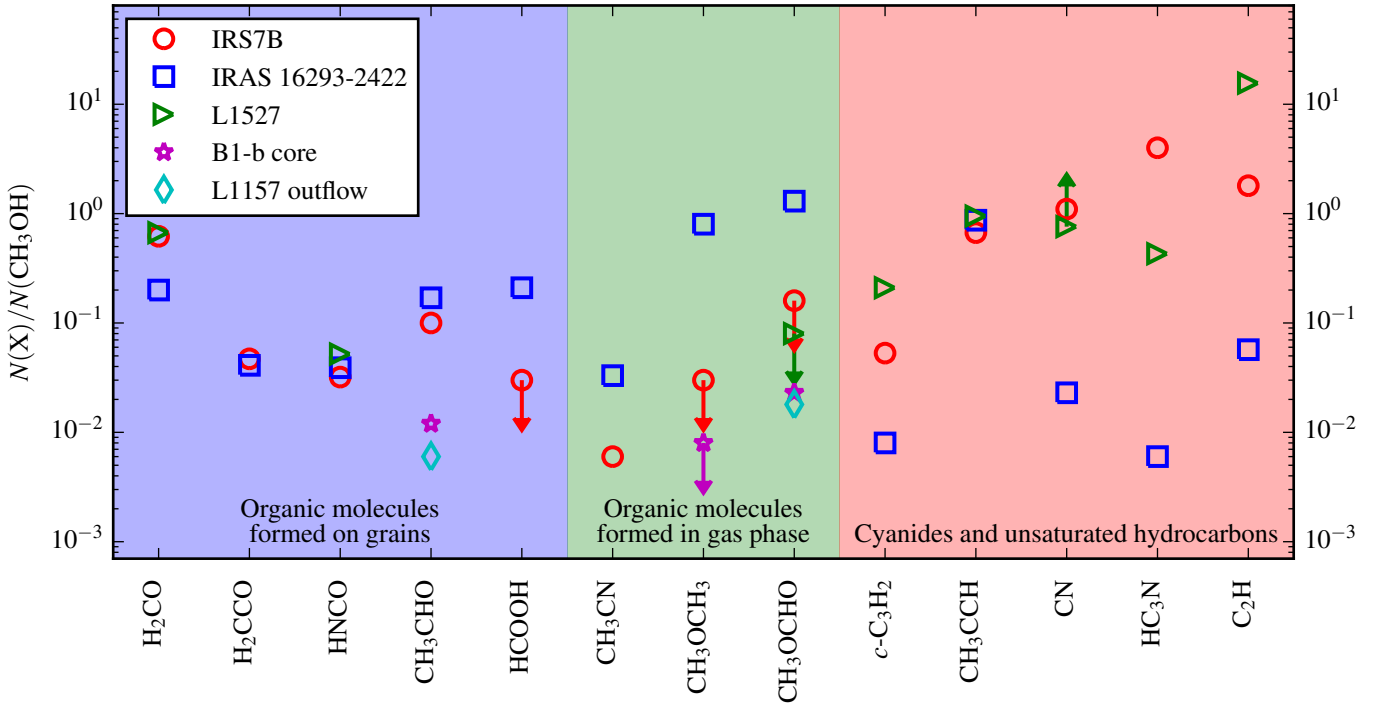
& Jørgensen (2012) and refined by Lindberg et al. (2014a) was employed. This is an envelope with a power-law density profile ($\rho \sim r^{-1.5}$) heated both by a central object and from the outside by irradiation corresponding to that of the nearby Herbig Be star R CrA. We used the RATRAN models to calculate abundances for 13 important species for which most or all lines are expected to be optically thin (see Jørgensen et al. 2004). The model abun-

dances were kept constant as a function of radius for all species except CN, since the modelled species are not expected to be heavily affected by hot corino emission. On the other hand, we let the abundance of the photo-destruction product CN take the shape of a step function, allowing for a higher CN abundance in the outer envelope, where the gas is more affected by photo-destruction from UV radiation originating in R CrA.

Table 6. Molecular abundances relative to CH₃OH ($N(X)/N(\text{CH}_3\text{OH})$) towards IRS7B and other protostellar sources as established from rotational diagrams. See also Fig. 10.

Molecule	IRS7B	I16293 ^a	L1527 ^b	B1-b core ^c	L1157 outflow ^d
CH ₃ OH	$\equiv 1$	$\equiv 1$	$\equiv 1$	$\equiv 1$	$\equiv 1$
H ₂ CO	0.62	0.20	0.67
H ₂ CCO	0.047	0.041
HNCO	0.032	0.039	0.052
CH ₃ CHO	0.10	0.17	...	0.012	0.006
HCOOH	< 0.03	0.21
CH ₃ CN	0.006	0.033
CH ₃ OCH ₃	< 0.03	0.80	...	< 0.008	...
CH ₃ OCHO	< 0.16	1.3	< 0.08	0.023	0.018
<i>c</i> -C ₃ H ₂	0.053	0.008	0.21
CH ₃ CCH	0.67	0.87	0.95
CN	1.1	0.023	> 0.76 ^e
HC ₃ N	~ 4	0.006	0.43
C ₂ H	1.8	0.057	15.6

Notes. ^(a) IRAS 16293-2422 (van Dishoeck et al. 1995; Schöier et al. 2002; Cazaux et al. 2003). ^(b) Sakai & Yamamoto (2013) and references therein. Observations were performed with several different single-dish telescopes with beam sizes between 10'' and 30''. Since the source is extended (Sakai et al. 2010), we used the beam-averaged column densities. ^(c) Öberg et al. (2010). ^(d) Bachiller & Pérez Gutiérrez (1997); Arce et al. (2008). ^(e) Agúndez et al. (2008).

**Fig. 10.** Graphical representation of molecular abundances relative to the CH₃OH abundance as given in Table 6 for IRS7B, the hot corino source IRAS 16293-2422, the WCCC source L1527, the quiescent protostar B1-b, and the L1157 outflow. See the notes of Table 6 for references. For a discussion on the classification of gas and grain formation of the organic species, see Charnley (1997, 2001). (A colour version of this plot is available in the online journal.)

In addition to the APEX line data of IRS7B reported in this work, we used *c*-C₃H₂, C¹⁷O, C³⁴S, SO, CN, HC¹⁸O⁺, and DCN line data from the ASTE survey of IRS7B (Watanabe et al. 2012).

Molecular data files from the LAMDA database (Schöier et al. 2005) were employed when available. In addition, the same molecular datafiles as were used by Jørgensen et al. (2004) were used for CN and HC₃N, since data for hyperfine lines of CN

and high-*J* transitions of HC₃N are not available in the LAMDA database. For isotopologue species where no LAMDA data files are available, the collisional data of the main isotopologue were used, but the line parameters of the isotopologue were acquired from the CDMS database (Müller et al. 2001). This was done for ¹³CS, C³⁴S, C³³S, DCN, and DNC.

The line widths and LSR velocities were estimated from Gaussian fits to the spectral lines. The abundance was left as

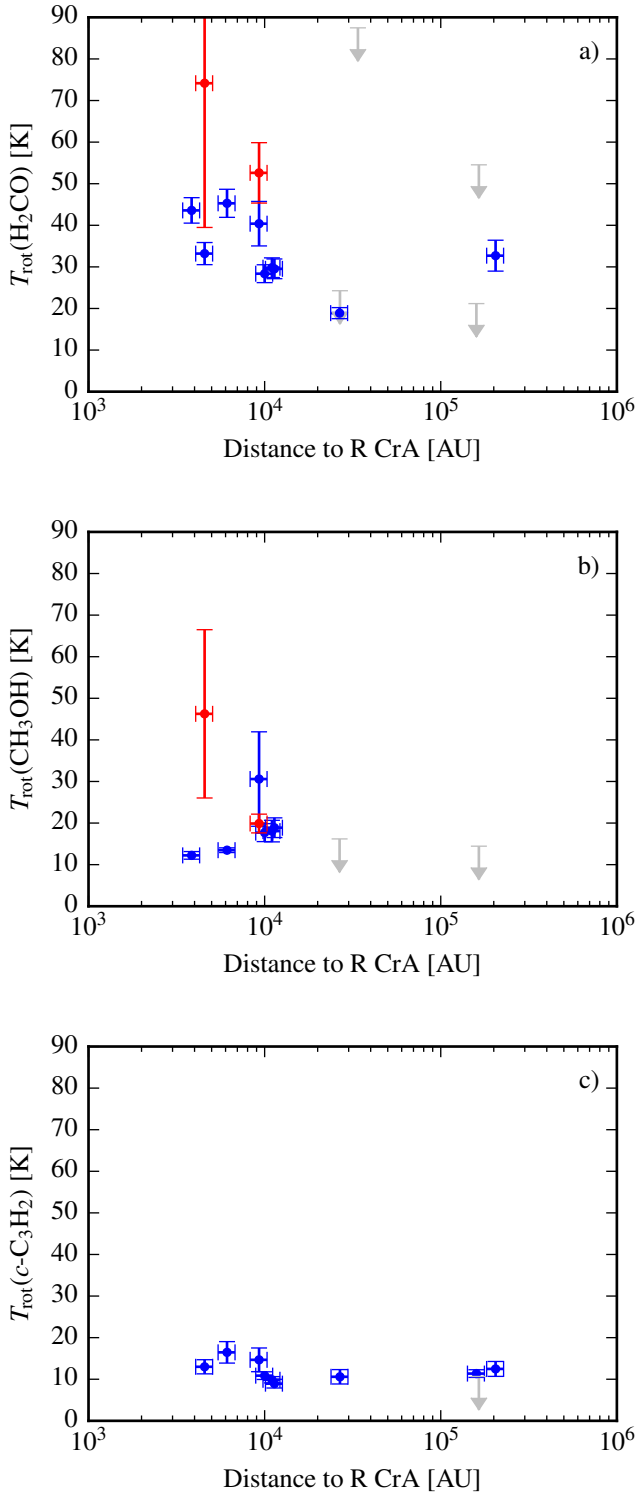


Fig. 9. Rotational temperatures for a) H_2CO , b) CH_3OH , and c) $c\text{-C}_3\text{H}_2$ as functions of distance to R CrA. Upper limits are shown in grey. In the H_2CO plot, CrA-24 and SMM 2 have two data points each, one for the on-source component (blue) and one for the outflow component (red), and the same applies to the CH_3OH plot when the rotational temperature could be measured. The CH_3OH rotational temperature most likely does not reflect a physical temperature due to non-LTE excitation in combination with few data points. (A colour version of this plot is available in the online journal.)

a free parameter, and the best value was found through a least- χ^2 fit. The error used for the χ^2 calculations is the combination of the rms error and a calibration uncertainty of 10% for both the APEX and the ASTE observations.

Table 7 lists the resulting modelled abundances together with data for other low-mass embedded protostellar sources in the literature. The abundance of the optically thick species CO, CS, and HCO^+ were calculated from optically thin isotopologues using isotope ratios from the literature: C, O, and ^{34}S isotope ratios were taken from Wilson (1999) and ^{33}S isotope ratios from Chin et al. (1996).

A contour plot of the reduced- χ^2 values as function of the CN abundances is shown in Fig. 11. The fit clearly is relatively insensitive to the inner abundance ($X_{\text{inner}} \lesssim 10^{-8}$), but fixes the outer abundance to $X_{\text{outer}} \sim \text{few} \times 10^{-9}$.

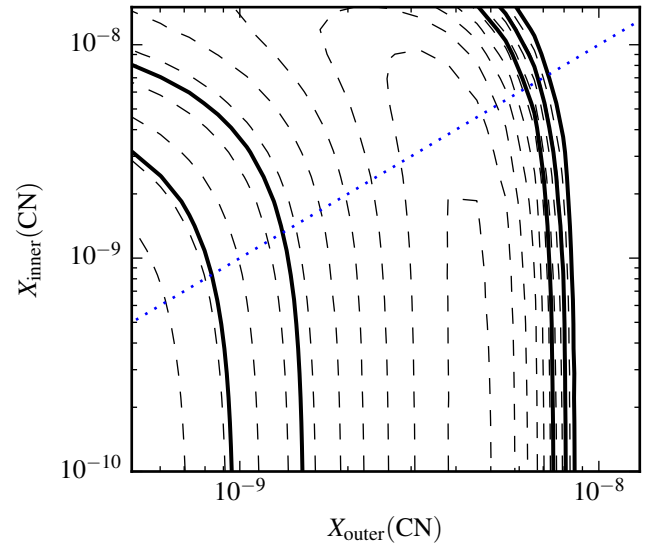


Fig. 11. Reduced- χ^2 fit to the CN abundance. The solid lines show the 1σ , 2σ , and 3σ confidence levels. The dashed lines show the reduced- χ^2 values in steps of 5. The border between inner and outer abundance lies where the temperature falls below 30 K, which occurs at 370 AU. The blue dotted line shows the values for equal inner and outer abundances. (A colour version of this plot is available in the online journal.)

While the IRS7B abundances of many of the more common molecules (CO, HCO^+ , SO, and CS) are comparable to those in other sources, we find that the CN-bearing species (CN, DCN, DNC, and HC_3N) and $c\text{-C}_3\text{H}_2$ are strongly enhanced in IRS7B compared to the other protostellar envelopes. This, in combination with the low upper limits of complex organic molecules discussed above, demonstrates that the chemical properties of the gas around IRS7B strongly differs from those of most other protostars studied before. Previous studies have shown that small hydrocarbon molecules such as $c\text{-C}_3\text{H}_2$ and C_2H are enhanced in PDR regions. In high-UV flux regions this is a result of gas-phase chemistry (Cuadrado et al. 2015), but in regions with more moderate UV flux levels it is a consequence of photodestruction of PAHs (Montillaud et al. 2013). For further references and discussion, see also Guzmán et al. (2015).

4.4. Isotopic fractionation in CrA

The $[\text{C}^{18}\text{O}]/[\text{C}^{17}\text{O}]$ abundance ratio in IRS7B is found to be 5.6, considerably higher than the expected value in the local ISM, 3.6 (Wilson 1999). It should, however, be noted that the C^{17}O

Table 7. Results of RATRAN models of fractional abundances of certain molecules in R CrA IRS7B and similar modelling results from the literature for other protostellar sources. The reduced- χ^2 values for IRS7B assume a 10% calibration error and can only be computed for species with at least two spectral lines.

Molecule	IRS7B Abundance	χ^2_{red}	I16293 ^a Abundance	Class 0 ^b Abundance	Class I ^b Abundance	Prestellar ^b Abundance
CO ^c	1.4×10^{-4}	...	3.3×10^{-5}	2.1×10^{-5}	1.1×10^{-4}	1.4×10^{-5}
C ¹⁷ O	5.7×10^{-8}	6.9	1.6×10^{-8}
C ¹⁸ O	3.2×10^{-7}	...	6.2×10^{-8}
HCO ^{+c}	3.8×10^{-9}	...	1.4×10^{-9}	2.2×10^{-9}	1.1×10^{-8}	8.0×10^{-10}
HC ¹⁸ O ⁺	6.8×10^{-12}	3.6	6.4×10^{-12}
SO	1.9×10^{-9}	33.6	4.4×10^{-9}	2.0×10^{-9}	2.3×10^{-9}	1.5×10^{-9}
CS ^c	6.7×10^{-9}	...	3.0×10^{-9}	1.5×10^{-9}	4.3×10^{-9}	1.8×10^{-9}
¹³ CS	8.8×10^{-11}
C ³⁴ S	2.1×10^{-10}	16.2	1.2×10^{-10}
C ³³ S	6.8×10^{-11}
CN outer ^d	4.5×10^{-9}
CN inner ^d	$< 1 \times 10^{-9}$	8.5	8.0×10^{-11}	6.9×10^{-10}	3.0×10^{-9}	4.8×10^{-9}
DCN	7.2×10^{-11}	14.1	1.3×10^{-11}	1.4×10^{-11}	...	7.7×10^{-12}
DNC	6.8×10^{-11}	...	4.2×10^{-12}
HNCO	1.2×10^{-10}	0.002	1.3×10^{-10}
HC ₃ N	3.3×10^{-9}	11.2	1.5×10^{-10}	3.5×10^{-10}	3.1×10^{-9}	8.2×10^{-10}
c-C ₃ H ₂	3.0×10^{-10}	12.9	1.6×10^{-11}

Notes. ^(a) IRAS 16293-2422, Schöier et al. (2002). ^(b) Average of sources in Jørgensen et al. (2004). ^(c) The abundances for these optically thick species have been calculated from the optically thin isotopologues assuming local ISM isotope ratios (Wilson 1999; Chin et al. 1996). ^(d) The CN fit was performed with a step in the abundance profile at 370 AU (where $T \approx 30$ K).

fit includes both the 3–2 and 2–1 lines, whereas the C¹⁸O fit only includes the 2–1 line. The uncertainty of the large-scale CO distribution and the differing beam sizes could contribute to the unusual isotope ratio, and if the ratio is calculated only with the 2–1 lines, a [C¹⁸O]/[C¹⁷O] ratio of 4.0 is reached. The [³⁴CS]/[¹³S] ratio 2.4 is slightly lower than the local ISM value 2.9, and the [³⁴CS]/[³³CS] ratio 3.1 is lower than the local ISM value 6.3 ± 1.0 .

We also investigated the D/H ratio of H₂CO towards IRS7B. As mentioned in Sect. 4.1, the excitation conditions of the H₂CO isotopologues is somewhat uncertain. Since the D₂CO rotational diagram fit is much better than the H₂¹³CO fit, we applied the D₂CO rotational temperature to the H₂¹³CO excitation diagram to acquire a better estimate on the H₂¹³CO column density. Assuming the local ISM value for the ¹²C/¹³C ratio (69 ± 6 , Wilson 1999), we estimated the [D₂CO]/[H₂CO] ratio towards IRS7B to 0.018 ± 0.003 . The calculated ratio is within the errors of the value of Watanabe et al. (2012), who calculated the ratio for temperatures fixed at 15 K, 20 K, and 25 K. Their [D₂CO]/[H₂CO] ratio for 25 K is 0.021 ± 0.003 . They also observed HDCO, and calculated the [HDCO]/[H₂CO] ratio to 0.052 ± 0.008 assuming the same temperature. We compared these values with [D₂CO]/[H₂CO] and [HDCO]/[H₂CO] ratios in other sources. Although the [D₂CO]/[H₂CO] value is elevated in comparison with what was found in Orion KL ([D₂CO]/[H₂CO] = 0.003; Turner 1990), the level of deuteration is lower than what is found in typical hot corino sources and other Class 0 protostars (Parise et al. 2006; e.g. [D₂CO]/[H₂CO] = 0.05 ± 0.008 in IRAS 16293-2422). This could suggest that grain-surface chemistry is less important for the formation of H₂CO in IRS7B than in other low-mass protostellar sources, but the lower level of deuteration could also be an effect of the higher large-scale temperature due to the external irradiation. However, while the

[D₂CO]/[H₂CO] and [HDCO]/[H₂CO] ratios are biased by the D/H ratio in the precursor molecules, the incremental fractionation ratio [HDCO]/[H₂CO]:[D₂CO]/[HDCO] only depends on the formation mechanisms for H₂CO (Turner 1990; Rodgers & Charnley 2002). The incremental fractionation ratio of H₂CO in IRS7B is 0.15 ± 0.04 , assuming the [D₂CO]/[H₂CO] from this work and the [HDCO]/[H₂CO] ratio of Watanabe et al. (2012) at 25 K. This is a low value, but still within the errors of the hot corino values (Parise et al. 2006), so we cannot draw any clear conclusions as to whether there is a difference in the formation path of H₂CO in IRS7B versus hot corinos or not.

Watanabe et al. (2012) also measured the DCN/HCN ratio, which was found to be 0.010 ± 0.001 , similar to the IRAS 16293-2422 value (van Dishoeck et al. 1995).

We detect ¹³CN and C¹⁵N towards several of the sources in CrA. In most sources, the ¹²CN lines are only observed in the 3 → 2 rotational transitions, while the isotopologue species are observed in the 2 → 1 rotational transitions. The uncertainty in the excitation conditions makes the estimation of isotope ratios difficult. For IRS7B, we have 2 → 1 observations also for the ¹²CN lines, and (excluding the strongest ¹²CN lines, which are expected to be optically thick) we find a CN/C¹⁵N value of 229 ± 50 , which is within the errors of the ¹⁴N/¹⁵N ratios calculated from IRS7B observations using H¹³CN/HC¹⁵N ratios (287 ± 36) and HN¹³C/H¹⁵NC ratios (259 ± 34) by Wampfler et al. (2014).

Faint ³⁴SO lines are detected towards IRS7A (but not IRS7B). The resulting [SO]/[³⁴SO] ratio is found to be 11 ± 10 , which is almost within the errors of the ISM value ~ 22 (Wilson 1999).

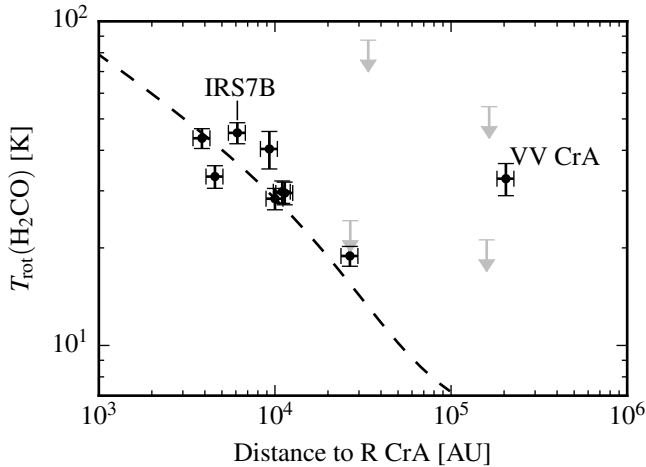


Fig. 12. 1-D radiative transfer model of heating from R CrA (dashed line) plotted together with the H_2CO rotational temperatures measured in the CrA sources as a function of distance to R CrA. For CrA-24 and SMM 2, only the on-source components are shown. Upper limits are shown in grey. See also Fig. 9a.

5. Discussion

In Sect. 4.2, the H_2CO rotational temperatures in the survey of CrA sources were found to be highest close to the Herbig Be star R CrA (Fig. 9a). This suggests that the sphere of thermal influence of R CrA (see Adams & Shu 1985) stretches out to radii greater than 10 000 AU. To study if this is plausible, radiative transfer modelling was employed. Using the dust radiative transfer code *Transphire* (Dullemond et al. 2002), we constructed a one-dimensional model of the molecular cloud around R CrA. The density was assumed to be constant at $n = 10^4 \text{ cm}^{-3}$ throughout the cloud, starting at a distance of 200 AU from R CrA. The luminosity of R CrA was set to $144 L_{\odot}$ (see Lindberg et al. 2014b for a thorough discussion of the luminosity of R CrA). For this configuration, *Transphire* calculates the temperature in the region self-consistently as a function of radius. The model is shown compared to the data in Fig. 12, and we conclude that it provides a good fit to the H_2CO rotational temperature data points within a radius of $\sim 30\,000$ AU from R CrA. We attribute the deviations outside the error bars to irregularities in the distribution of gas in the molecular cloud, with the exception for the source VV CrA.

The protostar VV CrA has a projected distance of more than 0.5 pc (100 000 AU) to R CrA, but still has a comparably high H_2CO rotational temperature (33 ± 4 K). This cannot be explained by the irradiation from R CrA. However, VV CrA is a fairly luminous protostar, with a higher flux at $5.8 \mu\text{m}$ than R CrA (Peterson et al. 2011). Using 2MASS, Spitzer, IRAS, PACS, and SCUBA data of VV CrA (Sicilia-Aguilar et al. 2013, and references therein), we estimate the bolometric luminosity of the source to $13L_{\odot}$, which is not sufficient to explain the measured H_2CO temperature. However, by the use of the Robitaille database of SED models for YSOs (Robitaille et al. 2006) and their online³ fitting tool (Robitaille et al. 2007), we find that the best matches to the SED are protostellar models with luminosities $\geq 40L_{\odot}$. Such a luminosity can heat the gas to 30 K on scales of several 1000 AU, and the elevated temperature in the envelope of VV CrA could thus be attributed to internal irradiation from

VV CrA itself. It should, however, be noted that the SED models of Robitaille et al. (2006) work best with protostars at later stages of evolution.

The $c\text{-C}_3\text{H}_2$ rotational temperatures measured in the source survey are much lower than the H_2CO temperatures and independent of the distance to R CrA. This can be explained by the $c\text{-C}_3\text{H}_2$ gas being more compact than the H_2CO gas, and thus more shielded against external irradiation. SMA interferometry of the region around IRS7B shows $c\text{-C}_3\text{H}_2$ emission that is more concentrated towards the low-mass YSOs than the H_2CO emission is, which supports this hypothesis (Lindberg & Jørgensen 2012), but H_2CO and $c\text{-C}_3\text{H}_2$ mapping of additional sources is required to confirm this explanation.

We also investigated the chemical composition of the molecular gas detected towards IRS7B. A simple comparison of spectra from three different star-forming regions – a hot core, a hot corino, and IRS7B (Fig. 3) – suggests that the chemistry of the low-mass hot corino source IRAS 16293-2422 has more in common with the high-mass hot core G327.3-0.6 than with the low-mass protostar IRS7B. Towards IRS7B, the PDR-tracing CN lines dominate the spectrum completely, whereas the two other sources have spectra dominated by various complex organic molecules. The only complex molecules detected in IRS7B are CH_3OH , CH_3CCH , CH_3CN , and CH_3CHO (the latter two only tentatively detected). CH_3OCH_3 and CH_3CN are non-detected also in high-resolution ALMA observations of the inner envelope of IRS7B (Lindberg et al. 2014a). We also find that the relative abundances of several complex organic molecules in IRS7B are significantly lower than what is found in typical hot corino sources. However, simple cyanides (CN and HCN) and the unsaturated hydrocarbons $c\text{-C}_3\text{H}_2$ and HC_3N are over-abundant in IRS7B. This makes IRS7B similar to the warm carbon-chain chemistry sources, but considering that the C_2H abundance is an order of magnitude higher in L1527 than in IRS7B and that a very low upper limit of the C_4H abundance in IRS7B was measured by Sakai et al. (2009a), IRS7B is not likely to be a typical WCCC source. Rather, the detected molecular abundances reflect a PDR-like chemistry resulting from the strong irradiation onto the molecular envelope from R CrA.

The CH_3OH abundance observed towards IRS7B is only around $3\text{--}6 \times 10^{-9}$ (we calculated this indirectly using the rotational diagram column density of CH_3OH and the rotational diagram column densities and RATRAN abundances of HNCO and $c\text{-C}_3\text{H}_2$). This is very low when compared to hot corino abundances (3×10^{-7} in IRAS 16293-2422; Cazaux et al. 2003) and could be explained by the elevated temperature in the region, which inhibits grain formation of CH_3OH due to evaporation of both CO and H atoms. The low abundances of CH_3OCHO and CH_3OCH_3 relative to CH_3OH can be explained if we assume that these molecules are generally formed through gas-phase reactions (see, e.g., Charnley 1997; Peeters et al. 2006). In this scenario, a CH_3OH abundance $\lesssim 10^{-8}$ is too low for an efficient formation of these molecules (Taquet et al., in prep.). H_2CCO and CH_3CHO are, on the other hand, more likely to form on grains (Charnley 2001) and should form at a rate similar to CH_3OH , which could explain why the $\text{H}_2\text{CCO}/\text{CH}_3\text{OH}$ and $\text{CH}_3\text{CHO}/\text{CH}_3\text{OH}$ ratios are similar to what is found in IRAS 16293-2422. Another possibility is that the tentatively detected complex molecules could exist in a more shielded inner region, at temperatures at the same levels as those of the hydrocarbon molecules (10–15 K), similar to the properties of the complex organic molecules detected in the prestellar core L1689B (Bacmann et al. 2012). If, on the other hand, we assume a grain-formation scenario for all complex organic molecules,

³ <http://caravan.astro.wisc.edu/protostars/>

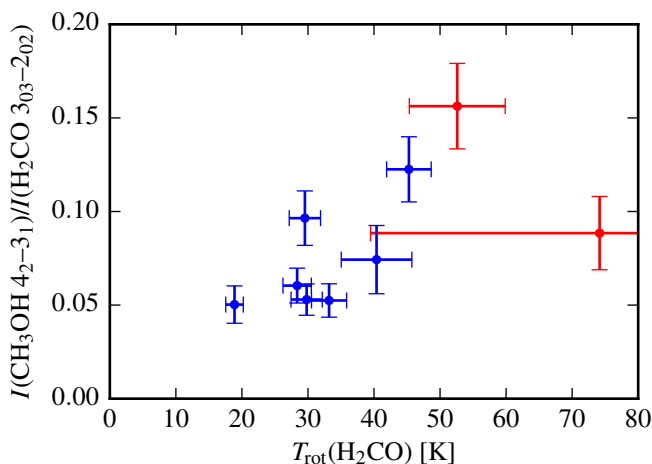


Fig. 13. As a proxy for the $\text{CH}_3\text{OH}/\text{H}_2\text{CO}$ abundance ratio, we here show the line ratio between the $\text{CH}_3\text{OH } 4_2 \rightarrow 3_1$, E line at 218.440 GHz and the $\text{H}_2\text{CO } 3_{03} \rightarrow 2_{02}$ line at 218.222 GHz in the CrA sources as a function of the H_2CO rotational temperature. CrA-24 and SMM 2 are shown with two data points each, one for the on-source component (blue) and one for the outflow component (red). (A colour version of this plot is available in the online journal.)

the elevated temperatures should enhance the formation of complex organic molecules as long as precursor molecules such as H_2CO exist on the icy grains (Garrod & Herbst 2006). The CH_3CN found towards protostellar envelopes is believed to be formed from gas-phase reactions between HCN and CH_3^+ (Rodgers & Charnley 2001; Wang et al. 2010). The low CH_3CN abundance and high CN and DCN abundances observed towards IRS7B are thus puzzling, but might be due to a relative lack of CH_4 , the precursor species of CH_3^+ . The exact reason for a low CH_3CN abundance needs to be further investigated.

Laboratory experiments (Watanabe et al. 2004; Fuchs et al. 2009) and numerical simulations (Cuppen et al. 2009) have suggested that the hydrogenation reactions of CO forming H_2CO and CH_3OH on CO- H_2O ices are strongly temperature dependent, with the $\text{CH}_3\text{OH}/\text{H}_2\text{CO}$ ratio increasing significantly at relatively small increases in temperature. Since the CH_3OH rotational diagrams of the source survey have too few data points to be reliable (see Sect. 4.2), we did not use the $\text{CH}_3\text{OH}/\text{H}_2\text{CO}$ abundance ratio, but instead used the ratio between the $\text{CH}_3\text{OH } 4_2 \rightarrow 3_1$, E line at 218.440 GHz and the $\text{H}_2\text{CO } 3_{03} \rightarrow 2_{02}$ line at 218.222 GHz as a more useful proxy for the $\text{CH}_3\text{OH}/\text{H}_2\text{CO}$ abundance ratio. We compare this ratio with the H_2CO rotational temperature in Fig. 13 and see a positive trend between the $\text{CH}_3\text{OH}/\text{H}_2\text{CO}$ ratio and the H_2CO temperature. We suggest that the high level of irradiation has caused most of the CO to evaporate from the ices in the whole region around R CrA, which has caused the relatively low CH_3OH abundances (see above). However, the low amounts of CO that are still left on the grain surfaces will form CH_3OH more efficiently in the warmest protostellar envelopes, causing the trend in Fig. 13. This effect should be strongest at $T < 20$ K (Watanabe et al. 2003), but the trend observed above 20 K could be explained if the CH_3OH now observed in the gas phase was formed on the icy grains at a time when R CrA was less luminous than today.

Lindberg & Jørgensen (2012) found that the embedded protostellar sources in the R CrA cloud are encompassed by dense molecular gas traced by ridges of H_2CO on scales of at least 5 000 AU. A large part of the emission observed in the APEX

beam centred at IRS7B is expected to originate in these ridges. Towards CrA-24 and SMM 2, we find signs of large-scale H_2CO and CH_3OH gas at velocities somewhat lower than the typical v_{LSR} of the sources in the CrA region. This is consistent with CH_3OH emission extending towards the northeast from the R CrA cloud observed in SEST CH_3OH maps (Miettinen et al., in prep.). A schematic drawing of the distribution of dense molecular gas, dust emission, and YSOs in the vicinity of R CrA is shown in Fig. 14. A direct comparison with the typical hot corino sources might therefore be argued against, because in such sources the emission from complex organic molecules originates in relatively compact regions close to the central source (e.g. Kuan et al. 2004; Bottinelli et al. 2004b, 2008; Bisschop et al. 2008). However, Lindberg et al. (2014a) separated the faint CH_3OH emission originating in the IRS7B central source from the surrounding emission using high-resolution ALMA interferometry data. The faint on-source CH_3OH lines can either be explained by a very low CH_3OH abundance in the inner envelope ($X(\text{CH}_3\text{OH}) \sim 10^{-10}$; an order of magnitude lower than the already low large-scale CH_3OH abundance), or by a more typical CH_3OH abundance in the inner envelope ($X(\text{CH}_3\text{OH}) \sim 10^{-8}$) in combination with a flattened density profile in the inner 100 AU caused by the presence of a Keplerian disc. This latter case would still allow for a higher CH_3OH abundance and the presence of more complex organic molecules in the inner envelope of IRS7B at similar abundances as found in hot corinos. Chemical modelling of the irradiated envelope and ALMA observations with higher sensitivity and resolution will help clarify the causes of the chemistry observed towards IRS7B and the inner structure of the source.

6. Conclusions

We have performed an unbiased line survey of the Class 0/I source R CrA IRS7B to investigate its chemical and physical properties. We also presented a survey of the H_2CO , CH_3OH , and $c\text{-C}_3\text{H}_2$ emission for the full sample of embedded YSOs in the Corona Australis region. The observations were carried out with the (sub)millimetre single-dish APEX telescope, but we also used supplementary data from the ASTE telescope. These are our main conclusions:

1. In comparison with other well-studied Class 0/I sources, the deeply embedded YSO IRS7B shows a different chemistry. In particular, very strong CN emission is seen, which indicates a PDR-like chemistry. The only signs of complex organic molecules or large carbon-chain species detected towards IRS7B are CH_3OH , CH_3CCH , and faint CH_3CN and CH_3CHO emission. The CH_3OH abundance is also very low ($3\text{--}6 \times 10^{-9}$) in comparison with other embedded protostars. The values or estimated upper limits of the abundances of several complex organic species relative to CH_3OH are much lower than the relative abundances detected towards typical hot corino sources, while species such as CN , HC_3N , and $c\text{-C}_3\text{H}_2$ show strongly elevated relative abundances. High-resolution ALMA observations have also failed to detect complex organics on smaller scales (Lindberg et al. 2014a).
2. The molecules detected towards R CrA IRS7B can be grouped into two categories by their rotational temperatures: the warm carbon-chain molecules and nitrogen-bearing species show temperatures around 10–17 K, whereas the organic molecules and sulphur-bearing species are warmer

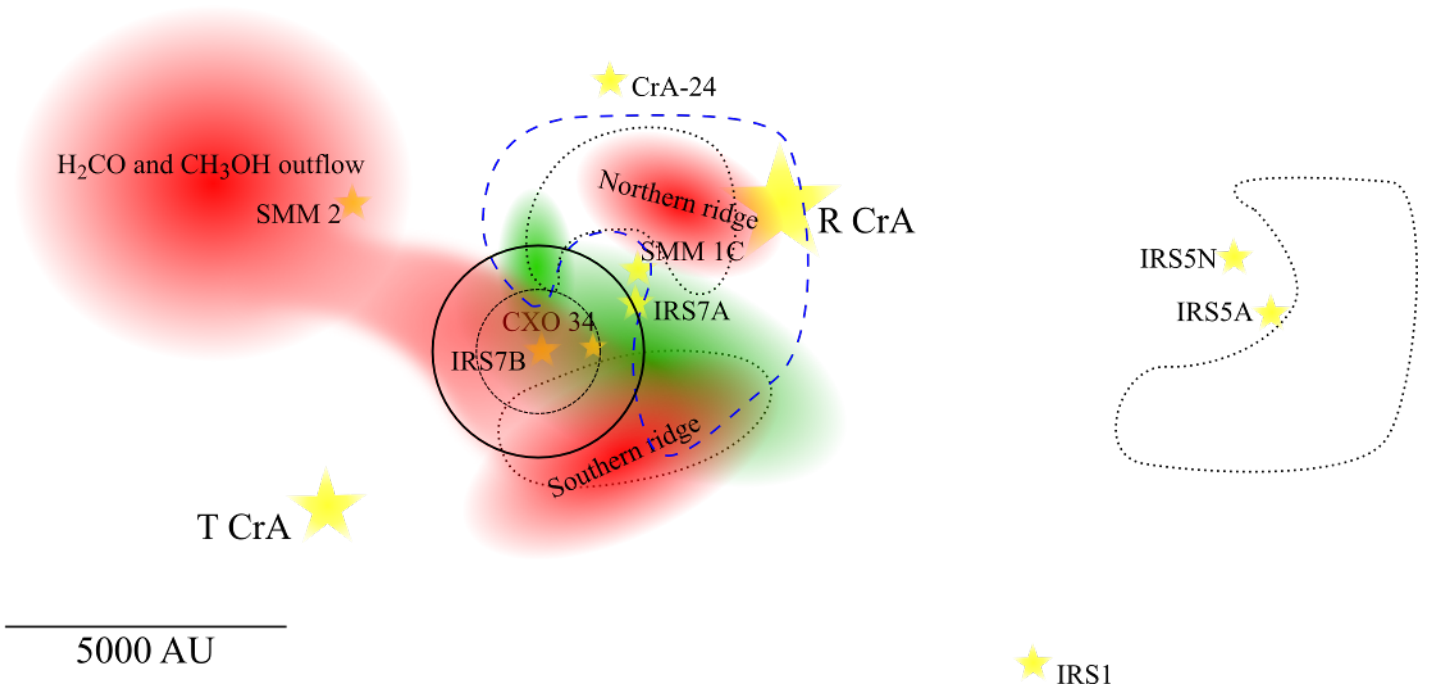


Fig. 14. Schematic drawing of the R CrA cloud and its surroundings. Protostars are shown in yellow. Red structures indicate extended H_2CO and CH_3OH emission, and blue striped structures show extended emission from hydrocarbon and nitrogen-bearing species (Miettinen et al., in prep.; Lindberg & Jørgensen 2012). The brown dashed contour shows extended high- J ($J \sim 20$) CO emission, and the black dotted contours show extended $110\ \mu\text{m}$ dust continuum emission not associated with the point sources (from *Herschel* PACS observations; Lindberg et al. 2014b). The solid black circle shows the APEX beam at 218 GHz centred at IRS7B, and the dashed black circle shows the APEX beam at 363 GHz. Large parts of the region have not been covered by all observation modes, and thus the map is probably incomplete. This map covers only a small part of the sources in the CrA source survey (cf. Fig. 1). (A colour version of this plot is available in the online journal.)

at 19–40 K. Molecules from the two groups have previously been found to have distinct spatial distributions in SMA/APEX interferometry observations of the region (Lindberg & Jørgensen 2012).

3. The H_2CO rotational temperatures of the sources in the CrA survey near the Herbig Be star R CrA are elevated to 30–50 K, and the H_2CO temperature is also found to decrease with the distance to R CrA. This temperature gradient is consistent with a 1-D radiative transfer model with R CrA as the heating source. The H_2CO temperatures of the outflow components of the sources with two velocity components are higher than the corresponding on-source component temperatures. The $c\text{-C}_3\text{H}_2$ rotational temperatures are on the other hand found to be fairly constant around 10–15 K for all sources where it could be measured. This could be a shielding effect as a result of the $c\text{-C}_3\text{H}_2$ being present at much smaller spatial scales than the H_2CO .
4. The $\text{CH}_3\text{OH}/\text{H}_2\text{CO}$ is found to increase with the H_2CO rotational temperature. This can be explained by the higher temperature increasing the efficiency of hydrogenation reactions of CO, as suggested by laboratory studies.

We have shown that the chemistry of protostellar envelopes can be strongly influenced by external irradiation. Follow-up studies with interferometric observations are needed to reveal the different origins of various organic molecules and unsaturated hydrocarbons in protostellar envelopes. To understand why the abundance levels of some but not all organic molecules are lowered, their exact formation paths need to be studied using astrochemical modelling, in particular assuming elevated temperatures on large scales.

Acknowledgements. We thank Steven Charnley for helpful suggestions and discussions. We also thank the anonymous referee for helpful comments and sug-

gestions that have improved the manuscript. Research at Centre for Star and Planet Formation is funded by the Danish National Research Foundation and the University of Copenhagen's programme of excellence. This research was also supported by an appointment to the NASA Postdoctoral Program at the NASA Goddard Space Flight Center to J.E.L., administered by Oak Ridge Associated Universities through a contract with NASA, and by a Lundbeck Foundation Group Leader Fellowship to J.K.J. Y.W. N.S. and S.Y. acknowledge financial support from Grant-in-Aid from the Ministry of Education, Culture, Sports, Science, and Technologies of Japan (25108005).

References

- Adams, F. C. & Shu, F. H. 1985, *ApJ*, 296, 655
 Agúndez, M., Cernicharo, J., Guélin, M., et al. 2008, *A&A*, 478, L19
 Arce, H. G., Santiago-García, J., Jørgensen, J. K., Tafalla, M., & Bachiller, R. 2008, *ApJ*, 681, L21
 Bachiller, R., Codella, C., Colomer, F., Liechti, S., & Walmsley, C. M. 1998, *A&A*, 335, 266
 Bachiller, R., Liechti, S., Walmsley, C. M., & Colomer, F. 1995, *A&A*, 295, L51
 Bachiller, R. & Pérez Gutiérrez, M. 1997, *ApJ*, 487, L93
 Bacmann, A., Taquet, V., Faure, A., Kahane, C., & Ceccarelli, C. 2012, *A&A*, 541, L12
 Bisschop, S. E., Jørgensen, J. K., Bourke, T. L., Bottinelli, S., & van Dishoeck, E. F. 2008, *A&A*, 488, 959
 Bisschop, S. E., Schilke, P., Wyrowski, F., et al. 2013, *A&A*, 552, A122
 Blake, G. A., van Dishoeck, E. F., Jansen, D. J., Groesbeck, T. D., & Mundy, L. G. 1994, *ApJ*, 428, 680
 Bottinelli, S., Ceccarelli, C., Lefloch, B., et al. 2004a, *ApJ*, 615, 354
 Bottinelli, S., Ceccarelli, C., Neri, R., & Williams, J. P. 2008, in *IAU Symposium*, Vol. 251, IAU Symposium, ed. S. Kwok & S. Sanford, 117–118
 Bottinelli, S., Ceccarelli, C., Neri, R., et al. 2004b, *ApJ*, 617, L69
 Bottinelli, S., Ceccarelli, C., Williams, J. P., & Lefloch, B. 2007, *A&A*, 463, 601
 Caux, E., Kahane, C., Castets, A., et al. 2011, *A&A*, 532, A23
 Cazaux, S., Tielens, A. G. G. M., Ceccarelli, C., et al. 2003, *ApJ*, 593, L51
 Ceccarelli, C. 2004, in *Astronomical Society of the Pacific Conference Series*, Vol. 323, *Star Formation in the Interstellar Medium: In Honor of David Hollenbach*, ed. D. Johnstone, F. C. Adams, D. N. C. Lin, D. A. Neufeld, & E. C. Ostriker, 195

- Charnley, S. B. 1997, in *IAU Colloq. 161: Astronomical and Biochemical Origins and the Search for Life in the Universe*, ed. C. Batalli Cosmovici, S. Bowyer, & D. Werthimer, 89
- Charnley, S. B. 2001, in *The Bridge Between the Big Bang and Biology: Stars, Planetary Systems, Atmospheres, Volcanoes: Their Link to Life*, ed. F. Giovannelli, 139
- Chin, Y.-N., Henkel, C., Whiteoak, J. B., Langer, N., & Churchwell, E. B. 1996, *A&A*, 305, 960
- Cuadrado, S., Goicoechea, J. R., Pilleri, P., et al. 2015, *A&A*, 575, A82
- Cuppen, H. M., van Dishoeck, E. F., Herbst, E., & Tielens, A. G. G. M. 2009, *A&A*, 508, 275
- Dickens, J. E. & Irvine, W. M. 1999, *ApJ*, 518, 733
- Dullemond, C. P., van Zadelhoff, G. J., & Natta, A. 2002, *A&A*, 389, 464
- Fuchs, G. W., Cuppen, H. M., Ioppolo, S., et al. 2009, *A&A*, 505, 629
- Garrod, R. T. & Herbst, E. 2006, *A&A*, 457, 927
- Goldsmith, P. F. & Langer, W. D. 1999, *ApJ*, 517, 209
- Green, S. 1991, *ApJS*, 76, 979
- Greene, T. P., Wilking, B. A., Andre, P., Young, E. T., & Lada, C. J. 1994, *ApJ*, 434, 614
- Güsten, R., Nyman, L. Å., Schilke, P., et al. 2006, *A&A*, 454, L13
- Guzmán, V. V., Pety, J., Goicoechea, J. R., et al. 2015, *ApJ*, 800, L33
- Hassel, G. E., Herbst, E., & Garrod, R. T. 2008, *ApJ*, 681, 1385
- Herbst, E. & van Dishoeck, E. F. 2009, *ARA&A*, 47, 427
- Hogerheijde, M. R. & van der Tak, F. F. S. 2000, *A&A*, 362, 697
- Jansen, D. J. 1995, PhD thesis, Leiden Observatory, Leiden University, P.O. Box 9513, 2300 RA Leiden, The Netherlands
- Jørgensen, J. K., Bourke, T. L., Myers, P. C., et al. 2005a, *ApJ*, 632, 973
- Jørgensen, J. K., Schöier, F. L., & van Dishoeck, E. F. 2004, *A&A*, 416, 603
- Jørgensen, J. K., Schöier, F. L., & van Dishoeck, E. F. 2005b, *A&A*, 437, 501
- Kuan, Y.-J., Huang, H.-C., Charnley, S. B., et al. 2004, *ApJ*, 616, L27
- Lindberg, J. E. & Jørgensen, J. K. 2012, *A&A*, 548, A24
- Lindberg, J. E., Jørgensen, J. K., Brinch, C., et al. 2014a, *A&A*, 566, A74
- Lindberg, J. E., Jørgensen, J. K., Green, J. D., et al. 2014b, *A&A*, 565, A29
- Lucas, R. & Liszt, H. S. 2000, *A&A*, 358, 1069
- Mangum, J. G. & Wootten, A. 1993, *ApJS*, 89, 123
- Mauray, A. J., Belloche, A., André, P., et al. 2014, *A&A*, 563, L2
- Minh, Y. C., Irvine, W. M., & Brewer, M. K. 1991, *A&A*, 244, 181
- Montillaud, J., Joblin, C., & Toubanc, D. 2013, *A&A*, 552, A15
- Müller, H. S. P., Thorwirth, S., Roth, D. A., & Winnewisser, G. 2001, *A&A*, 370, L49
- Neuhäuser, R. & Forbrich, J. 2008, in *Handbook of Star Forming Regions, Volume II: The Southern Sky*, ed. Reipurth, B. (ASP Monographs; San Francisco, CA; ASP), 735
- Öberg, K. I., Bottinelli, S., Jørgensen, J. K., & van Dishoeck, E. F. 2010, *ApJ*, 716, 825
- Ohishi, M., Kawaguchi, K., Kaifu, N., et al. 1991, in *Astronomical Society of the Pacific Conference Series, Vol. 16, Atoms, Ions and Molecules: New Results in Spectral Line Astrophysics*, ed. A. D. Haschick & P. T. P. Ho, 387
- Parise, B., Ceccarelli, C., Tielens, A. G. G. M., et al. 2006, *A&A*, 453, 949
- Peeters, Z., Rodgers, S. D., Charnley, S. B., et al. 2006, *A&A*, 445, 197
- Peterson, D. E., Caratti o Garatti, A., Bourke, T. L., et al. 2011, *ApJS*, 194, 43
- Pickett, H. M., Poynter, R. L., Cohen, E. A., et al. 1998, *J. Quant. Spec. Radiat. Transf.*, 60, 883
- Robitaille, T. P., Whitney, B. A., Indebetouw, R., & Wood, K. 2007, *ApJS*, 169, 328
- Robitaille, T. P., Whitney, B. A., Indebetouw, R., Wood, K., & Denzmore, P. 2006, *ApJS*, 167, 256
- Rodgers, S. D. & Charnley, S. B. 2001, *ApJ*, 546, 324
- Rodgers, S. D. & Charnley, S. B. 2002, *Planet. Space Sci.*, 50, 1125
- Sakai, N., Sakai, T., Hirota, T., Burton, M., & Yamamoto, S. 2009a, *ApJ*, 697, 769
- Sakai, N., Sakai, T., Hirota, T., & Yamamoto, S. 2008, *ApJ*, 672, 371
- Sakai, N., Sakai, T., Hirota, T., & Yamamoto, S. 2009b, *ApJ*, 702, 1025
- Sakai, N., Sakai, T., Hirota, T., & Yamamoto, S. 2010, *ApJ*, 722, 1633
- Sakai, N. & Yamamoto, S. 2013, *Chemical Reviews*, 113, 8981
- Schöier, F. L., Jørgensen, J. K., van Dishoeck, E. F., & Blake, G. A. 2002, *A&A*, 390, 1001
- Schöier, F. L., van der Tak, F. F. S., van Dishoeck, E. F., & Black, J. H. 2005, *A&A*, 432, 369
- Sicilia-Aguilar, A., Henning, T., Linz, H., et al. 2013, *A&A*, 551, A34
- Turner, B. E. 1990, *ApJ*, 362, L29
- van der Tak, F. F. S., Black, J. H., Schöier, F. L., Jansen, D. J., & van Dishoeck, E. F. 2007, *A&A*, 468, 627
- van Dishoeck, E. F., Blake, G. A., Jansen, D. J., & Groesbeck, T. D. 1995, *ApJ*, 447, 760
- Vassilev, V., Meledin, D., Lapkin, I., et al. 2008, *A&A*, 490, 1157
- Wampfler, S. F., Jørgensen, J. K., Bizzarro, M., & Bisschop, S. E. 2014, *A&A*, 572, A24
- Wang, K.-S., Kuan, Y.-J., Liu, S.-Y., & Charnley, S. B. 2010, *ApJ*, 713, 1192
- Watanabe, N., Nagaoka, A., Shiraki, T., & Kouchi, A. 2004, *ApJ*, 616, 638
- Watanabe, N., Shiraki, T., & Kouchi, A. 2003, *ApJ*, 588, L121
- Watanabe, Y., Sakai, N., Lindberg, J. E., et al. 2012, *ApJ*, 745, 126
- Wiesenfeld, L. & Faure, A. 2013, *MNRAS*, 432, 2573
- Wilson, T. L. 1999, *Reports on Progress in Physics*, 62, 143

Appendix A: Baseline subtraction

As noted in Sect. 2, the spectra observed by APEX exhibit unstable quasi-sinusoidal baselines (see Vassilev et al. 2008). When investigating the spectra, we found that polynomial and/or sinusoidal baselines were not giving desirable results. To account for this, we developed a relatively advanced baseline-fitting algorithm, computing running-mean baselines, which is described here.

In principle, the fitted baseline is a boxcar smoothing of the spectrum (where line channels have been removed) with weights increasing towards the centre of the box: For each channel in the spectrum, the algorithm calculates the weighted mean of the line-free channels in a box around the channel. The weights have a Gaussian distribution around the central channel of the box. The width of this Gaussian must be adjusted so that all irregularities in the baseline are removed but no real spectral features are removed. In addition to the quasi-sinusoidal baselines, strong atmospheric lines arising from the different elevations of the position-switching on- and off-positions made it necessary to introduce discontinuities in the fitted baseline. By this method, a piecewise smooth but in general non-analytical baseline can be fitted to the data (see examples in Fig. A.1). Some artefacts of the strongest of these atmospheric lines still remain after the baseline subtraction and appear as broad spectral line features in the resulting spectra. In this dataset, they are easy to distinguish from the source lines due to the large difference in line widths.

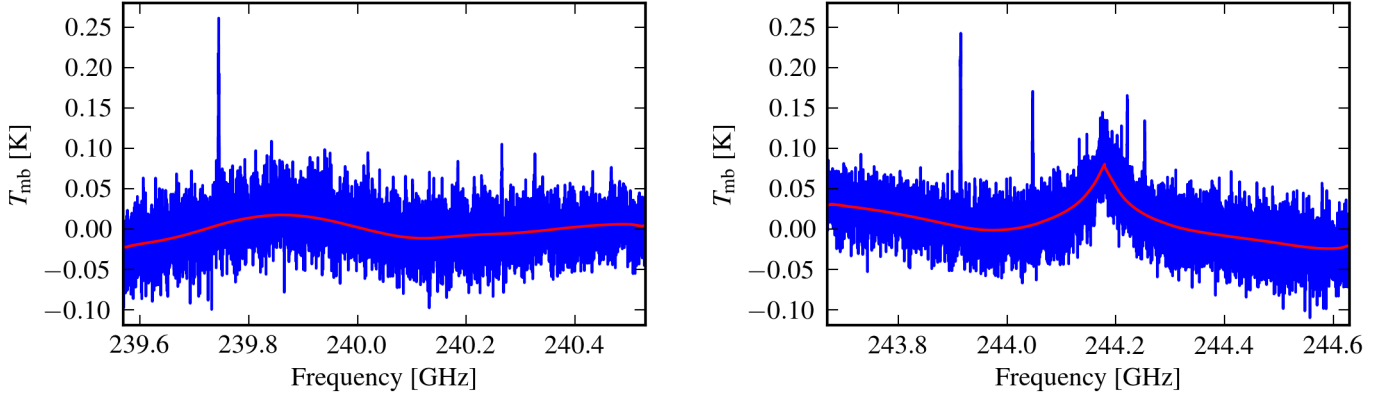


Fig. A.1. Examples of spectral data before they were treated by the running-mean baseline-fitting routine (blue) and the fitted baseline that was subsequently subtracted (red). The right spectrum has a discontinuity in the fitted baseline that is due to an atmospheric line. (A colour version of this plot is available in the online journal.)

Appendix B: Observed spectral line parameters

The integrated intensities and other parameters of the detected spectral lines are listed in the tables of this appendix. The values of v_{LSR} , Δv , and T_{peak} are results of Gaussian fits. In the cases where no values are given, Gaussian fits could not be performed to that line because of irregular line shapes.

Table B.1. Observed line strengths towards IRS7B, both for the 1.3 mm unbiased line survey and for the IRS7B part of the source survey, which also covered the 0.9 mm and 0.8 mm windows.

Frequency ^a [MHz]	Molecule	Transition	v_{LSR} [km s ⁻¹]	Δv [km s ⁻¹]	T_{mb} [K]	$\int T_{\text{mb}} dv$ [K km s ⁻¹]
217238.538	DCN	$J = 3 \rightarrow 2$	6.1	1.8	1.04	2.01 ± 0.07
217467.150	¹³ CN	$N = 2 \rightarrow 1, J = 5/2 \rightarrow 3/2, F_1 = 3 \rightarrow 2, F = 4 \rightarrow 3$	5.8	0.9	0.24	0.24 ± 0.05
217467.150	¹³ CN	$N = 2 \rightarrow 1, J = 5/2 \rightarrow 3/2, F_1 = 3 \rightarrow 2, F = 3 \rightarrow 2$
217822.148	<i>c</i> -C ₃ H ₂	$6_{06} \rightarrow 5_{15}$	5.8	1.6	0.95	1.68 ± 0.07
217822.148	<i>c</i> -C ₃ H ₂	$6_{16} \rightarrow 5_{05}$
217880.232	U	1.4	0.44	0.66 ± 0.02
217940.046	<i>c</i> -C ₃ H ₂	$5_{14} \rightarrow 4_{23}$	5.7	1.5	0.51	0.83 ± 0.02
218160.456	<i>c</i> -C ₃ H ₂	$5_{24} \rightarrow 4_{13}$	5.7	1.5	0.23	0.36 ± 0.02
218222.192	H ₂ CO	$3_{03} \rightarrow 2_{02}$	5.9	2.4	6.27	16.09 ± 0.03
218324.723	HC ₃ N	$J = 24 \rightarrow 23$	6.1	1.4	0.55	0.81 ± 0.02
218440.063	CH ₃ OH	$4_2 \rightarrow 3_1, E$	5.8	2.1	0.88	1.97 ± 0.03
218475.632	H ₂ CO	$3_{22} \rightarrow 2_{21}$	5.9	2.2	1.52	3.61 ± 0.03
218732.732	<i>c</i> -C ₃ H ₂	$7_{16} \rightarrow 7_{07}$	5.8	1.6	0.05	0.11 ± 0.02
218732.732	<i>c</i> -C ₃ H ₂	$7_{26} \rightarrow 7_{17}$
218760.066	H ₂ CO	$3_{21} \rightarrow 2_{20}$	5.9	2.2	1.35	3.22 ± 0.03
219560.354	C ¹⁸ O	$J = 2 \rightarrow 1$	20.34 ± 0.04
219798.274	HNCO	$10_{0,10} \rightarrow 9_{0,9}$	5.8	2.3	0.13	0.29 ± 0.02
219908.525	H ₂ ¹³ CO	$3_{12} \rightarrow 2_{11}$	5.9	2.1	0.24	0.54 ± 0.02

219934.040	C ¹⁵ N	$N = 2 \rightarrow 1, J = 5/2 \rightarrow 3/2, F = 2 \rightarrow 1$...	4.5	0.03	0.14 ± 0.02
219934.820	C ¹⁵ N	$N = 2 \rightarrow 1, J = 5/2 \rightarrow 3/2, F = 3 \rightarrow 2$
219949.442	SO	$6_5 \rightarrow 5_4$	5.7	2.6	1.96	5.66 ± 0.03
220078.561	CH ₃ OH	$8_0 \rightarrow 7_1, E$	6.6	3.5	0.06	0.19 ± 0.02
220177.569	H ₂ CCO	$11_{1,11} \rightarrow 10_{1,10}$	5.8	0.8	0.10	0.12 ± 0.02
220188.265	U	0.5	0.10	0.04 ± 0.01
220398.684	¹³ CO	$J = 2 \rightarrow 1$	59.75 ± 0.05
220743.011	CH ₃ CN	$12_1 \rightarrow 11_1$	6.1	1.5	0.07	0.12 ± 0.02
220747.261	CH ₃ CN	$12_0 \rightarrow 11_0$	6.1	2.8	0.05	0.11 ± 0.02
221191.665	D ₂ CO	$4_{14} \rightarrow 3_{13}$	6.0	1.5	0.13	0.20 ± 0.02
221965.220	SO ₂	$11_{1,11} \rightarrow 10_{0,10}$	5.3	2.5	0.23	0.60 ± 0.02
222128.815	CH ₃ CCH	$13_3 \rightarrow 12_3$	6.0	1.2	0.11	0.14 ± 0.02
222150.010	CH ₃ CCH	$13_2 \rightarrow 12_2$	5.9	1.3	0.19	0.25 ± 0.01
222162.730	CH ₃ CCH	$13_1 \rightarrow 12_1$	5.9	1.5	0.31	0.47 ± 0.02
222166.971	CH ₃ CCH	$13_0 \rightarrow 12_0$	5.9	1.6	0.36	0.58 ± 0.02
223756.396	U	0.6	0.08	0.06 ± 0.02
224327.250	H ₂ CCO	$11_{1,10} \rightarrow 10_{1,9}$	5.8	1.5	0.09	0.14 ± 0.02
224714.187	C ¹⁷ O	$J = 2 \rightarrow 1$	5.2	2.2	2.35	6.00 ± 0.03
225153.704	SO ₂	$13_{2,12} \rightarrow 13_{1,13}$	5.2	2.3	0.06	0.15 ± 0.02
225159.616	U	1.5	0.05	0.07 ± 0.02
225697.775	H ₂ CO	$3_{12} \rightarrow 2_{11}$	5.8	2.5	6.59	19.34 ± 0.04
226004.854	U	3.5	0.09	0.31 ± 0.03
226287.418	CN	$N = 2 \rightarrow 1, J = 3/2 \rightarrow 3/2, F = 1/2 \rightarrow 1/2$	5.6	2.1	0.15	0.32 ± 0.02
226298.943	CN	$N = 2 \rightarrow 1, J = 3/2 \rightarrow 3/2, F = 1/2 \rightarrow 3/2$	5.2	2.8	0.11	0.29 ± 0.02
226303.037	CN	$N = 2 \rightarrow 1, J = 3/2 \rightarrow 3/2, F = 3/2 \rightarrow 1/2$	5.6	2.0	0.14	0.29 ± 0.02
226314.540	CN	$N = 2 \rightarrow 1, J = 3/2 \rightarrow 3/2, F = 3/2 \rightarrow 3/2$	5.6	1.8	0.33	0.63 ± 0.03
226332.499	CN	$N = 2 \rightarrow 1, J = 3/2 \rightarrow 3/2, F = 3/2 \rightarrow 5/2$	5.6	2.0	0.14	0.31 ± 0.02
226341.930	CN	$N = 2 \rightarrow 1, J = 3/2 \rightarrow 3/2, F = 5/2 \rightarrow 3/2$	5.4	1.6	0.19	0.32 ± 0.02
226359.871	CN	$N = 2 \rightarrow 1, J = 3/2 \rightarrow 3/2, F = 5/2 \rightarrow 5/2$	5.6	1.9	0.77	1.66 ± 0.03
226551.622	CH ₃ CHO	$12_{0,12} \rightarrow 11_{0,11}, E$	5.2	2.6	0.06	0.17 ± 0.03
226592.725	CH ₃ CHO	$12_{0,12} \rightarrow 11_{0,11}, A$	5.6	2.0	0.04	0.08 ± 0.02
226616.571	CN	$N = 2 \rightarrow 1, J = 3/2 \rightarrow 1/2, F = 1/2 \rightarrow 3/2$	5.6	2.1	0.16	0.37 ± 0.03
226632.190	CN	$N = 2 \rightarrow 1, J = 3/2 \rightarrow 1/2, F = 3/2 \rightarrow 3/2$	5.7	2.1	1.06	2.40 ± 0.03
226659.558	CN	$N = 2 \rightarrow 1, J = 3/2 \rightarrow 1/2, F = 5/2 \rightarrow 3/2$	5.8	2.3	2.44	6.53 ± 0.04
226663.693	CN	$N = 2 \rightarrow 1, J = 3/2 \rightarrow 1/2, F = 1/2 \rightarrow 1/2$	5.8	2.3	0.96	2.33 ± 0.03
226679.311	CN	$N = 2 \rightarrow 1, J = 3/2 \rightarrow 1/2, F = 3/2 \rightarrow 1/2$	5.7	2.1	1.22	2.80 ± 0.03
226823.149	U	2.7	0.06	0.15 ± 0.02
226838.423	U	2.7	0.03	0.08 ± 0.02
226843.364	U	2.3	0.07	0.17 ± 0.03
226874.191	CN	$N = 2 \rightarrow 1, J = 5/2 \rightarrow 3/2, F = 5/2 \rightarrow 3/2$...	3.9	3.50	15.14 ± 0.05
226874.781	CN	$N = 2 \rightarrow 1, J = 5/2 \rightarrow 3/2, F = 7/2 \rightarrow 5/2$
226875.896	CN	$N = 2 \rightarrow 1, J = 5/2 \rightarrow 3/2, F = 3/2 \rightarrow 1/2$
226887.420	CN	$N = 2 \rightarrow 1, J = 5/2 \rightarrow 3/2, F = 3/2 \rightarrow 3/2$	5.7	2.0	0.72	1.55 ± 0.03
226892.128	CN	$N = 2 \rightarrow 1, J = 5/2 \rightarrow 3/2, F = 5/2 \rightarrow 5/2$	5.6	2.0	0.84	1.80 ± 0.03
227169.138	c-C ₃ H ₂	$4_{32} \rightarrow 3_{21}$	5.6	1.5	0.50	0.80 ± 0.03
227418.905	HC ₃ N	$J = 25 \rightarrow 24$	6.0	1.4	0.34	0.47 ± 0.02
228910.481	DNC	$J = 3 \rightarrow 2$	5.7	1.5	0.67	1.02 ± 0.02
229758.756	CH ₃ OH	$8_{-1} \rightarrow 7_0, E$	5.3	2.2	0.23	0.54 ± 0.02
229775.966	U	1.1	0.05	0.06 ± 0.01
230538.000	CO	$J = 2 \rightarrow 1$	381.24 ± 0.06
231220.685	¹³ CS	$J = 5 \rightarrow 4$	5.2	2.0	0.23	0.48 ± 0.02
231410.234	D ₂ CO	$4_{04} \rightarrow 3_{03}$	5.5	1.8	0.14	0.24 ± 0.02
233455.410	U	1.9	0.06	0.11 ± 0.03
235151.720	SO ₂	$4_{22} \rightarrow 3_{13}$	5.0	2.6	0.08	0.17 ± 0.02
235774.099	CH ₃ CHO	$3_{3,1} \rightarrow 3_{2,2}, A$	5.3	1.0	0.05	0.05 ± 0.01
235816.499	U	0.9	0.06	0.05 ± 0.02
236102.086	D ₂ CO	$4_{22} \rightarrow 3_{21}$	5.8	1.7	0.10	0.16 ± 0.02
236512.789	HC ₃ N	$J = 26 \rightarrow 25$	5.9	2.0	0.11	0.22 ± 0.02
236727.020	H ₂ CS	$7_{17} \rightarrow 6_{16}$	5.6	1.9	0.16	0.34 ± 0.02
237068.833	SO ₂	$12_{3,9} \rightarrow 12_{2,10}$	5.8	4.8	0.04	0.10 ± 0.02
237433.168	U	3.4	0.09	0.32 ± 0.03
237998.265	U	2.7	0.10	0.26 ± 0.03
238609.987	U	2.0	0.16	0.32 ± 0.02
239211.215	CH ₃ CCH	$14_3 \rightarrow 13_3$	5.9	1.2	0.11	0.14 ± 0.02
239234.034	CH ₃ CCH	$14_2 \rightarrow 13_2$	5.8	1.5	0.13	0.20 ± 0.02
239247.728	CH ₃ CCH	$14_1 \rightarrow 13_1$	5.8	1.5	0.27	0.40 ± 0.02
239252.294	CH ₃ CCH	$14_0 \rightarrow 13_0$	5.9	1.4	0.32	0.46 ± 0.02
239746.219	CH ₃ OH	$5_1 \rightarrow 4_1, A+$	5.6	2.4	0.28	0.70 ± 0.03
240020.626	U	2.4	0.07	0.16 ± 0.02
240185.794	H ₂ CCO	$12_{1,12} \rightarrow 11_{1,11}$	5.9	1.6	0.09	0.15 ± 0.02

240266.872	H ₂ CS	7 ₀₇ → 6 ₀₆	5.6	2.1	0.13	0.29 ± 0.02
241016.089	C ³⁴ S	J = 5 → 4	5.7	1.8	0.86	1.68 ± 0.03
241615.797	SO ₂	5 ₂₄ → 4 ₁₃	5.5	2.2	0.16	0.39 ± 0.03
241700.159	CH ₃ OH	5 ₀ → 4 ₀ , E	5.7	2.2	0.50	1.12 ± 0.03
241767.234	CH ₃ OH	5 ₋₁ → 4 ₋₁ , E	5.6	2.2	1.27	3.17 ± 0.04
241774.032	HNCO	11 _{0,11} → 10 _{0,10}	5.7	2.0	0.09	0.23 ± 0.03
241791.352	CH ₃ OH	5 ₀ → 4 ₀ , A+	5.6	2.2	1.50	3.80 ± 0.05
241832.718	CH ₃ OH	5 ₃ → 4 ₃ , A+	...	1.7	0.06	0.12 ± 0.03
241833.106	CH ₃ OH	5 ₋₃ → 4 ₋₃ , A-
241842.284	CH ₃ OH	5 ₋₂ → 4 ₋₂ , A-	...	2.8	0.05	0.12 ± 0.02
241843.604	CH ₃ OH	5 ₃ → 4 ₃ , E
241879.025	CH ₃ OH	5 ₁ → 4 ₁ , E	5.6	2.1	0.25	0.53 ± 0.03
241887.674	CH ₃ OH	5 ₂ → 4 ₂ , A+	5.6	2.1	0.05	0.10 ± 0.03
241904.147	CH ₃ OH	5 ₋₂ → 4 ₋₂ , E	...	2.4	0.42	1.04 ± 0.03
241904.643	CH ₃ OH	5 ₂ → 4 ₂ , E
242913.610	C ³³ S	J = 5 → 4	5.6	1.8	0.19	0.37 ± 0.02
243915.788	CH ₃ OH	5 ₋₁ → 4 ₋₁ , A-	5.5	2.2	0.31	0.71 ± 0.03
244048.504	H ₂ CS	7 ₁₆ → 6 ₁₅	5.7	2.0	0.20	0.43 ± 0.02
244222.150	c-C ₃ H ₂	3 ₂₁ → 2 ₁₂	5.4	1.5	0.15	0.22 ± 0.02
244254.218	SO ₂	14 _{0,14} → 13 _{1,13}	5.2	1.6	0.13	0.21 ± 0.02
244712.269	H ₂ CCO	12 _{1,11} → 11 _{1,10}	5.8	2.1	0.06	0.14 ± 0.02
244935.557	CS	J = 5 → 4	5.8	2.3	8.75	22.76 ± 0.04
245532.752	D ₂ CO	4 ₁₃ → 3 ₁₂	5.8	1.8	0.06	0.11 ± 0.02
<hr/>						
337061.050	C ¹⁷ O	J = 3 → 2	5.5	1.7	2.64	5.19 ± 0.04
337396.459	C ³⁴ S	J = 7 → 6	5.8	1.8	0.18	0.33 ± 0.02
338072.030	U	2.2	0.06	0.13 ± 0.02
338083.195	H ₂ CS	10 _{1,10} → 9 _{1,9}	5.9	1.7	0.09	0.16 ± 0.02
338124.488	CH ₃ OH	7 ₀ → 6 ₀ , E	5.7	1.7	0.15	0.28 ± 0.02
338344.588	CH ₃ OH	7 ₋₁ → 6 ₋₁ , E	5.7	1.8	0.43	0.83 ± 0.03
338408.698	CH ₃ OH	7 ₀ → 6 ₀ , A+	5.7	1.8	0.48	0.92 ± 0.03
338614.936	CH ₃ OH	7 ₁ → 6 ₁ , E	5.7	2.3	0.09	0.22 ± 0.03
338721.693	CH ₃ OH	7 ₂ → 6 ₂ , E	5.7	1.9	0.17	0.35 ± 0.02
339341.459	SO	3 ₃ → 3 ₂	5.8	1.5	0.10	0.18 ± 0.02
339475.904	CN	N = 3 → 2, J = 5/2 → 5/2, F = 5/2 → 5/2	5.7	1.7	0.09	0.17 ± 0.02
339516.635	CN	N = 3 → 2, J = 5/2 → 5/2, F = 7/2 → 7/2	5.7	1.5	0.15	0.24 ± 0.02
340008.126	CN	N = 3 → 2, J = 5/2 → 3/2, F = 5/2 → 5/2	5.7	1.7	0.20	0.34 ± 0.02
340019.626	CN	N = 3 → 2, J = 5/2 → 3/2, F = 3/2 → 3/2	5.8	1.9	0.19	0.36 ± 0.02
340031.549	CN	N = 3 → 2, J = 5/2 → 3/2, F = 7/2 → 5/2	5.7	2.2	1.19	5.33 ± 0.04
340035.408	CN	N = 3 → 2, J = 5/2 → 3/2, F = 5/2 → 3/2
340035.408	CN	N = 3 → 2, J = 5/2 → 3/2, F = 3/2 → 1/2
340247.770	CN	N = 3 → 2, J = 7/2 → 5/2, F = 7/2 → 5/2	5.7	2.6	2.52	7.36 ± 0.04
340247.770	CN	N = 3 → 2, J = 7/2 → 5/2, F = 9/2 → 7/2
340248.544	CN	N = 3 → 2, J = 7/2 → 5/2, F = 5/2 → 3/2
340261.773	CN	N = 3 → 2, J = 7/2 → 5/2, F = 5/2 → 5/2	5.8	1.8	0.19	0.33 ± 0.02
340264.949	CN	N = 3 → 2, J = 7/2 → 5/2, F = 7/2 → 7/2	5.6	1.4	0.22	0.33 ± 0.02
340630.692	HC ¹⁸ O ⁺	J = 4 → 3	5.8	1.8	0.13	0.24 ± 0.02
340714.155	SO	7 ₈ → 6 ₇	5.8	1.9	0.60	1.34 ± 0.03
<hr/>						
362045.753	DCN	J = 5 → 4	6.0	1.3	0.27	0.34 ± 0.05
362630.303	HNC	J = 4 → 3	5.9	1.7	5.18	9.63 ± 0.09
362736.048	H ₂ CO	5 ₀₅ → 4 ₀₄	6.0	1.8	3.47	6.77 ± 0.09
363739.868	CH ₃ OH	7 ₂ → 6 ₁ , E	5.7	2.0	0.19	0.43 ± 0.07
363945.894	H ₂ CO	5 ₂₄ → 4 ₂₃	5.9	1.8	0.75	1.37 ± 0.07
364275.141	H ₂ CO	5 ₃₃ → 4 ₃₂	5.9	2.0	0.31	0.70 ± 0.07
364288.884	H ₂ CO	5 ₃₂ → 4 ₃₁	5.7	1.8	0.29	0.51 ± 0.07
365363.428	H ₂ CO	5 ₂₃ → 4 ₂₂	5.8	2.4	0.49	1.33 ± 0.10

Notes. ^(a) Rest frequency. For the unidentified lines, this is calculated assuming a source velocity of 5.7 km s⁻¹.

Table B.2. Observed line strengths towards CrA-46.

Frequency [MHz]	Molecule	Transition	v_{LSR} [km s ⁻¹]	Δv [km s ⁻¹]	T_{mb} [K]	$\int T_{\text{mb}} dv$ [K km s ⁻¹]
No detections						

Table B.3. Observed line strengths towards CrA-3.

Frequency [MHz]	Molecule	Transition	v_{LSR} [km s ⁻¹]	Δv [km s ⁻¹]	T_{mb} [K]	$\int T_{\text{mb}} dv$ [K km s ⁻¹]
219560.354	C ¹⁸ O	$J = 2 \rightarrow 1$	6.0	1.1	0.63	0.69 ± 0.03
337061.050	C ¹⁷ O	$J = 3 \rightarrow 2$	5.8	0.3	0.26	0.06 ± 0.03

Table B.4. Observed line strengths towards CrA-5.

Frequency [MHz]	Molecule	Transition	v_{LSR} [km s ⁻¹]	Δv [km s ⁻¹]	T_{mb} [K]	$\int T_{\text{mb}} dv$ [K km s ⁻¹]
219560.354	C ¹⁸ O	$J = 2 \rightarrow 1$	6.2	0.7	1.96	1.40 ± 0.02

Table B.5. Observed line strengths towards LS-RCrA1.

Frequency [MHz]	Molecule	Transition	v_{LSR} [km s ⁻¹]	Δv [km s ⁻¹]	T_{mb} [K]	$\int T_{\text{mb}} dv$ [K km s ⁻¹]
219560.354	C ¹⁸ O	$J = 2 \rightarrow 1$	6.0	1.4	0.86	1.22 ± 0.04

Table B.6. Observed line strengths towards Haas4.

Frequency [MHz]	Molecule	Transition	v_{LSR} [km s ⁻¹]	Δv [km s ⁻¹]	T_{mb} [K]	$\int T_{\text{mb}} dv$ [K km s ⁻¹]
216112.582	DCO ⁺	$J = 3 \rightarrow 2$	5.6	0.9	0.61	0.55 ± 0.02
216278.756	<i>c</i> -C ₃ H ₂	$3_{03} \rightarrow 2_{21}$	5.4	0.5	0.24	0.11 ± 0.02
217104.919	SiO	$J = 5 \rightarrow 4$	10.4	5.6	0.15	1.08 ± 0.06
217822.148	<i>c</i> -C ₃ H ₂	$6_{06} \rightarrow 5_{15}$	5.4	0.6	0.12	0.07 ± 0.02
217822.148	<i>c</i> -C ₃ H ₂	$6_{16} \rightarrow 5_{05}$
217940.046	<i>c</i> -C ₃ H ₂	$5_{14} \rightarrow 4_{23}$	5.7	0.9	0.11	0.12 ± 0.03
218222.192	H ₂ CO	$3_{03} \rightarrow 2_{02}$	5.5	1.0	1.18	1.84 ± 0.05
219560.354	C ¹⁸ O	$J = 2 \rightarrow 1$	5.5	1.3	9.79	14.62 ± 0.04
219949.442	SO	$6_5 \rightarrow 5_4$	5.5	0.9	1.15	2.30 ± 0.06
337061.050	C ¹⁷ O	$J = 3 \rightarrow 2$	5.4	1.3	0.84	1.20 ± 0.04
340247.770	CN	$N = 3 \rightarrow 2, J = 7/2 \rightarrow 5/2, F = 7/2 \rightarrow 5/2$	5.4	0.6	0.20	0.12 ± 0.02
340247.770	CN	$N = 3 \rightarrow 2, J = 7/2 \rightarrow 5/2, F = 9/2 \rightarrow 7/2$

Table B.7. Observed line strengths towards IRS2.

Frequency [MHz]	Molecule	Transition	v_{LSR} [km s ⁻¹]	Δv [km s ⁻¹]	T_{mb} [K]	$\int T_{\text{mb}} dv$ [K km s ⁻¹]
216112.582	DCO ⁺	$J = 3 \rightarrow 2$	6.0	0.4	0.87	0.37 ± 0.01
218222.192	H ₂ CO	$3_{03} \rightarrow 2_{02}$	6.0	0.6	1.97	1.29 ± 0.01
218440.063	CH ₃ OH	$4_2 \rightarrow 3_{1, E}$	6.0	0.4	0.16	0.06 ± 0.01
218475.632	H ₂ CO	$3_{22} \rightarrow 2_{21}$	6.0	0.6	0.07	0.05 ± 0.01
218760.066	H ₂ CO	$3_{21} \rightarrow 2_{20}$	6.2	0.9	0.07	0.07 ± 0.01
219560.354	C ¹⁸ O	$J = 2 \rightarrow 1$	6.2	1.0	7.72	8.47 ± 0.02
219908.525	H ₂ ¹³ CO	$3_{12} \rightarrow 2_{11}$	6.0	0.5	0.07	0.04 ± 0.01
219949.442	S ¹⁸ O	$6_5 \rightarrow 5_4$	6.0	0.4	2.47	1.22 ± 0.01
337061.050	C ¹⁷ O	$J = 3 \rightarrow 2$	6.1	1.0	0.97	1.11 ± 0.02
339341.459	SO	$3_3 \rightarrow 3_2$	6.1	0.4	0.19	0.08 ± 0.01
340247.770	CN	$N = 3 \rightarrow 2, J = 7/2 \rightarrow 5/2, F = 7/2 \rightarrow 5/2$	6.1	1.9	0.09	0.15 ± 0.02
340247.770	CN	$N = 3 \rightarrow 2, J = 7/2 \rightarrow 5/2, F = 9/2 \rightarrow 7/2$

Table B.8. Observed line strengths towards IRS5A.

Frequency [MHz]	Molecule	Transition	v_{LSR} [km s ⁻¹]	Δv [km s ⁻¹]	T_{mb} [K]	$\int T_{\text{mb}} dv$ [K km s ⁻¹]
216112.582	DCO ⁺	$J = 3 \rightarrow 2$	5.7	0.7	0.99	0.81 ± 0.02
216278.756	<i>c</i> -C ₃ H ₂	$3_{03} \rightarrow 2_{21}$	5.6	0.9	0.38	0.39 ± 0.02
216373.320	C ₂ D	$N = 3 \rightarrow 2, J = 7/2 \rightarrow 5/2, F = 5/2 \rightarrow 3/2$	5.9	1.5	0.16	0.26 ± 0.02
216373.320	C ₂ D	$N = 3 \rightarrow 2, J = 7/2 \rightarrow 5/2, F = 7/2 \rightarrow 5/2$
216428.320	C ₂ D	$N = 3 \rightarrow 2, J = 5/2 \rightarrow 3/2, F = 7/2 \rightarrow 5/2$	5.5	1.0	0.12	0.12 ± 0.01
216428.320	C ₂ D	$N = 3 \rightarrow 2, J = 5/2 \rightarrow 3/2, F = 5/2 \rightarrow 3/2$
217238.538	DCN	$J = 3 \rightarrow 2$	5.6	1.0	0.18	0.20 ± 0.02
217467.150	¹³ CN	$N = 2 \rightarrow 1, J = 5/2 \rightarrow 3/2, F_1 = 3 \rightarrow 2, F = 4 \rightarrow 3$	5.4	0.8	0.11	0.09 ± 0.01
217467.150	¹³ CN	$N = 2 \rightarrow 1, J = 5/2 \rightarrow 3/2, F_1 = 3 \rightarrow 2, F = 3 \rightarrow 2$
217822.148	<i>c</i> -C ₃ H ₂	$6_{06} \rightarrow 5_{15}$	5.6	1.0	0.34	0.37 ± 0.02
217822.148	<i>c</i> -C ₃ H ₂	$6_{16} \rightarrow 5_{05}$
217940.046	<i>c</i> -C ₃ H ₂	$5_{14} \rightarrow 4_{23}$	5.6	1.0	0.20	0.21 ± 0.02
218222.192	H ₂ CO	$3_{03} \rightarrow 2_{02}$	5.6	1.3	3.26	4.87 ± 0.03
218440.063	CH ₃ OH	$4_2 \rightarrow 3_1, E$	5.6	1.1	0.20	0.26 ± 0.02
218475.632	H ₂ CO	$3_{22} \rightarrow 2_{21}$	5.5	1.4	0.37	0.58 ± 0.02
218760.066	H ₂ CO	$3_{21} \rightarrow 2_{20}$	5.5	1.4	0.38	0.54 ± 0.02
219560.354	C ¹⁸ O	$J = 2 \rightarrow 1$	5.7	1.1	12.72	16.13 ± 0.03
219908.525	H ₂ ¹³ CO	$3_{12} \rightarrow 2_{11}$	5.6	1.3	0.09	0.13 ± 0.02
219949.442	S ¹⁸ O	$6_5 \rightarrow 5_4$	5.7	0.7	6.05	4.80 ± 0.02
337061.050	C ¹⁷ O	$J = 3 \rightarrow 2$	5.6	1.2	2.03	2.65 ± 0.03
338344.588	CH ₃ OH	$7_{-1} \rightarrow 6_{-1}, E$	5.5	1.6	0.10	0.16 ± 0.03
338408.698	CH ₃ OH	$7_0 \rightarrow 6_0, A+$	5.4	1.6	0.14	0.23 ± 0.03
339341.459	SO	$3_3 \rightarrow 3_2$	5.7	0.5	0.73	0.40 ± 0.02
340008.126	CN	$N = 3 \rightarrow 2, J = 5/2 \rightarrow 3/2, F = 5/2 \rightarrow 5/2$	5.4	1.5	0.14	0.23 ± 0.03
340019.626	CN	$N = 3 \rightarrow 2, J = 5/2 \rightarrow 3/2, F = 3/2 \rightarrow 3/2$	5.6	1.1	0.15	0.21 ± 0.03
340031.549	CN	$N = 3 \rightarrow 2, J = 5/2 \rightarrow 3/2, F = 7/2 \rightarrow 5/2$	5.4	1.7	0.69	1.17 ± 0.03
340035.408	CN	$N = 3 \rightarrow 2, J = 5/2 \rightarrow 3/2, F = 3/2 \rightarrow 1/2$	5.4	1.6	0.69	1.11 ± 0.03
340035.408	CN	$N = 3 \rightarrow 2, J = 5/2 \rightarrow 3/2, F = 5/2 \rightarrow 3/2$
340247.770	CN	$N = 3 \rightarrow 2, J = 7/2 \rightarrow 5/2, F = 7/2 \rightarrow 5/2$	5.3	2.2	1.42	3.36 ± 0.04
340247.770	CN	$N = 3 \rightarrow 2, J = 7/2 \rightarrow 5/2, F = 9/2 \rightarrow 7/2$
340261.773	CN	$N = 3 \rightarrow 2, J = 7/2 \rightarrow 5/2, F = 5/2 \rightarrow 5/2$	5.7	2.5	0.10	0.16 ± 0.02
340264.949	CN	$N = 3 \rightarrow 2, J = 7/2 \rightarrow 5/2, F = 7/2 \rightarrow 7/2$	5.5	1.2	0.20	0.23 ± 0.03
340630.692	HC ¹⁸ O ⁺	$J = 4 \rightarrow 3$	5.5	0.6	0.13	0.07 ± 0.02
340714.155	SO	$7_8 \rightarrow 6_7$	5.5	0.5	0.52	0.27 ± 0.02
362630.303	HNC	$J = 4 \rightarrow 3$	5.6	1.5	1.59	2.41 ± 0.06
362736.048	H ₂ CO	$5_{05} \rightarrow 4_{04}$	5.6	1.2	0.74	0.93 ± 0.05

Table B.9. Observed line strengths towards IRS5N.

Frequency [MHz]	Molecule	Transition	v_{LSR} [km s ⁻¹]	Δv [km s ⁻¹]	T_{mb} [K]	$\int T_{\text{mb}} dv$ [K km s ⁻¹]
216112.582	DCO ⁺	$J = 3 \rightarrow 2$	5.7	0.9	0.80	0.78 ± 0.02
216278.756	<i>c</i> -C ₃ H ₂	$3_{03} \rightarrow 2_{21}$	5.7	1.3	0.26	0.35 ± 0.02
216373.320	C ₂ D	$N = 3 \rightarrow 2, J = 7/2 \rightarrow 5/2, F = 5/2 \rightarrow 3/2$	5.9	1.6	0.17	0.29 ± 0.02
216373.320	C ₂ D	$N = 3 \rightarrow 2, J = 7/2 \rightarrow 5/2, F = 7/2 \rightarrow 5/2$
216428.320	C ₂ D	$N = 3 \rightarrow 2, J = 5/2 \rightarrow 3/2, F = 7/2 \rightarrow 5/2$	5.5	1.6	0.10	0.15 ± 0.02
216428.320	C ₂ D	$N = 3 \rightarrow 2, J = 5/2 \rightarrow 3/2, F = 5/2 \rightarrow 3/2$
217238.538	DCN	$J = 3 \rightarrow 2$	5.8	1.5	0.17	0.26 ± 0.02
217467.150	¹³ CN	$N = 2 \rightarrow 1, J = 5/2 \rightarrow 3/2, F_1 = 3 \rightarrow 2, F = 4 \rightarrow 3$	5.6	1.6	0.08	0.12 ± 0.02
217467.150	¹³ CN	$N = 2 \rightarrow 1, J = 5/2 \rightarrow 3/2, F_1 = 3 \rightarrow 2, F = 3 \rightarrow 2$
217822.148	<i>c</i> -C ₃ H ₂	$6_{06} \rightarrow 5_{15}$	5.6	1.2	0.27	0.36 ± 0.02
217822.148	<i>c</i> -C ₃ H ₂	$6_{16} \rightarrow 5_{05}$
217940.046	<i>c</i> -C ₃ H ₂	$5_{14} \rightarrow 4_{23}$	5.7	1.4	0.16	0.23 ± 0.02
218160.456	<i>c</i> -C ₃ H ₂	$5_{24} \rightarrow 4_{13}$	5.7	1.1	0.07	0.09 ± 0.02
218222.192	H ₂ CO	$3_{03} \rightarrow 2_{02}$	5.7	1.4	3.26	4.95 ± 0.03
218440.063	CH ₃ OH	$4_2 \rightarrow 3_{1, E}$	5.7	1.2	0.23	0.30 ± 0.02
218475.632	H ₂ CO	$3_{22} \rightarrow 2_{21}$	5.6	1.4	0.35	0.50 ± 0.02
218760.066	H ₂ CO	$3_{21} \rightarrow 2_{20}$	5.6	1.3	0.37	0.54 ± 0.02
219560.354	C ¹⁸ O	$J = 2 \rightarrow 1$	5.7	1.1	12.39	15.71 ± 0.03
219908.525	H ¹³ CO	$3_{12} \rightarrow 2_{11}$	5.8	1.1	0.12	0.14 ± 0.02
219934.040	C ¹⁵ N	$N = 2 \rightarrow 1, J = 5/2 \rightarrow 3/2, F = 2 \rightarrow 1$	4.3	2.7	0.04	0.11 ± 0.03
219934.820	C ¹⁵ N	$N = 2 \rightarrow 1, J = 5/2 \rightarrow 3/2, F = 3 \rightarrow 2$
219949.442	SO	$6_5 \rightarrow 5_4$	5.7	0.7	3.77	3.00 ± 0.02
337061.050	C ¹⁷ O	$J = 3 \rightarrow 2$	5.7	1.2	1.94	2.53 ± 0.03
338344.588	CH ₃ OH	$7_{-1} \rightarrow 6_{-1, E}$	5.5	1.2	0.15	0.18 ± 0.02
338408.698	CH ₃ OH	$7_0 \rightarrow 6_0, A+$	5.6	1.4	0.16	0.25 ± 0.03
339341.459	SO	$3_3 \rightarrow 3_2$	5.7	0.5	0.29	0.15 ± 0.02
339516.635	CN	$N = 3 \rightarrow 2, J = 5/2 \rightarrow 5/2, F = 7/2 \rightarrow 7/2$	5.4	1.1	0.10	0.14 ± 0.02
340008.126	CN	$N = 3 \rightarrow 2, J = 5/2 \rightarrow 3/2, F = 5/2 \rightarrow 5/2$	5.4	0.9	0.15	0.18 ± 0.02
340019.626	CN	$N = 3 \rightarrow 2, J = 5/2 \rightarrow 3/2, F = 3/2 \rightarrow 3/2$	5.6	1.5	0.13	0.20 ± 0.02
340031.549	CN	$N = 3 \rightarrow 2, J = 5/2 \rightarrow 3/2, F = 7/2 \rightarrow 5/2$	5.6	1.8	0.72	1.15 ± 0.02
340035.408	CN	$N = 3 \rightarrow 2, J = 5/2 \rightarrow 3/2, F = 3/2 \rightarrow 1/2$	5.6	1.5	0.69	1.03 ± 0.02
340035.408	CN	$N = 3 \rightarrow 2, J = 5/2 \rightarrow 3/2, F = 5/2 \rightarrow 3/2$
340247.770	CN	$N = 3 \rightarrow 2, J = 7/2 \rightarrow 5/2, F = 7/2 \rightarrow 5/2$	5.4	2.1	1.44	3.15 ± 0.03
340247.770	CN	$N = 3 \rightarrow 2, J = 7/2 \rightarrow 5/2, F = 9/2 \rightarrow 7/2$
340261.773	CN	$N = 3 \rightarrow 2, J = 7/2 \rightarrow 5/2, F = 5/2 \rightarrow 5/2$	5.5	1.0	0.13	0.12 ± 0.02
340264.949	CN	$N = 3 \rightarrow 2, J = 7/2 \rightarrow 5/2, F = 7/2 \rightarrow 7/2$	5.6	1.2	0.16	0.19 ± 0.02
340714.155	SO	$7_8 \rightarrow 6_7$	5.5	0.6	0.17	0.12 ± 0.02
362150.763	U	0.7	0.24	0.15 ± 0.04
362630.303	HNC	$J = 4 \rightarrow 3$	5.9	1.5	1.83	2.75 ± 0.07
362736.048	H ₂ CO	$5_{05} \rightarrow 4_{04}$	5.7	1.2	0.77	0.90 ± 0.06

Table B.10. Observed line strengths towards IRS1.

Frequency [MHz]	Molecule	Transition	v_{LSR} [km s ⁻¹]	Δv [km s ⁻¹]	T_{mb} [K]	$\int T_{\text{mb}} dv$ [K km s ⁻¹]
216112.582	DCO ⁺	$J = 3 \rightarrow 2$	5.8	0.8	0.44	0.38 ± 0.02
216278.756	<i>c</i> -C ₃ H ₂	$3_{03} \rightarrow 2_{21}$	5.8	0.8	0.15	0.13 ± 0.02
216373.320	C ₂ D	$N = 3 \rightarrow 2, J = 7/2 \rightarrow 5/2, F = 5/2 \rightarrow 3/2$	6.0	1.2	0.10	0.13 ± 0.02
216373.320	C ₂ D	$N = 3 \rightarrow 2, J = 7/2 \rightarrow 5/2, F = 7/2 \rightarrow 5/2$
216428.320	C ₂ D	$N = 3 \rightarrow 2, J = 5/2 \rightarrow 3/2, F = 7/2 \rightarrow 5/2$	5.8	0.8	0.09	0.06 ± 0.02
216428.320	C ₂ D	$N = 3 \rightarrow 2, J = 5/2 \rightarrow 3/2, F = 5/2 \rightarrow 3/2$
217238.538	DCN	$J = 3 \rightarrow 2$	5.8	0.9	0.17	0.17 ± 0.02
217467.150	¹³ CN	$N = 2 \rightarrow 1, J = 5/2 \rightarrow 3/2, F_1 = 3 \rightarrow 2, F = 4 \rightarrow 3$	5.7	2.5	0.05	0.15 ± 0.03
217467.150	¹³ CN	$N = 2 \rightarrow 1, J = 5/2 \rightarrow 3/2, F_1 = 3 \rightarrow 2, F = 3 \rightarrow 2$
217822.148	<i>c</i> -C ₃ H ₂	$6_{06} \rightarrow 5_{15}$	5.8	0.8	0.13	0.10 ± 0.02
217822.148	<i>c</i> -C ₃ H ₂	$6_{16} \rightarrow 5_{05}$
217940.046	<i>c</i> -C ₃ H ₂	$5_{14} \rightarrow 4_{23}$	5.6	0.6	0.09	0.05 ± 0.02
218222.192	H ₂ CO	$3_{03} \rightarrow 2_{02}$	5.8	1.2	3.05	4.08 ± 0.03
218440.063	CH ₃ OH	$4_2 \rightarrow 3_1, E$	5.9	1.2	0.30	0.39 ± 0.02
218475.632	H ₂ CO	$3_{22} \rightarrow 2_{21}$	5.8	1.4	0.33	0.54 ± 0.02
218760.066	H ₂ CO	$3_{21} \rightarrow 2_{20}$	5.8	1.3	0.35	0.39 ± 0.02
219560.354	C ¹⁸ O	$J = 2 \rightarrow 1$	5.8	1.1	11.61	13.63 ± 0.03
219908.525	H ₂ ¹³ CO	$3_{12} \rightarrow 2_{11}$	5.9	0.9	0.09	0.09 ± 0.02
219949.442	S ³⁴ O	$6_5 \rightarrow 5_4$	5.8	1.0	2.20	2.47 ± 0.03
337061.050	C ¹⁷ O	$J = 3 \rightarrow 2$	5.8	1.1	1.70	1.97 ± 0.03
338344.588	CH ₃ OH	$7_{-1} \rightarrow 6_{-1}, E$	5.8	1.1	0.24	0.26 ± 0.03
338408.698	CH ₃ OH	$7_0 \rightarrow 6_0, A+$	5.8	1.4	0.24	0.36 ± 0.03
340031.549	CN	$N = 3 \rightarrow 2, J = 5/2 \rightarrow 3/2, F = 7/2 \rightarrow 5/2$	5.9	1.0	0.49	0.52 ± 0.03
340035.408	CN	$N = 3 \rightarrow 2, J = 5/2 \rightarrow 3/2, F = 3/2 \rightarrow 1/2$	5.8	1.0	0.47	0.48 ± 0.03
340035.408	CN	$N = 3 \rightarrow 2, J = 5/2 \rightarrow 3/2, F = 5/2 \rightarrow 3/2$
340247.770	CN	$N = 3 \rightarrow 2, J = 7/2 \rightarrow 5/2, F = 7/2 \rightarrow 5/2$	5.7	1.6	0.87	1.48 ± 0.04
340247.770	CN	$N = 3 \rightarrow 2, J = 7/2 \rightarrow 5/2, F = 9/2 \rightarrow 7/2$
340261.773	CN	$N = 3 \rightarrow 2, J = 7/2 \rightarrow 5/2, F = 5/2 \rightarrow 5/2$	5.8	0.8	0.11	0.09 ± 0.02
340264.949	CN	$N = 3 \rightarrow 2, J = 7/2 \rightarrow 5/2, F = 7/2 \rightarrow 7/2$	5.9	0.8	0.13	0.10 ± 0.02
340714.155	SO	$7_8 \rightarrow 6_7$	5.6	1.7	0.32	0.60 ± 0.04
362630.303	HNC	$J = 4 \rightarrow 3$	6.0	1.4	0.73	1.02 ± 0.06
362736.048	H ₂ CO	$5_{05} \rightarrow 4_{04}$	6.0	1.7	0.48	0.78 ± 0.06

Table B.11. Observed line strengths towards IRS7A.

Frequency [MHz]	Molecule	Transition	v_{LSR} [km s ⁻¹]	Δv [km s ⁻¹]	T_{mb} [K]	$\int T_{\text{mb}} dv$ [K km s ⁻¹]
337061.050	C ¹⁷ O	$J = 3 \rightarrow 2$	5.1	2.0	2.39	5.63 ± 0.04
337396.459	C ³⁴ S	$J = 7 \rightarrow 6$	5.0	2.4	0.21	0.54 ± 0.03
337580.147	³⁴ SO	$8_8 \rightarrow 7_7$	4.6	3.8	0.07	0.34 ± 0.04
338083.195	H ₂ CS	$10_{1,10} \rightarrow 9_{1,9}$	5.2	1.4	0.08	0.11 ± 0.02
338124.488	CH ₃ OH	$7_0 \rightarrow 6_0, \text{E}$	5.0	2.2	0.12	0.24 ± 0.02
338344.588	CH ₃ OH	$7_{-1} \rightarrow 6_{-1}, \text{E}$	5.1	2.4	0.36	0.87 ± 0.03
338408.698	CH ₃ OH	$7_0 \rightarrow 6_0, \text{A}+$	5.1	2.3	0.45	1.09 ± 0.03
338614.936	CH ₃ OH	$7_1 \rightarrow 6_1, \text{E}$	5.2	2.2	0.10	0.19 ± 0.03
338721.693	CH ₃ OH	$7_2 \rightarrow 6_2, \text{E}$	4.9	2.8	0.17	0.40 ± 0.03
339341.459	SO	$3_3 \rightarrow 3_2$	4.9	2.6	0.19	0.52 ± 0.03
339516.635	CN	$N = 3 \rightarrow 2, J = 5/2 \rightarrow 5/2, F = 7/2 \rightarrow 7/2$	5.1	1.3	0.12	0.15 ± 0.02
339857.269	³⁴ SO	$9_8 \rightarrow 8_7$	4.6	2.8	0.14	0.42 ± 0.03
340008.126	CN	$N = 3 \rightarrow 2, J = 5/2 \rightarrow 3/2, F = 5/2 \rightarrow 5/2$	5.1	2.3	0.16	0.39 ± 0.03
340019.626	CN	$N = 3 \rightarrow 2, J = 5/2 \rightarrow 3/2, F = 3/2 \rightarrow 3/2$	5.1	2.0	0.17	0.39 ± 0.03
340031.549	CN	$N = 3 \rightarrow 2, J = 5/2 \rightarrow 3/2, F = 7/2 \rightarrow 5/2$	5.1	2.4	1.13	5.67 ± 0.05
340035.408	CN	$N = 3 \rightarrow 2, J = 5/2 \rightarrow 3/2, F = 5/2 \rightarrow 3/2$
340035.408	CN	$N = 3 \rightarrow 2, J = 5/2 \rightarrow 3/2, F = 3/2 \rightarrow 1/2$
340247.770	CN	$N = 3 \rightarrow 2, J = 7/2 \rightarrow 5/2, F = 7/2 \rightarrow 5/2$	4.9	2.8	2.64	8.14 ± 0.04
340247.770	CN	$N = 3 \rightarrow 2, J = 7/2 \rightarrow 5/2, F = 9/2 \rightarrow 7/2$
340261.773	CN	$N = 3 \rightarrow 2, J = 7/2 \rightarrow 5/2, F = 5/2 \rightarrow 5/2$	5.3	1.9	0.14	0.31 ± 0.02
340264.949	CN	$N = 3 \rightarrow 2, J = 7/2 \rightarrow 5/2, F = 7/2 \rightarrow 7/2$	5.0	2.0	0.16	0.36 ± 0.03
340630.692	HC ¹⁸ O ⁺	$J = 4 \rightarrow 3$	5.1	1.3	0.19	0.29 ± 0.03
340714.155	SO	$7_8 \rightarrow 6_7$	4.7	3.0	1.18	3.66 ± 0.04
362045.753	DCN	$J = 5 \rightarrow 4$	5.8	2.6	0.19	0.53 ± 0.08
362630.303	HNC	$J = 4 \rightarrow 3$	5.5	2.3	3.13	7.57 ± 0.09
362736.048	H ₂ CO	$5_{05} \rightarrow 4_{04}$	5.4	2.5	2.30	6.39 ± 0.10
363945.894	H ₂ CO	$5_{24} \rightarrow 4_{23}$	5.4	2.4	0.54	1.35 ± 0.08
364275.141	H ₂ CO	$5_{33} \rightarrow 4_{32}$	5.3	2.5	0.21	0.61 ± 0.10
364288.884	H ₂ CO	$5_{32} \rightarrow 4_{31}$	5.6	2.7	0.20	0.59 ± 0.10

Table B.12. Observed line strengths towards CrA-24, total flux (both source and outflow components).

Frequency [MHz]	Molecule	Transition	v_{LSR} [km s ⁻¹]	Δv [km s ⁻¹]	T_{mb} [K]	$\int T_{\text{mb}} dv$ [K km s ⁻¹]
216112.582	DCO ⁺	$J = 3 \rightarrow 2$	4.9	1.2	0.26	0.31 ± 0.03
216278.756	<i>c</i> -C ₃ H ₂	$3_{03} \rightarrow 2_{21}$	4.8	0.9	0.27	0.24 ± 0.02
216373.320	C ₂ D	$N = 3 \rightarrow 2, J = 7/2 \rightarrow 5/2, F = 5/2 \rightarrow 3/2$	5.2	1.5	0.10	0.19 ± 0.04
216373.320	C ₂ D	$N = 3 \rightarrow 2, J = 7/2 \rightarrow 5/2, F = 7/2 \rightarrow 5/2$
217104.919	SiO	$J = 5 \rightarrow 4$	1.9	4.5	0.10	0.49 ± 0.05
217238.538	DCN	$J = 3 \rightarrow 2$	4.7	1.1	0.24	0.27 ± 0.03
217822.148	<i>c</i> -C ₃ H ₂	$6_{06} \rightarrow 5_{15}$	4.8	1.3	0.27	0.37 ± 0.04
217822.148	<i>c</i> -C ₃ H ₂	$6_{16} \rightarrow 5_{05}$
217940.046	<i>c</i> -C ₃ H ₂	$5_{14} \rightarrow 4_{23}$	5.0	1.0	0.16	0.19 ± 0.04
218222.192	H ₂ CO	$3_{03} \rightarrow 2_{02}$	7.99 ± 0.07
218440.063	CH ₃ OH	$4_2 \rightarrow 3_{1, E}$	4.8	2.2	0.17	0.47 ± 0.06
218475.632	H ₂ CO	$3_{22} \rightarrow 2_{21}$	1.47 ± 0.06
218760.066	H ₂ CO	$3_{21} \rightarrow 2_{20}$	1.63 ± 0.06
219560.354	C ¹⁸ O	$J = 2 \rightarrow 1$	5.1	1.5	9.45	17.30 ± 0.07
219908.525	H ₂ ¹³ CO	$3_{12} \rightarrow 2_{11}$	4.6	1.6	0.10	0.16 ± 0.04
219949.442	S ¹⁸ O	$6_5 \rightarrow 5_4$	2.40 ± 0.06
337061.050	C ¹⁷ O	$J = 3 \rightarrow 2$	4.9	1.7	1.60	3.11 ± 0.05
338344.588	CH ₃ OH	$7_{-1} \rightarrow 6_{-1, E}$	0.60 ± 0.04
338408.698	CH ₃ OH	$7_0 \rightarrow 6_0, A+$	0.73 ± 0.03
340008.126	CN	$N = 3 \rightarrow 2, J = 5/2 \rightarrow 3/2, F = 5/2 \rightarrow 5/2$	4.6	1.1	0.11	0.13 ± 0.03
340031.549	CN	$N = 3 \rightarrow 2, J = 5/2 \rightarrow 3/2, F = 7/2 \rightarrow 5/2$	4.7	1.7	0.43	0.76 ± 0.04
340035.408	CN	$N = 3 \rightarrow 2, J = 5/2 \rightarrow 3/2, F = 3/2 \rightarrow 1/2$	4.7	1.9	0.40	0.77 ± 0.04
340035.408	CN	$N = 3 \rightarrow 2, J = 5/2 \rightarrow 3/2, F = 5/2 \rightarrow 3/2$
340247.770	CN	$N = 3 \rightarrow 2, J = 7/2 \rightarrow 5/2, F = 7/2 \rightarrow 5/2$	4.6	1.7	1.12	2.49 ± 0.06
340247.770	CN	$N = 3 \rightarrow 2, J = 7/2 \rightarrow 5/2, F = 9/2 \rightarrow 7/2$
340714.155	SO	$7_8 \rightarrow 6_7$	5.0	1.7	0.12	0.28 ± 0.05
362630.303	HNC	$J = 4 \rightarrow 3$	4.6	1.3	1.98	2.67 ± 0.07
362736.048	H ₂ CO	$5_{05} \rightarrow 4_{04}$	2.43 ± 0.09
363945.894	H ₂ CO	$5_{24} \rightarrow 4_{23}$	4.7	1.3	0.25	0.32 ± 0.07

Table B.13. Observed line strengths towards CrA-24, on-source velocity component. The integrated intensities are calculated from Gaussian fits.

Frequency [MHz]	Molecule	Transition	v_{LSR} [km s ⁻¹]	Δv [km s ⁻¹]	T_{mb} [K]	$\int T_{\text{mb}} dv$ [K km s ⁻¹]
217104.919	SiO	$J = 5 \rightarrow 4$	4.6	2.4	0.06	0.17 ± 0.03
218222.192	H ₂ CO	$3_{03} \rightarrow 2_{02}$	5.0	1.8	2.61	5.09 ± 0.03
218440.063	CH ₃ OH	$4_2 \rightarrow 3_{1, E}$	5.1	1.5	0.17	0.27 ± 0.03
218475.632	H ₂ CO	$3_{22} \rightarrow 2_{21}$	5.0	1.9	0.42	0.84 ± 0.03
218760.066	H ₂ CO	$3_{21} \rightarrow 2_{20}$	4.9	1.9	0.46	0.92 ± 0.03
219908.525	H ₂ ¹³ CO	$3_{12} \rightarrow 2_{11}$	4.6	1.6	0.10	0.16 ± 0.03
219949.442	S ¹⁸ O	$6_5 \rightarrow 5_4$	5.1	1.7	0.87	1.58 ± 0.03
338344.588	CH ₃ OH	$7_{-1} \rightarrow 6_{-1, E}$	5.1	2.0	0.30	0.63 ± 0.03
338408.698	CH ₃ OH	$7_0 \rightarrow 6_0, A+$	4.9	1.7	0.42	0.77 ± 0.03
340247.770	CN	$N = 3 \rightarrow 2, J = 7/2 \rightarrow 5/2, F = 7/2 \rightarrow 5/2$	4.6	1.7	1.13	2.00 ± 0.03
340247.770	CN	$N = 3 \rightarrow 2, J = 7/2 \rightarrow 5/2, F = 9/2 \rightarrow 7/2$
340714.155	SO	$7_8 \rightarrow 6_7$	5.0	1.7	0.12	0.22 ± 0.03
362736.048	H ₂ CO	$5_{05} \rightarrow 4_{04}$	4.9	1.7	1.13	2.07 ± 0.05
363945.894	H ₂ CO	$5_{24} \rightarrow 4_{23}$	4.7	1.2	0.26	0.32 ± 0.04

Table B.14. Observed line strengths towards CrA-24, outflow velocity component. The integrated intensities are calculated from Gaussian fits.

Frequency [MHz]	Molecule	Transition	v_{LSR} [km s ⁻¹]	Δv [km s ⁻¹]	T_{mb} [K]	$\int T_{\text{mb}} dv$ [K km s ⁻¹]
217104.919	SiO	$J = 5 \rightarrow 4$	1.2	2.2	0.13	0.30 ± 0.03
218222.192	H ₂ CO	$3_{03} \rightarrow 2_{02}$	2.0	3.2	0.75	2.57 ± 0.04
218440.063	CH ₃ OH	$4_2 \rightarrow 3_{1, E}$	2.7	3.5	0.06	0.23 ± 0.04
218475.632	H ₂ CO	$3_{22} \rightarrow 2_{21}$	2.2	3.7	0.18	0.71 ± 0.04
218760.066	H ₂ CO	$3_{21} \rightarrow 2_{20}$	1.6	3.7	0.18	0.73 ± 0.04
219908.525	H ₂ ¹³ CO	$3_{12} \rightarrow 2_{11}$	1.3	1.1	0.05	0.06 ± 0.02
219949.442	SO	$6_5 \rightarrow 5_4$	1.9	2.8	0.25	0.74 ± 0.03
338344.588	CH ₃ OH	$7_{-1} \rightarrow 6_{-1, E}$	2.0	2.3	0.13	0.33 ± 0.03
338408.698	CH ₃ OH	$7_0 \rightarrow 6_0, A+$	1.6	2.5	0.14	0.38 ± 0.03
340247.770	CN	$N = 3 \rightarrow 2, J = 7/2 \rightarrow 5/2, F = 7/2 \rightarrow 5/2$	1.6	2.9	0.11	0.34 ± 0.03
340247.770	CN	$N = 3 \rightarrow 2, J = 7/2 \rightarrow 5/2, F = 9/2 \rightarrow 7/2$
340714.155	SO	$7_8 \rightarrow 6_7$	1.1	0.4	0.10	0.04 ± 0.01
362736.048	H ₂ CO	$5_{05} \rightarrow 4_{04}$	1.8	1.4	0.23	0.35 ± 0.04
363945.894	H ₂ CO	$5_{24} \rightarrow 4_{23}$	2.2	1.5	0.11	0.19 ± 0.04

Table B.15. Observed line strengths towards SMM 2, total flux (both source and outflow components).

Frequency [MHz]	Molecule	Transition	v_{LSR} [km s ⁻¹]	Δv [km s ⁻¹]	T_{mb} [K]	$\int T_{\text{mb}} dv$ [K km s ⁻¹]
216112.582	DCO ⁺	$J = 3 \rightarrow 2$	4.8	0.5	0.36	0.21 ± 0.03
216278.756	<i>c</i> -C ₃ H ₂	$3_{03} \rightarrow 2_{21}$	5.0	0.5	0.26	0.14 ± 0.02
216373.320	C ₂ D	$N = 3 \rightarrow 2, J = 7/2 \rightarrow 5/2, F = 5/2 \rightarrow 3/2$	5.4	0.8	0.09	0.08 ± 0.03
216373.320	C ₂ D	$N = 3 \rightarrow 2, J = 7/2 \rightarrow 5/2, F = 7/2 \rightarrow 5/2$
217104.919	SiO	$J = 5 \rightarrow 4$	1.3	6.0	0.14	1.08 ± 0.08
217238.538	DCN	$J = 3 \rightarrow 2$	4.3	2.7	0.13	0.28 ± 0.03
217822.148	<i>c</i> -C ₃ H ₂	$6_{06} \rightarrow 5_{15}$	5.0	1.4	0.19	0.26 ± 0.03
217822.148	<i>c</i> -C ₃ H ₂	$6_{16} \rightarrow 5_{05}$
218222.192	H ₂ CO	$3_{03} \rightarrow 2_{02}$	8.76 ± 0.07
218440.063	CH ₃ OH	$4_2 \rightarrow 3_{1, E}$	2.8	3.9	0.28	1.14 ± 0.05
218475.632	H ₂ CO	$3_{22} \rightarrow 2_{21}$	2.6	3.3	0.49	1.77 ± 0.06
218760.066	H ₂ CO	$3_{21} \rightarrow 2_{20}$	2.6	3.2	0.53	1.86 ± 0.05
219560.354	C ¹⁸ O	$J = 2 \rightarrow 1$	5.3	1.3	9.35	14.74 ± 0.07
219908.525	H ₂ ¹³ CO	$3_{12} \rightarrow 2_{11}$	0.31 ± 0.04
219949.442	SO	$6_5 \rightarrow 5_4$	4.18 ± 0.07
337061.050	C ¹⁷ O	$J = 3 \rightarrow 2$	5.3	1.5	1.34	2.30 ± 0.04
338344.588	CH ₃ OH	$7_{-1} \rightarrow 6_{-1, E}$	1.78 ± 0.07
338408.698	CH ₃ OH	$7_0 \rightarrow 6_0, A+$	1.76 ± 0.06
340019.626	CN	$N = 3 \rightarrow 2, J = 5/2 \rightarrow 3/2, F = 3/2 \rightarrow 3/2$	4.9	0.8	0.09	0.09 ± 0.02
340031.549	CN	$N = 3 \rightarrow 2, J = 5/2 \rightarrow 3/2, F = 7/2 \rightarrow 5/2$	5.0	2.7	0.39	1.96 ± 0.05
340035.408	CN	$N = 3 \rightarrow 2, J = 5/2 \rightarrow 3/2, F = 5/2 \rightarrow 3/2$
340035.408	CN	$N = 3 \rightarrow 2, J = 5/2 \rightarrow 3/2, F = 3/2 \rightarrow 1/2$
340247.770	CN	$N = 3 \rightarrow 2, J = 7/2 \rightarrow 5/2, F = 7/2 \rightarrow 5/2$	4.9	2.1	1.12	3.13 ± 0.04
340247.770	CN	$N = 3 \rightarrow 2, J = 7/2 \rightarrow 5/2, F = 9/2 \rightarrow 7/2$
340261.773	CN	$N = 3 \rightarrow 2, J = 7/2 \rightarrow 5/2, F = 5/2 \rightarrow 5/2$	5.0	1.2	0.09	0.12 ± 0.02
340264.949	CN	$N = 3 \rightarrow 2, J = 7/2 \rightarrow 5/2, F = 7/2 \rightarrow 7/2$	4.8	0.9	0.09	0.11 ± 0.02
340714.155	SO	$7_8 \rightarrow 6_7$	3.0	3.1	0.09	0.25 ± 0.03
362630.303	HNC	$J = 4 \rightarrow 3$	4.8	0.9	1.52	1.43 ± 0.05
362736.048	H ₂ CO	$5_{05} \rightarrow 4_{04}$	1.63 ± 0.10

Table B.16. Observed line strengths towards SMM 2, on-source velocity component. The integrated intensities are calculated from Gaussian fits.

Frequency [MHz]	Molecule	Transition	v_{LSR} [km s ⁻¹]	Δv [km s ⁻¹]	T_{mb} [K]	$\int T_{\text{mb}} dv$ [K km s ⁻¹]
218222.192	H ₂ CO	3 ₀₃ → 2 ₀₂	5.1	1.3	0.87	1.23 ± 0.02
218440.063	CH ₃ OH	4 ₂ → 3 ₁ , E	5.2	0.8	0.11	0.09 ± 0.02
218475.632	H ₂ CO	3 ₂₂ → 2 ₂₁	5.1	1.6	0.08	0.14 ± 0.03
218760.066	H ₂ CO	3 ₂₁ → 2 ₂₀	4.6	1.5	0.16	0.26 ± 0.02
219908.525	H ₂ ¹³ CO	3 ₁₂ → 2 ₁₁	4.6	2.2	0.07	0.16 ± 0.03
219949.442	S ₂ O	6 ₅ → 5 ₄	5.7	0.5	0.23	0.13 ± 0.01
338344.588	CH ₃ OH	7 ₋₁ → 6 ₋₁ , E	6.4	2.5	0.04	0.11 ± 0.02
338408.698	CH ₃ OH	7 ₀ → 6 ₀ , A+	5.2	1.6	0.05	0.09 ± 0.02
362736.048	H ₂ CO	5 ₀₅ → 4 ₀₄	5.3	1.7	0.20	0.35 ± 0.05

Table B.17. Observed line strengths towards SMM 2, outflow velocity component. The integrated intensities are calculated from Gaussian fits.

Frequency [MHz]	Molecule	Transition	v_{LSR} [km s ⁻¹]	Δv [km s ⁻¹]	T_{mb} [K]	$\int T_{\text{mb}} dv$ [K km s ⁻¹]
217104.919	SiO	$J = 5 \rightarrow 4$	1.3	6.6	0.32	1.08 ± 0.08
218222.192	H ₂ CO	3 ₀₃ → 2 ₀₂	2.7	2.9	2.11	6.55 ± 0.03
218440.063	CH ₃ OH	4 ₂ → 3 ₁ , E	2.6	3.3	0.29	1.02 ± 0.04
218475.632	H ₂ CO	3 ₂₂ → 2 ₂₁	2.5	2.8	0.51	1.54 ± 0.03
218760.066	H ₂ CO	3 ₂₁ → 2 ₂₀	2.4	2.4	0.56	1.44 ± 0.03
219908.525	H ₂ ¹³ CO	3 ₁₂ → 2 ₁₁	2.0	1.8	0.09	0.17 ± 0.03
219949.442	S ₂ O	6 ₅ → 5 ₄	3.1	3.1	0.96	3.20 ± 0.04
338344.588	CH ₃ OH	7 ₋₁ → 6 ₋₁ , E	2.6	3.2	0.23	0.76 ± 0.03
338408.698	CH ₃ OH	7 ₀ → 6 ₀ , A+	2.6	2.5	0.32	0.85 ± 0.02
362736.048	H ₂ CO	5 ₀₅ → 4 ₀₄	2.7	2.9	0.43	1.31 ± 0.06

Table B.18. Observed line strengths towards CXO42.

Frequency [MHz]	Molecule	Transition	v_{LSR} [km s ⁻¹]	Δv [km s ⁻¹]	T_{mb} [K]	$\int T_{\text{mb}} dv$ [K km s ⁻¹]
218222.192	H ₂ CO	3 ₀₃ → 2 ₀₂	5.8	1.9	0.07	0.14 ± 0.02
219560.354	C ¹⁸ O	$J = 2 \rightarrow 1$	5.4	1.2	2.40	3.34 ± 0.02
337061.050	C ¹⁷ O	$J = 3 \rightarrow 2$	5.4	0.8	0.20	0.16 ± 0.02

Table B.19. Observed line strengths towards CrA-44.

Frequency [MHz]	Molecule	Transition	v_{LSR} [km s ⁻¹]	Δv [km s ⁻¹]	T_{mb} [K]	$\int T_{\text{mb}} dv$ [K km s ⁻¹]
216112.582	DCO ⁺	$J = 3 \rightarrow 2$	5.7	0.6	0.83	0.51 ± 0.02
216278.756	<i>c</i> -C ₃ H ₂	$3_{03} \rightarrow 2_{21}$	5.7	0.8	0.71	0.64 ± 0.02
216373.320	C ₂ D	$N = 3 \rightarrow 2, J = 7/2 \rightarrow 5/2, F = 5/2 \rightarrow 3/2$	6.0	1.4	0.20	0.28 ± 0.02
216373.320	C ₂ D	$N = 3 \rightarrow 2, J = 7/2 \rightarrow 5/2, F = 7/2 \rightarrow 5/2$
216428.320	C ₂ D	$N = 3 \rightarrow 2, J = 5/2 \rightarrow 3/2, F = 7/2 \rightarrow 5/2$	5.5	1.0	0.18	0.19 ± 0.02
216428.320	C ₂ D	$N = 3 \rightarrow 2, J = 5/2 \rightarrow 3/2, F = 5/2 \rightarrow 3/2$
217238.538	DCN	$J = 3 \rightarrow 2$	5.6	1.1	0.19	0.24 ± 0.02
217467.150	¹³ CN	$N = 2 \rightarrow 1, J = 5/2 \rightarrow 3/2, F_1 = 3 \rightarrow 2, F = 4 \rightarrow 3$	5.3	1.1	0.08	0.10 ± 0.02
217467.150	¹³ CN	$N = 2 \rightarrow 1, J = 5/2 \rightarrow 3/2, F_1 = 3 \rightarrow 2, F = 3 \rightarrow 2$
217822.148	<i>c</i> -C ₃ H ₂	$6_{06} \rightarrow 5_{15}$	5.7	1.0	0.65	0.73 ± 0.02
217822.148	<i>c</i> -C ₃ H ₂	$6_{16} \rightarrow 5_{05}$
217940.046	<i>c</i> -C ₃ H ₂	$5_{14} \rightarrow 4_{23}$	5.7	0.8	0.47	0.42 ± 0.02
218160.456	<i>c</i> -C ₃ H ₂	$5_{24} \rightarrow 4_{13}$	5.8	1.2	0.13	0.17 ± 0.02
218222.192	H ₂ CO	$3_{03} \rightarrow 2_{02}$	5.7	0.9	1.11	1.18 ± 0.02
219560.354	C ¹⁸ O	$J = 2 \rightarrow 1$	5.7	0.9	7.41	7.29 ± 0.02
219949.442	SO	$6_5 \rightarrow 5_4$	5.8	1.0	0.86	1.06 ± 0.03
337061.050	C ¹⁷ O	$J = 3 \rightarrow 2$	5.6	1.1	1.30	1.60 ± 0.04
340031.549	CN	$N = 3 \rightarrow 2, J = 5/2 \rightarrow 3/2, F = 7/2 \rightarrow 5/2$	5.5	1.4	0.33	0.47 ± 0.03
340035.408	CN	$N = 3 \rightarrow 2, J = 5/2 \rightarrow 3/2, F = 3/2 \rightarrow 1/2$	5.6	1.1	0.41	0.44 ± 0.03
340035.408	CN	$N = 3 \rightarrow 2, J = 5/2 \rightarrow 3/2, F = 5/2 \rightarrow 3/2$
340247.770	CN	$N = 3 \rightarrow 2, J = 7/2 \rightarrow 5/2, F = 7/2 \rightarrow 5/2$	5.4	1.8	0.82	1.57 ± 0.04
340247.770	CN	$N = 3 \rightarrow 2, J = 7/2 \rightarrow 5/2, F = 9/2 \rightarrow 7/2$
340714.155	SO	$7_8 \rightarrow 6_7$	5.5	1.5	0.33	0.51 ± 0.03

Table B.20. Observed line strengths towards CrA-33.

Frequency [MHz]	Molecule	Transition	v_{LSR} [km s ⁻¹]	Δv [km s ⁻¹]	T_{mb} [K]	$\int T_{\text{mb}} dv$ [K km s ⁻¹]
216112.582	DCO ⁺	$J = 3 \rightarrow 2$	5.7	0.4	0.55	0.26 ± 0.02
216278.756	<i>c</i> -C ₃ H ₂	$3_{03} \rightarrow 2_{21}$	5.7	0.1	0.17	0.06 ± 0.02
218222.192	H ₂ CO	$3_{03} \rightarrow 2_{02}$	5.7	0.4	0.76	0.31 ± 0.02
218440.063	CH ₃ OH	$4_2 \rightarrow 3_1, E$	5.7	0.5	0.17	0.10 ± 0.03
219560.354	C ¹⁸ O	$J = 2 \rightarrow 1$	5.7	0.8	4.51	3.92 ± 0.03
219949.442	SO	$6_5 \rightarrow 5_4$	5.7	0.3	0.45	0.15 ± 0.02
337061.050	C ¹⁷ O	$J = 3 \rightarrow 2$	5.6	0.7	0.24	0.18 ± 0.02

Table B.21. Observed line strengths towards VV CrA.

Frequency [MHz]	Molecule	Transition	v_{LSR} [km s ⁻¹]	Δv [km s ⁻¹]	T_{mb} [K]	$\int T_{\text{mb}} dv$ [K km s ⁻¹]
216112.582	DCO ⁺	$J = 3 \rightarrow 2$	4.9	0.7	0.15	0.12 ± 0.01
216278.756	<i>c</i> -C ₃ H ₂	$3_{03} \rightarrow 2_{21}$	5.0	0.7	0.13	0.09 ± 0.01
217238.538	DCN	$J = 3 \rightarrow 2$	4.8	0.8	0.05	0.04 ± 0.01
217822.148	<i>c</i> -C ₃ H ₂	$6_{06} \rightarrow 5_{15}$	5.0	0.8	0.13	0.12 ± 0.01
217822.148	<i>c</i> -C ₃ H ₂	$6_{16} \rightarrow 5_{05}$
217940.046	<i>c</i> -C ₃ H ₂	$5_{14} \rightarrow 4_{23}$	5.1	0.8	0.08	0.07 ± 0.01
218222.192	H ₂ CO	$3_{03} \rightarrow 2_{02}$	4.9	0.9	0.78	0.79 ± 0.02
218475.632	H ₂ CO	$3_{22} \rightarrow 2_{21}$	4.8	1.3	0.06	0.09 ± 0.02
218760.066	H ₂ CO	$3_{21} \rightarrow 2_{20}$	5.0	1.4	0.07	0.12 ± 0.02
219560.354	C ¹⁸ O	$J = 2 \rightarrow 1$	4.9	0.9	5.48	6.12 ± 0.02
219949.442	SO	$6_5 \rightarrow 5_4$	5.0	1.3	0.84	1.39 ± 0.02
337061.050	C ¹⁷ O	$J = 3 \rightarrow 2$	4.9	1.0	0.76	0.86 ± 0.02
340031.549	CN	$N = 3 \rightarrow 2, J = 5/2 \rightarrow 3/2, F = 7/2 \rightarrow 5/2$	4.8	1.4	0.20	0.29 ± 0.02
340035.408	CN	$N = 3 \rightarrow 2, J = 5/2 \rightarrow 3/2, F = 3/2 \rightarrow 1/2$	4.8	1.2	0.19	0.25 ± 0.02
340035.408	CN	$N = 3 \rightarrow 2, J = 5/2 \rightarrow 3/2, F = 5/2 \rightarrow 3/2$
340247.770	CN	$N = 3 \rightarrow 2, J = 7/2 \rightarrow 5/2, F = 7/2 \rightarrow 5/2$	4.7	1.5	0.57	0.95 ± 0.02
340247.770	CN	$N = 3 \rightarrow 2, J = 7/2 \rightarrow 5/2, F = 9/2 \rightarrow 7/2$
340714.155	SO	$7_8 \rightarrow 6_7$	4.8	2.0	0.31	0.69 ± 0.03

Table B.22. Observed line strengths towards CrA-37.

Frequency [MHz]	Molecule	Transition	v_{LSR} [km s ⁻¹]	Δv [km s ⁻¹]	T_{mb} [K]	$\int T_{\text{mb}} dv$ [K km s ⁻¹]
219560.354	C ¹⁸ O	$J = 2 \rightarrow 1$	5.7	0.6	1.12	0.72 ± 0.03

Appendix C: Complete IRS7B spectrum at 217–245.5 GHz

All spectra in this and the next section are cut off at 0.5 K to also show the weaker spectral lines.

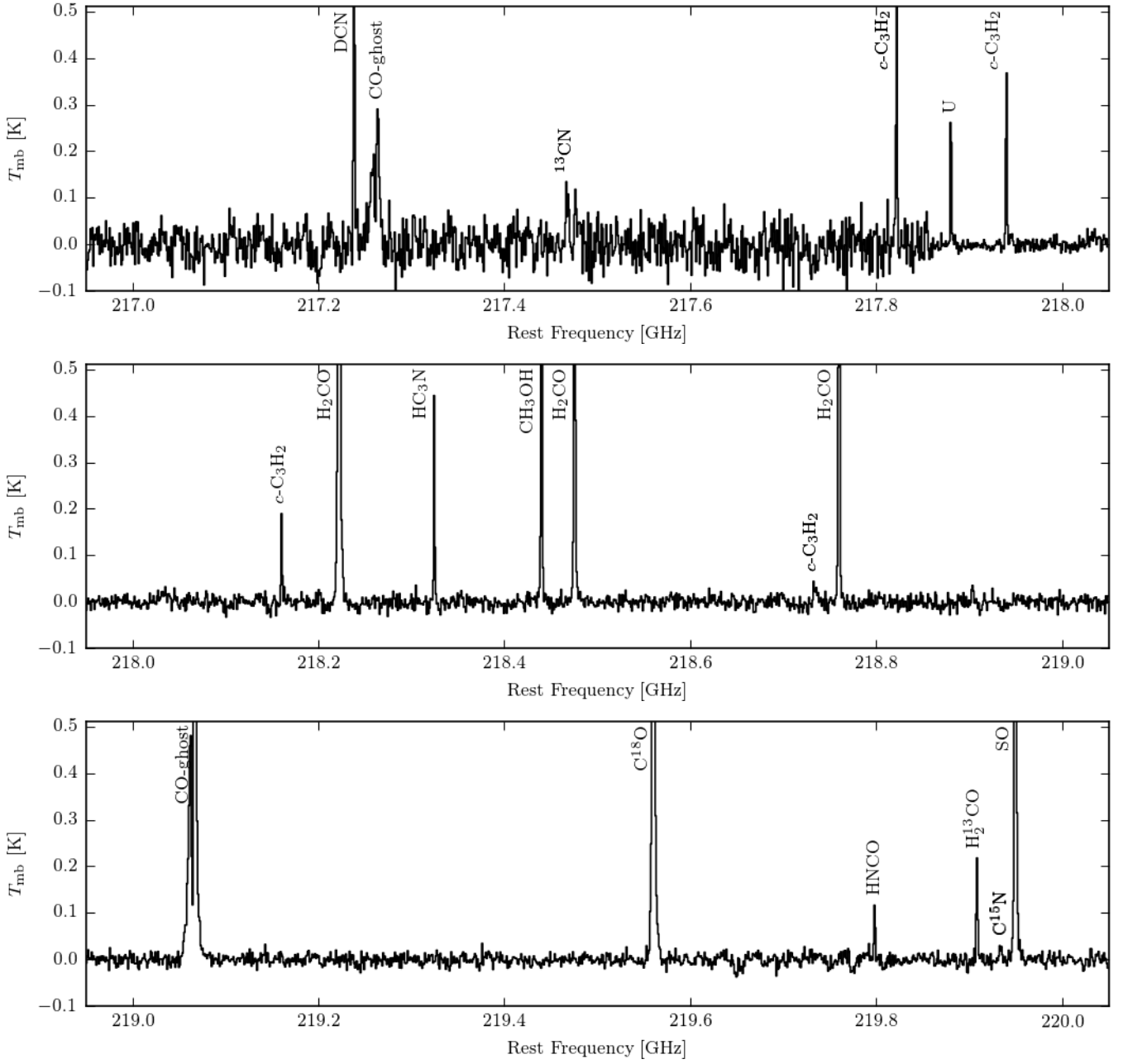


Fig. C.1. Full spectrum of IRS7B, smoothed by a factor 8, corresponding to a channel width of 1.2–1.4 km s⁻¹.

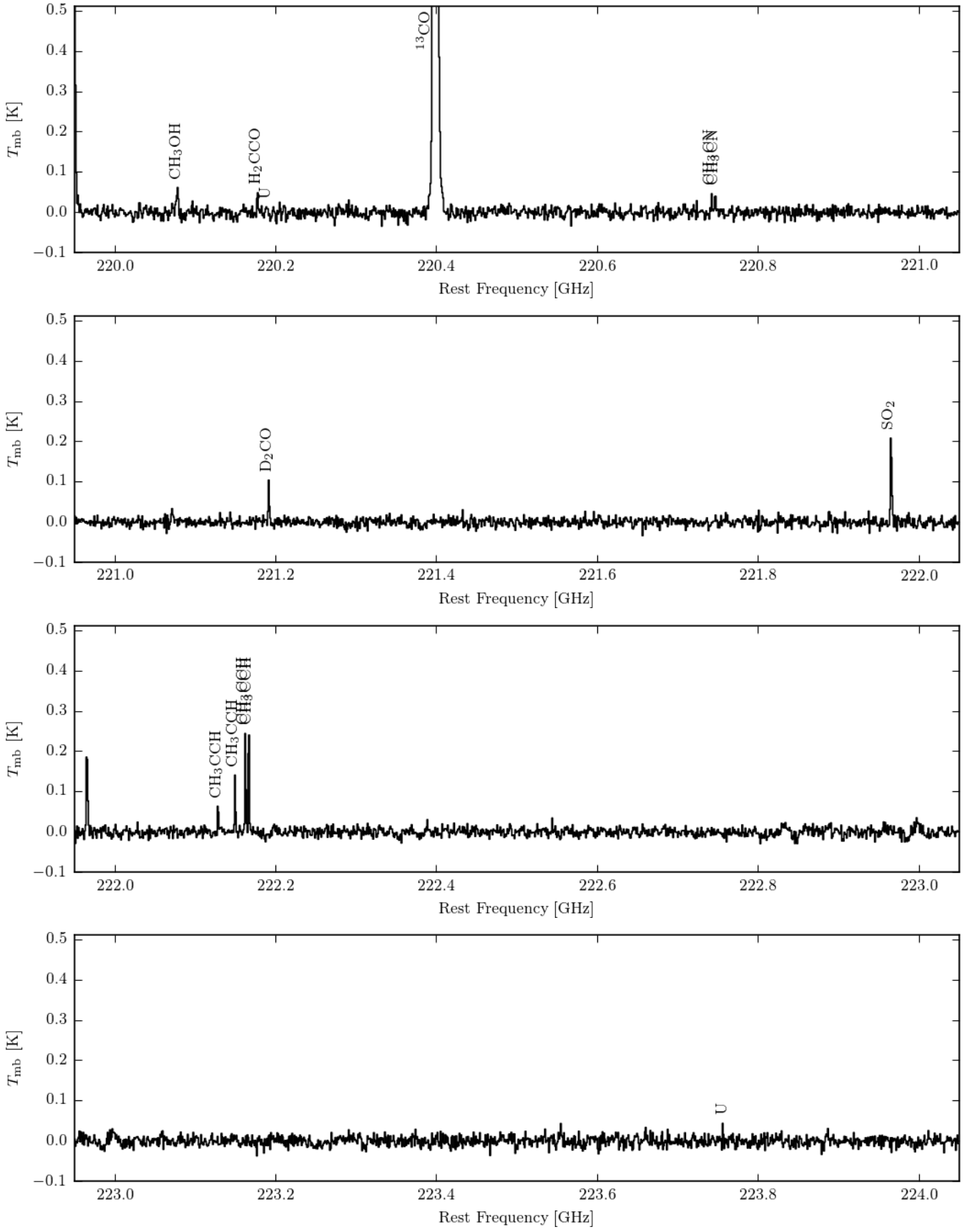


Fig. C.2. See Fig. C.1.

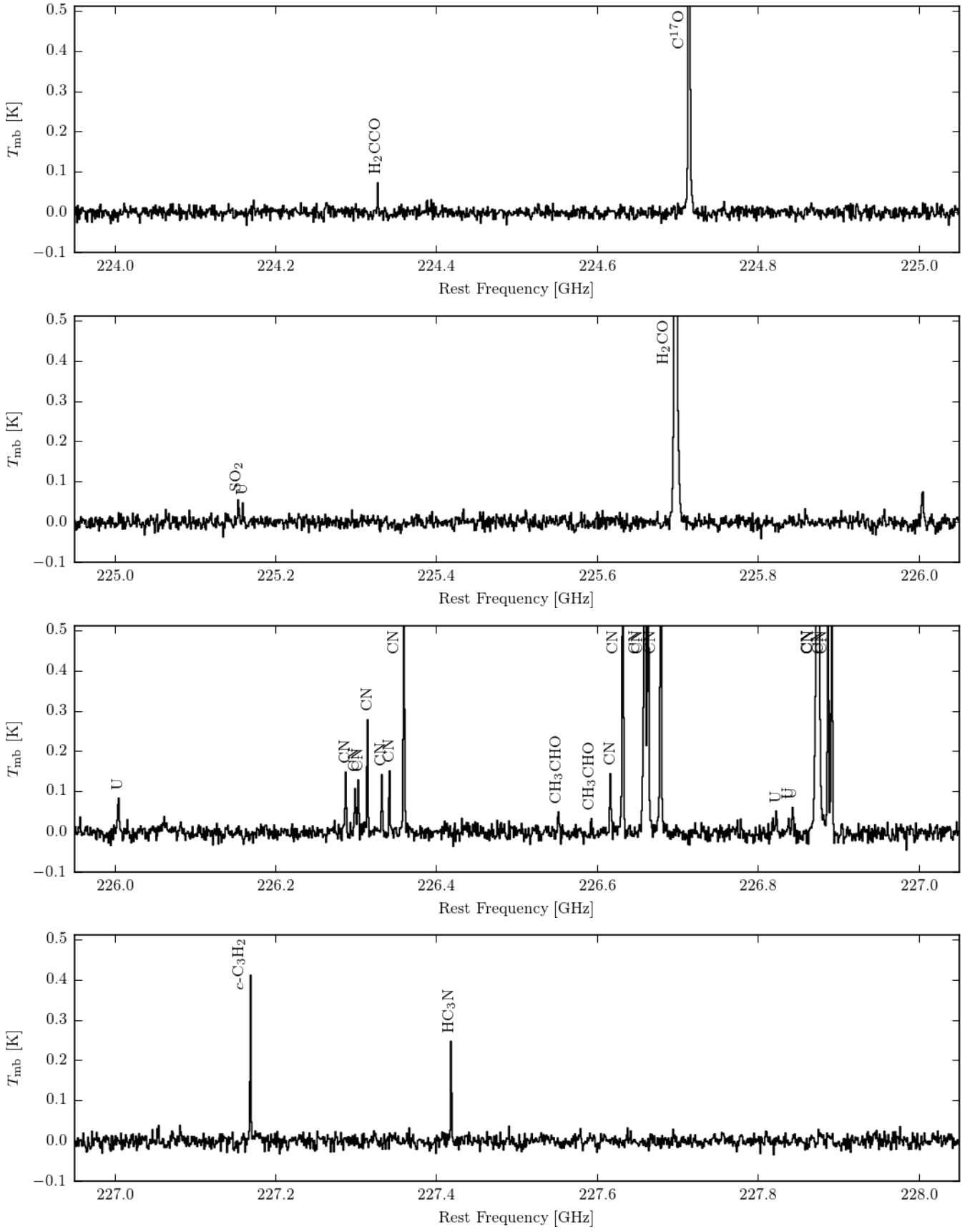
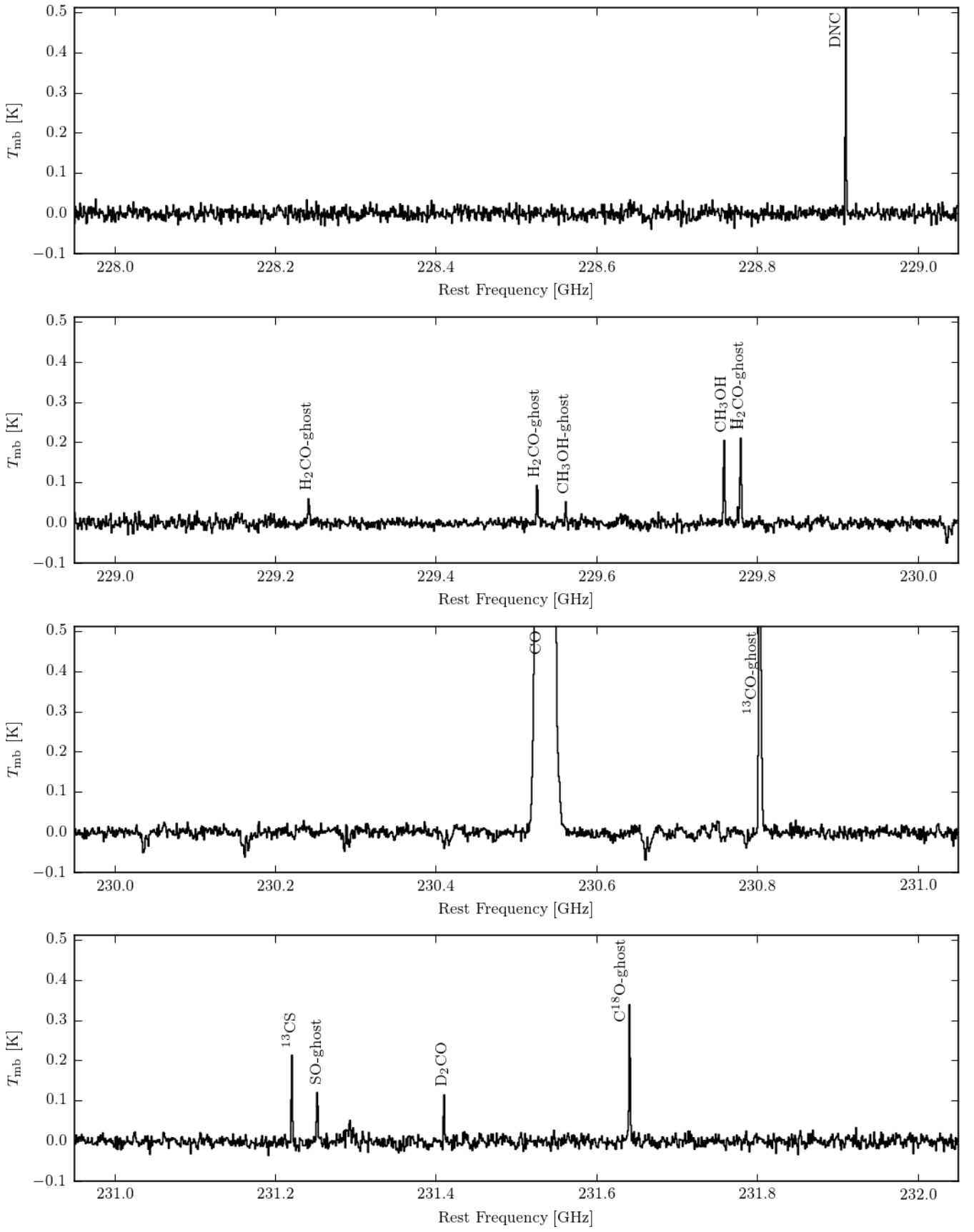
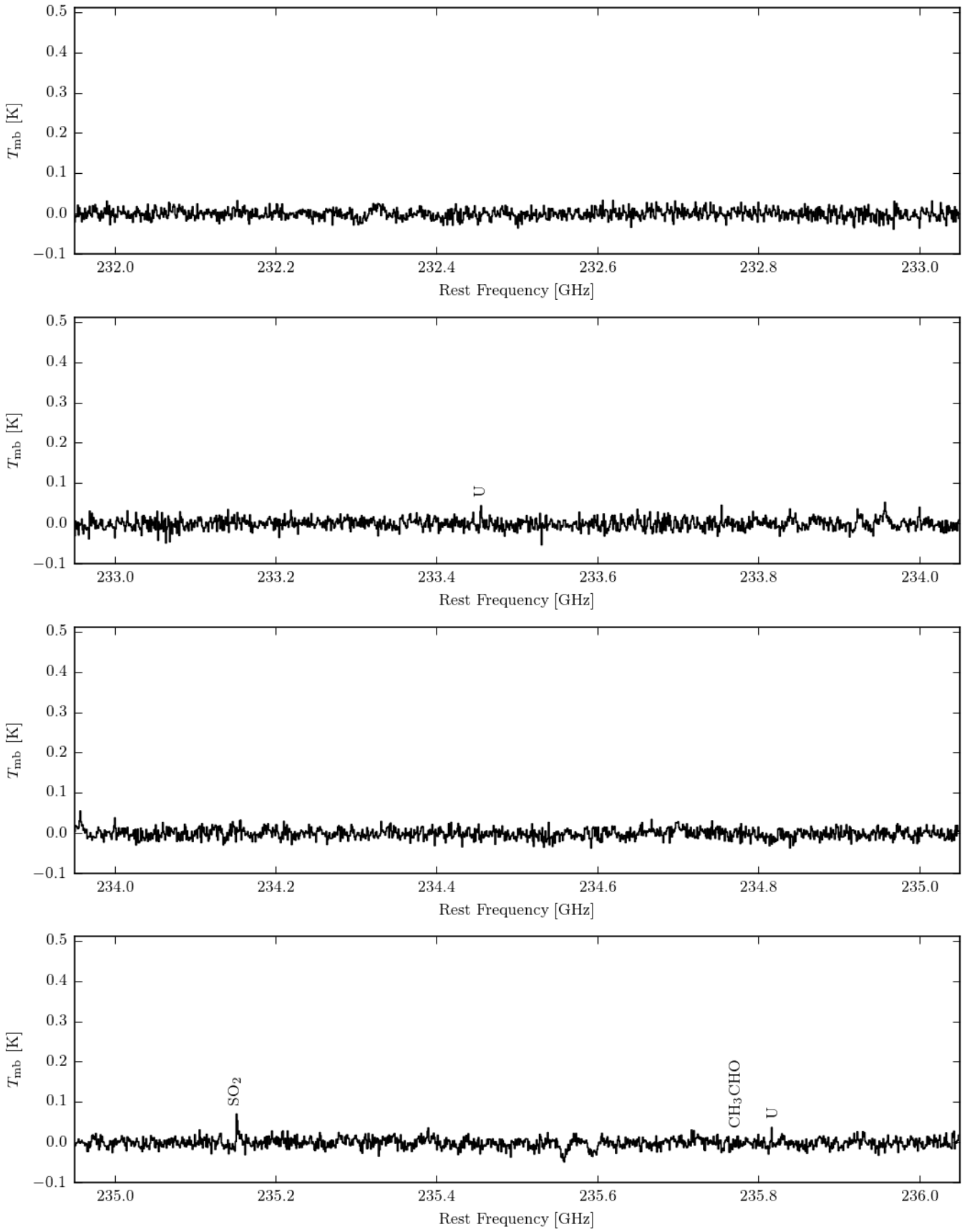


Fig. C.3. See Fig. C.1.

**Fig. C.4.** See Fig. C.1.

**Fig. C.5.** See Fig. C.1.

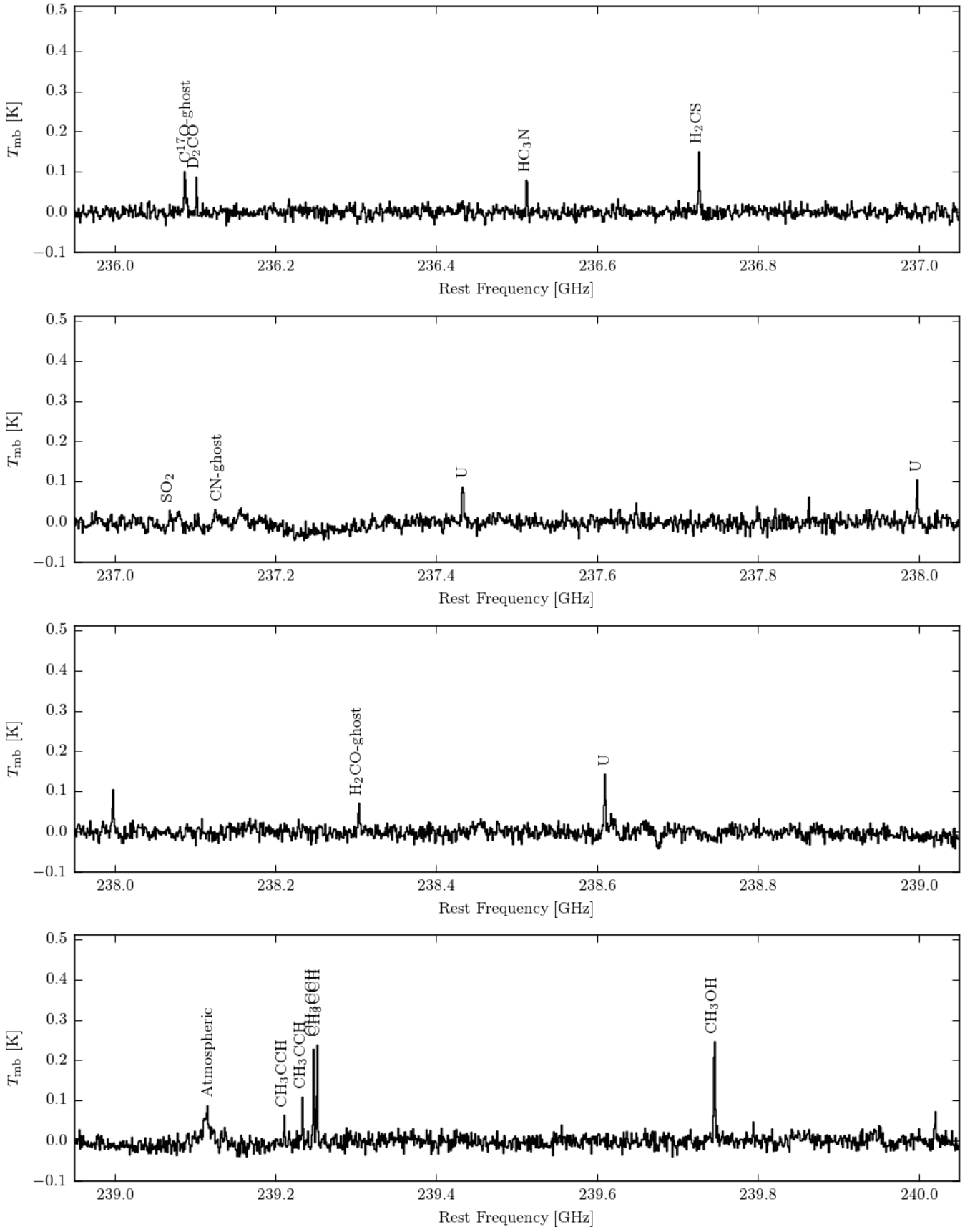


Fig. C.6. See Fig. C.1.

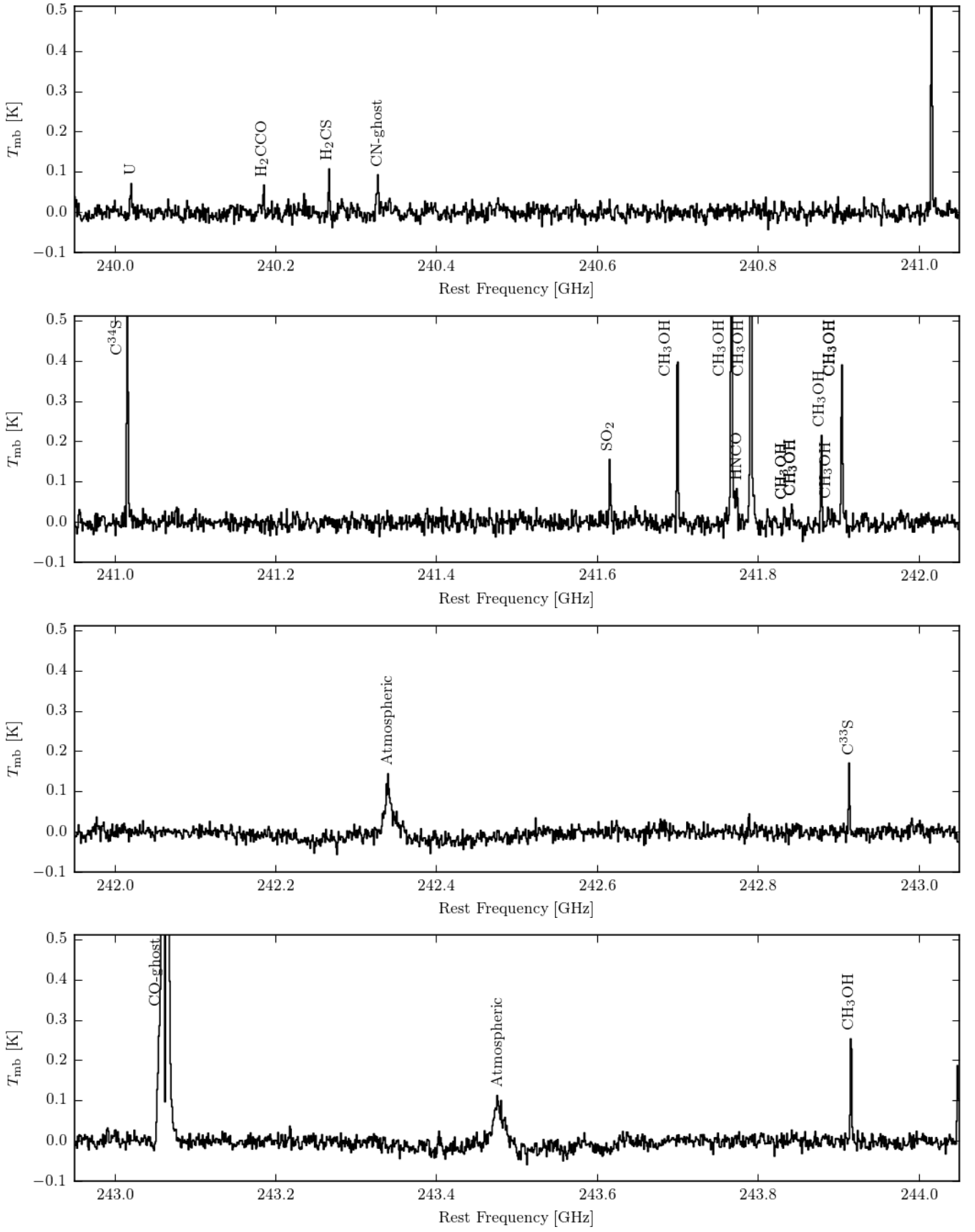


Fig. C.7. See Fig. C.1.

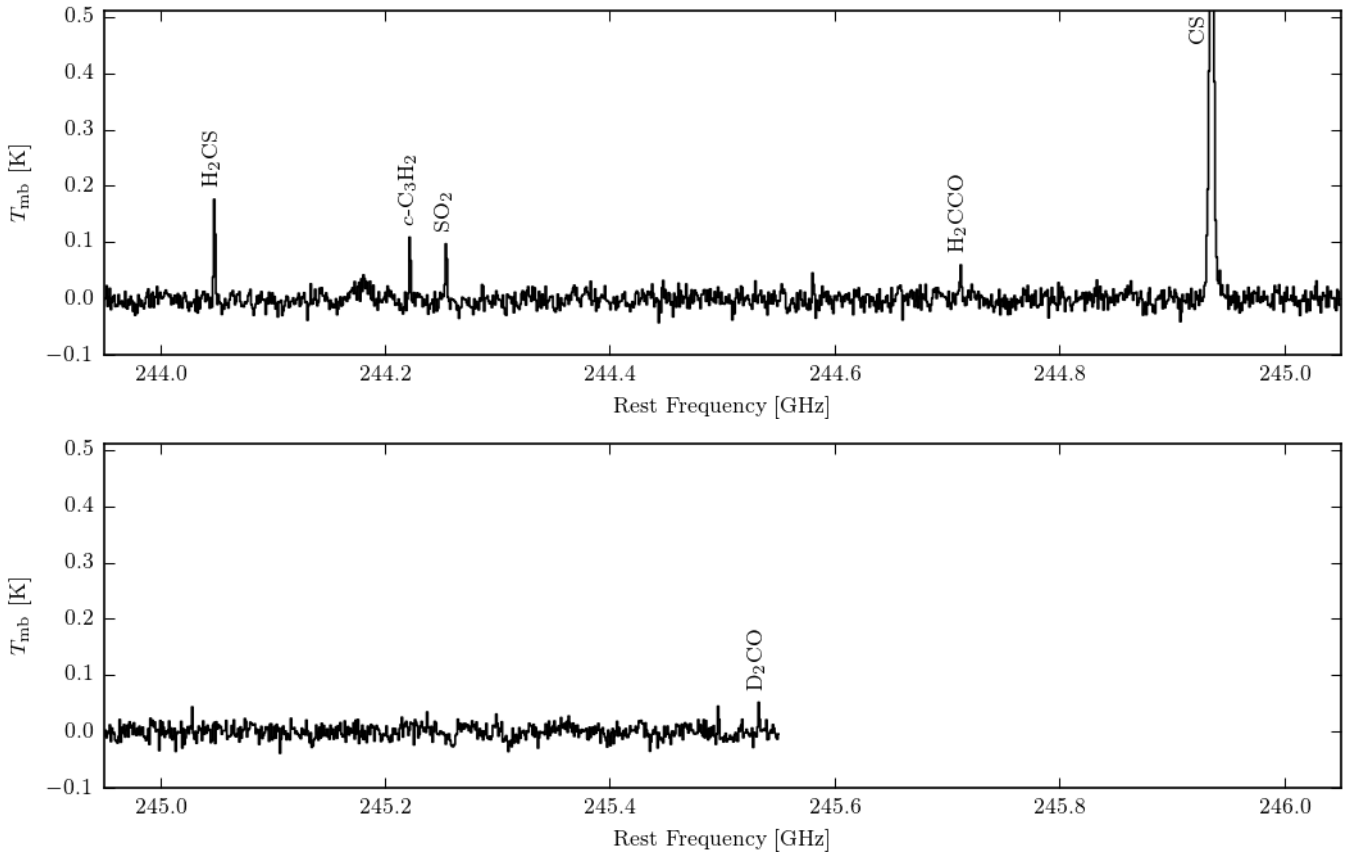
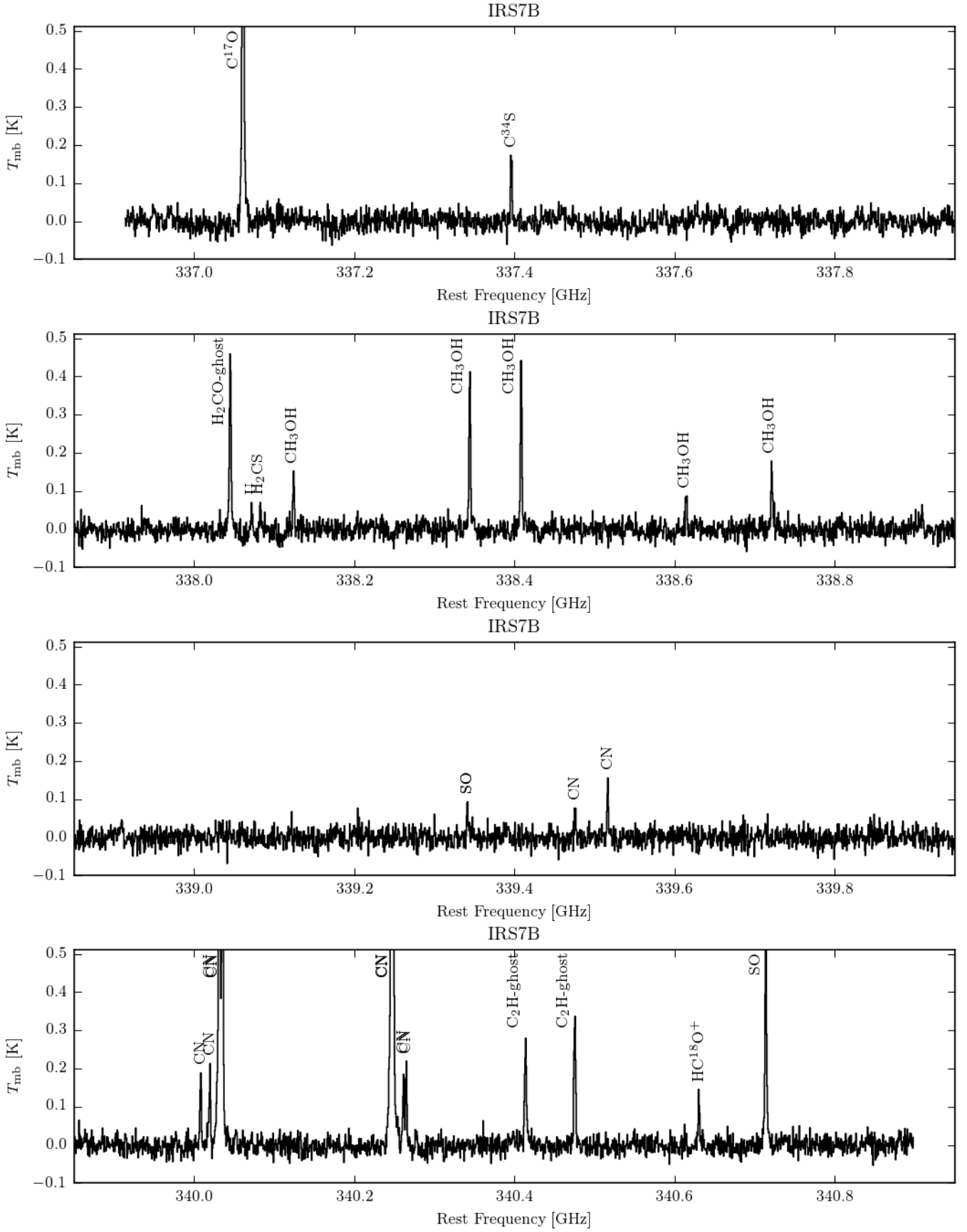


Fig. C.8. See Fig. C.1.

Appendix D: Complete spectra of the H₂CO, CH₃OH, and *c*-C₃H₂ survey**Fig. D.1.** 0.9 mm spectrum of IRS7B, smoothed by a factor 8, corresponding to a channel width of 0.6 km s^{-1} .

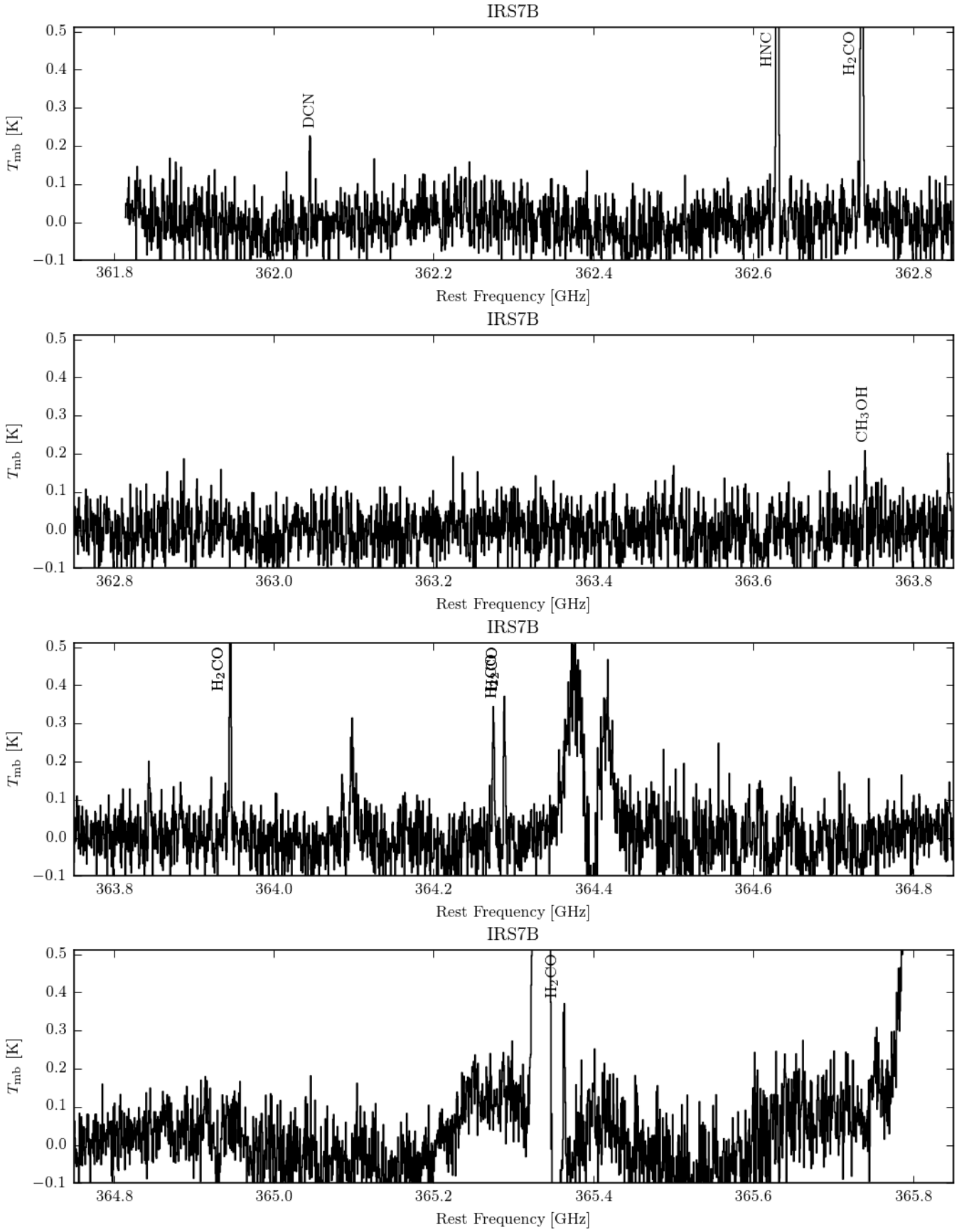


Fig. D.2. 0.8 mm spectrum of IRS7B, smoothed by a factor 8, corresponding to a channel width of 0.5 km s^{-1} . Strong atmospheric lines are visible at 364.1 GHz, 364.4 GHz, and 365.3 GHz.

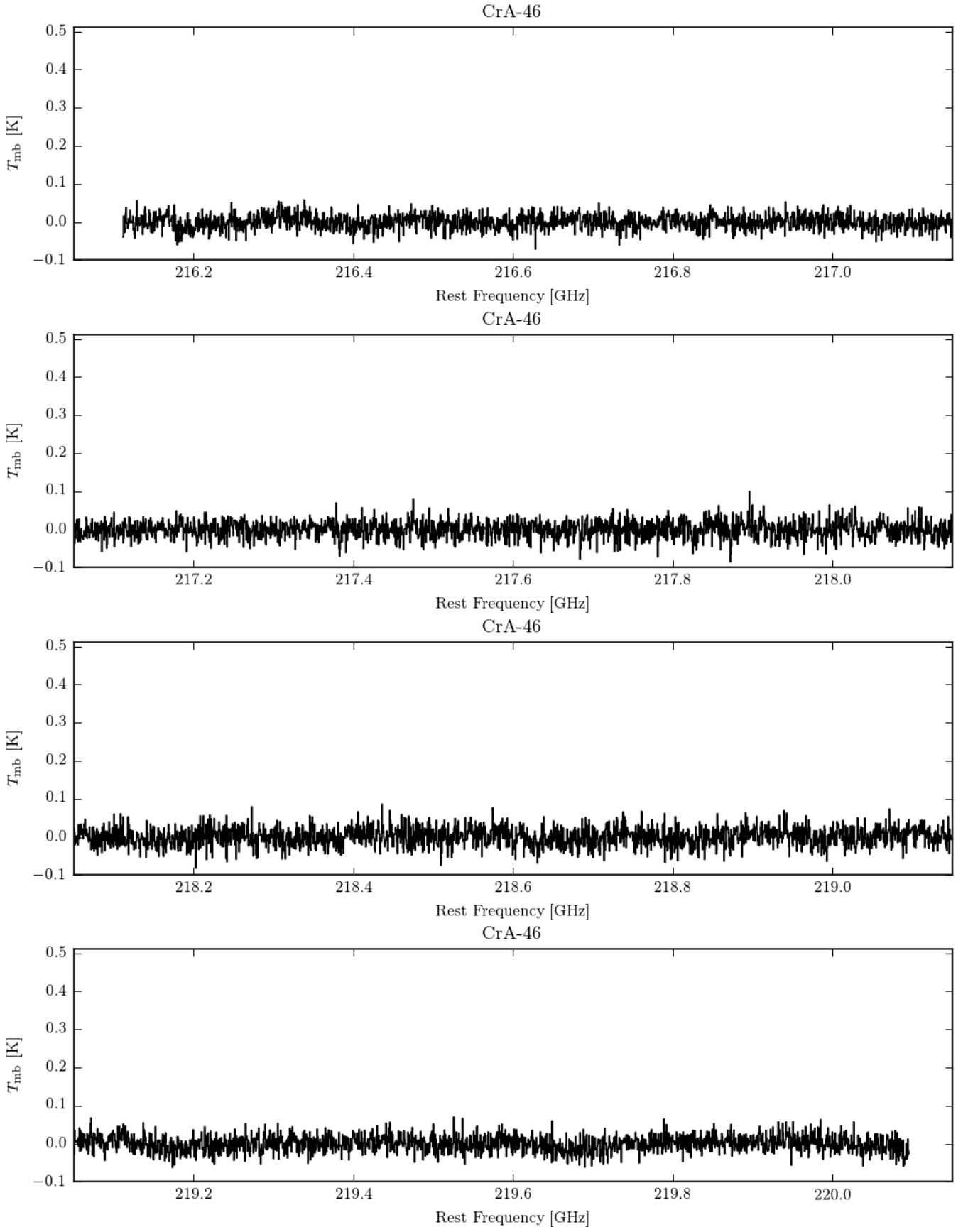


Fig. D.3. 1.4 mm spectrum of CrA-46, smoothed by a factor 8, corresponding to a channel width of 0.8 km s^{-1} .

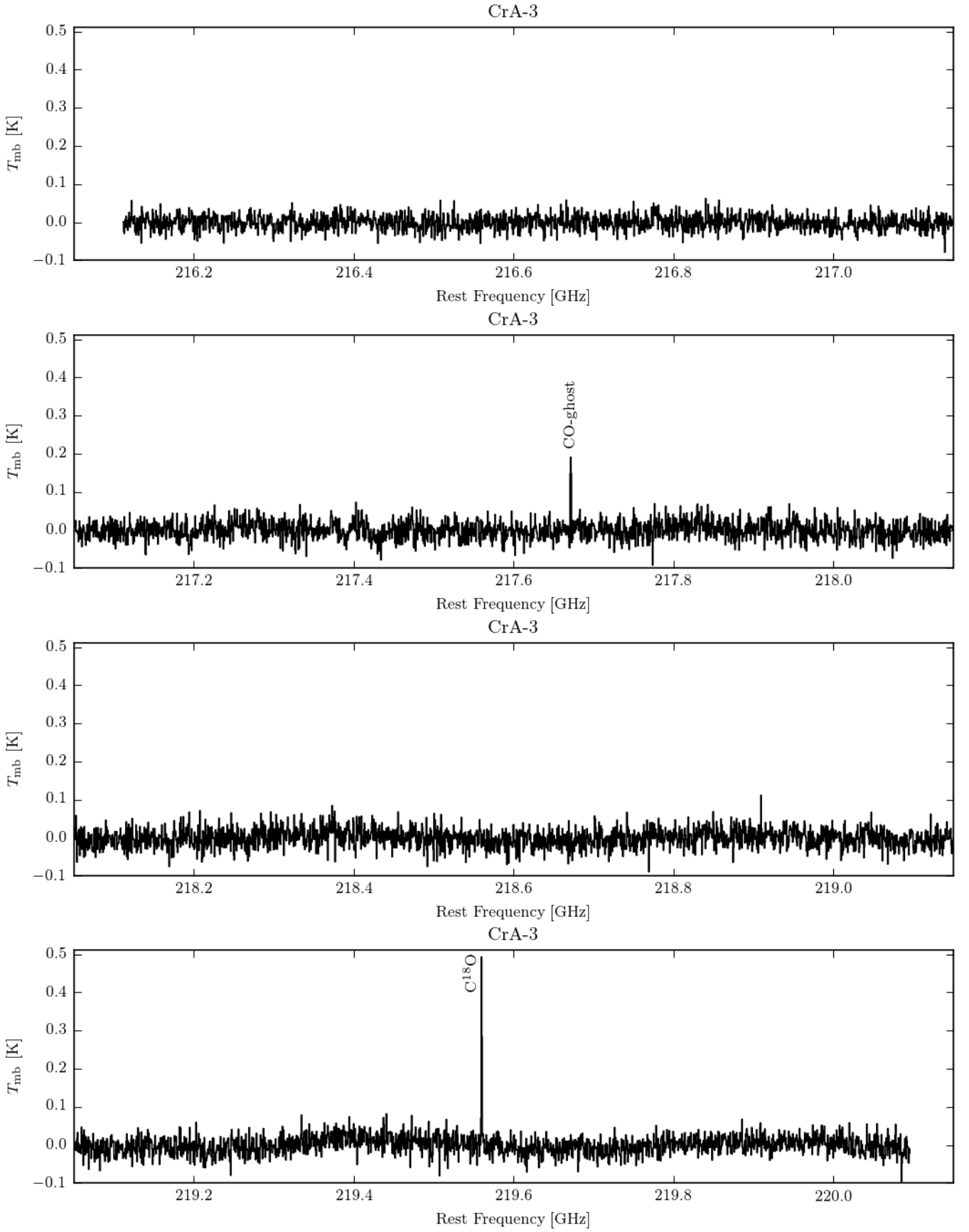


Fig. D.4. 1.4 mm spectrum of CrA-3, smoothed by a factor 8, corresponding to a channel width of 0.8 km s^{-1} .

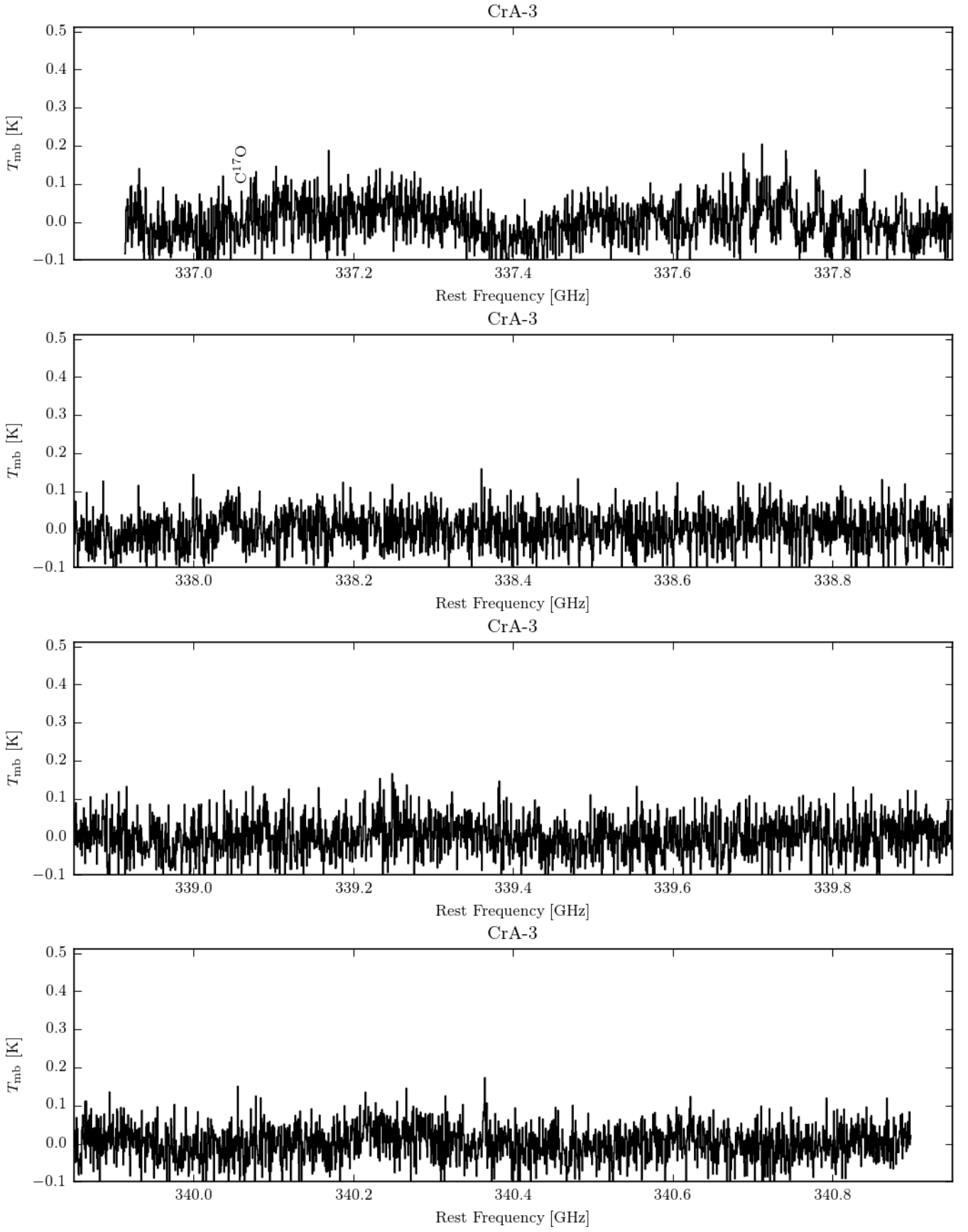


Fig. D.5. 0.9 mm spectrum of CrA-3, smoothed by a factor 8, corresponding to a channel width of 0.6 km s^{-1} .

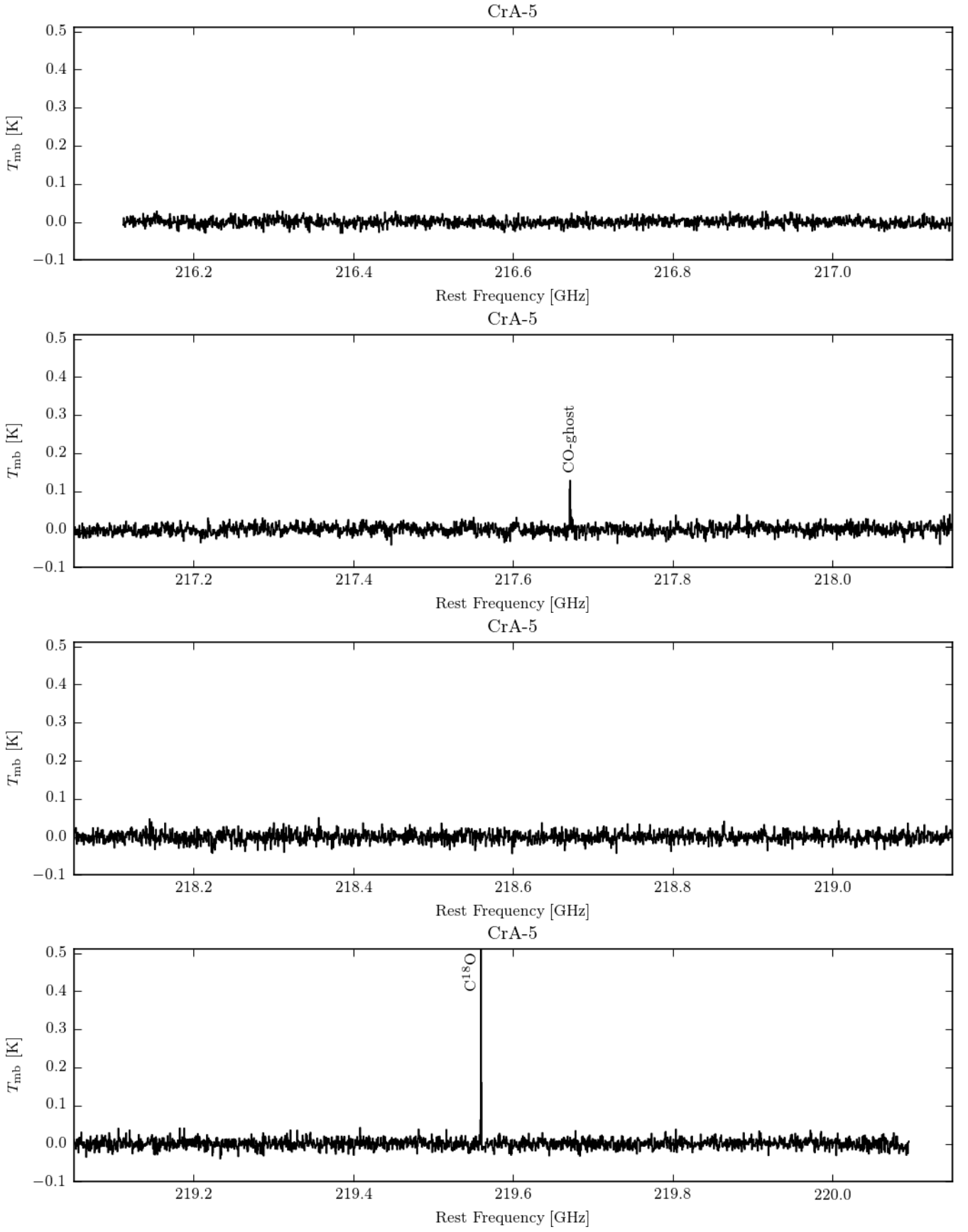


Fig. D.6. 1.4 mm spectrum of CrA-5, smoothed by a factor 8, corresponding to a channel width of 0.8 km s^{-1} .

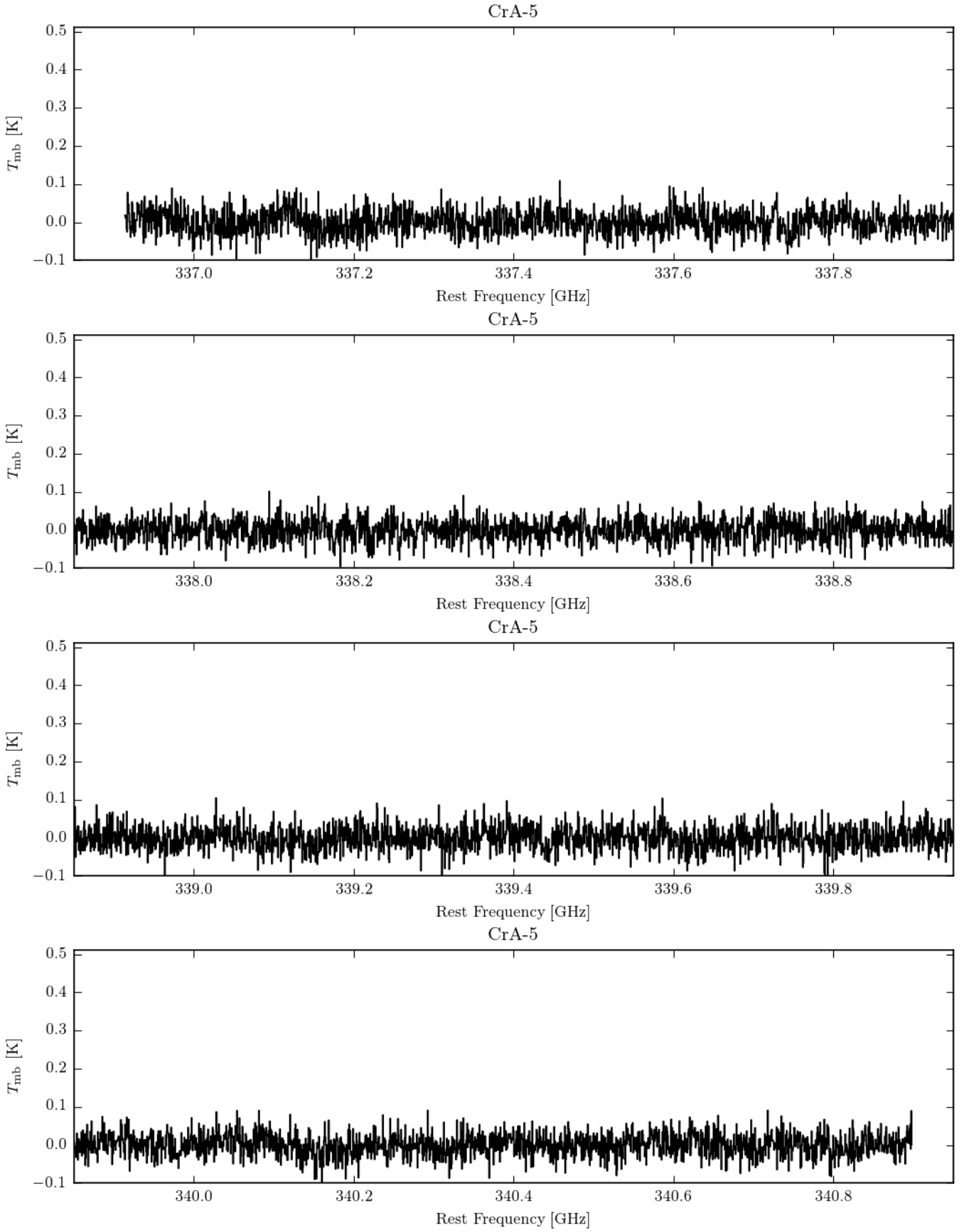


Fig. D.7. 0.9 mm spectrum of CrA-5, smoothed by a factor 8, corresponding to a channel width of 0.6 km s^{-1} .

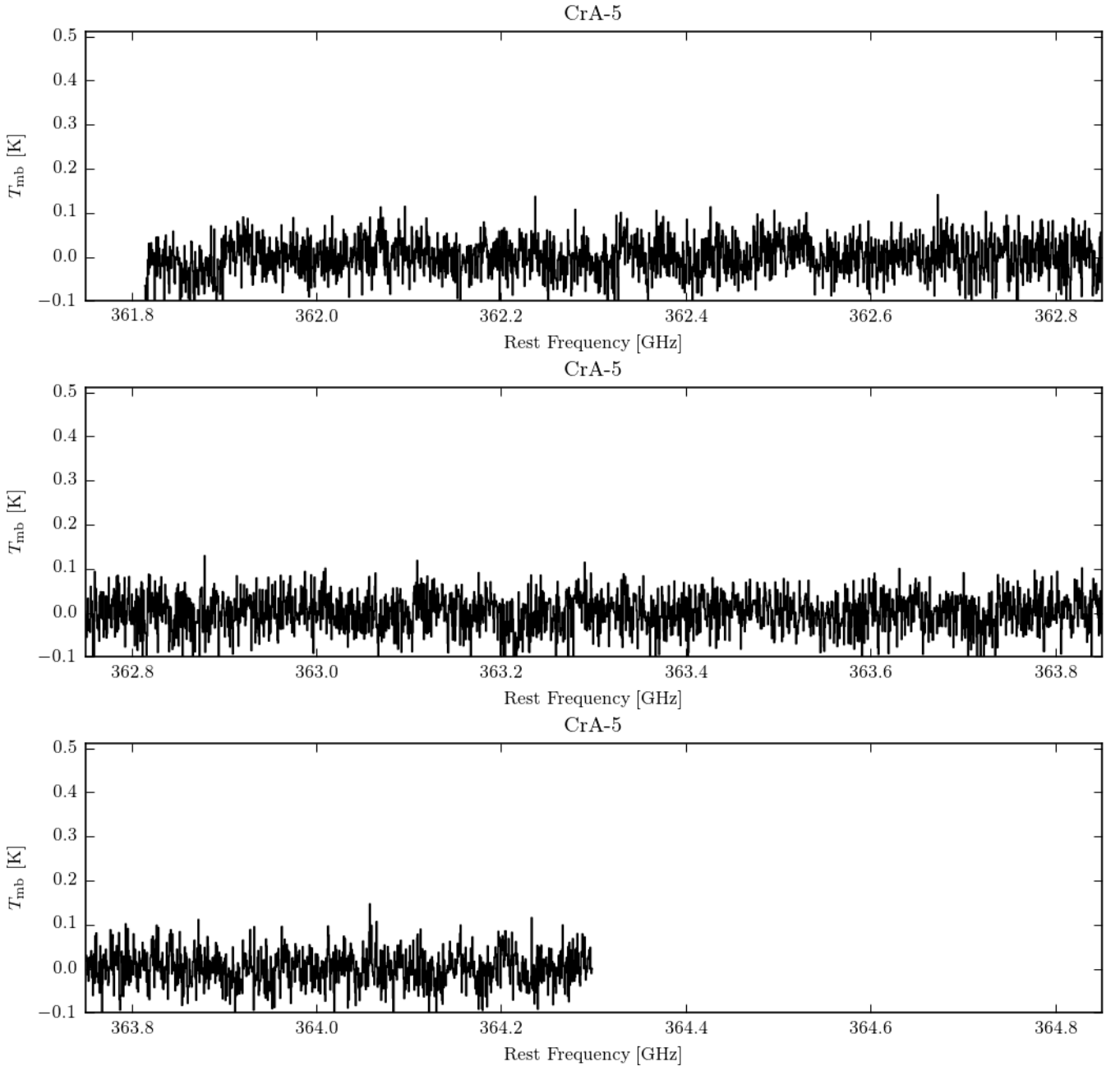


Fig. D.8. 0.8 mm spectrum of CrA-5, smoothed by a factor 8, corresponding to a channel width of 0.5 km s^{-1} .

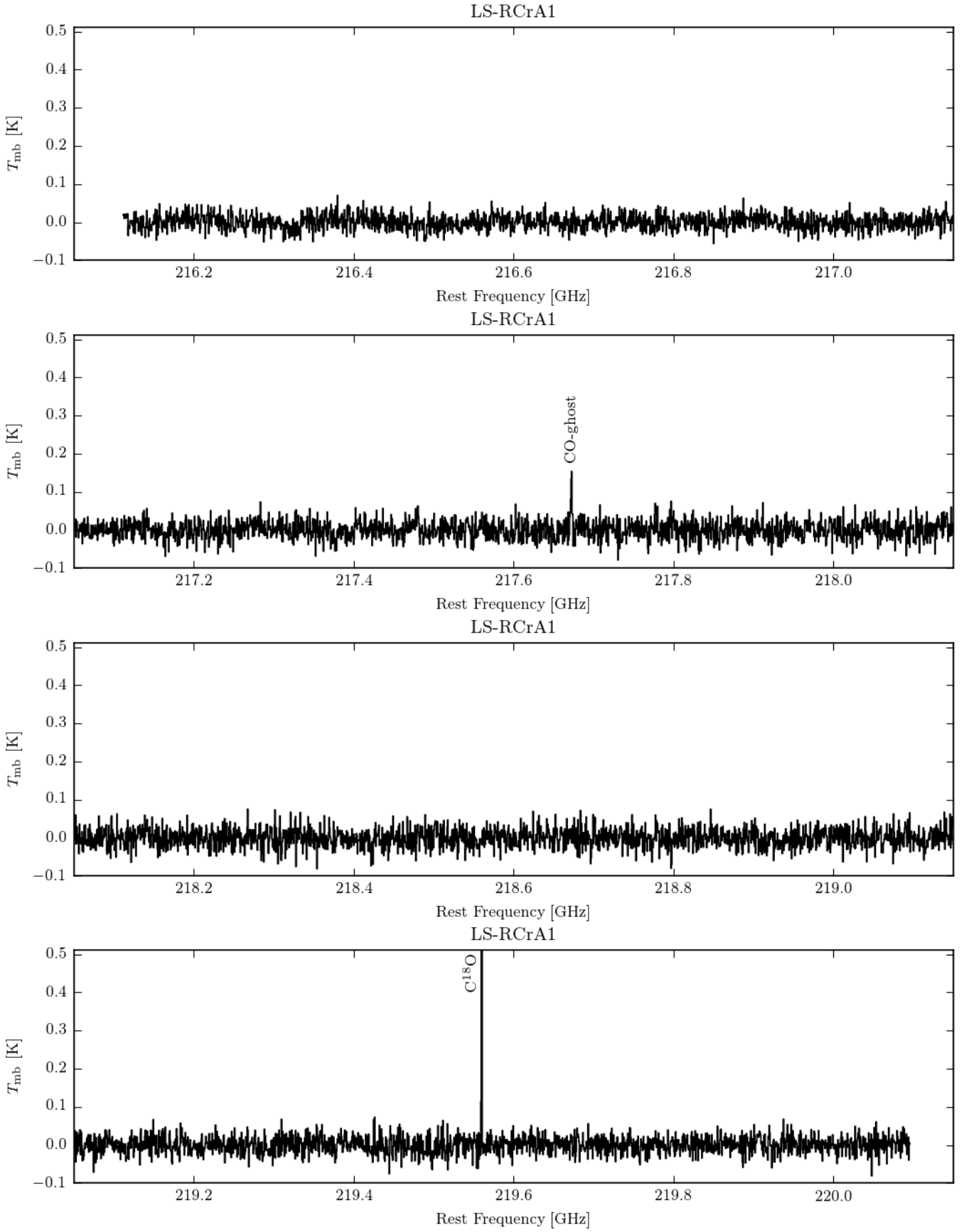


Fig. D.9. 1.4 mm spectrum of LS-RCrA1, smoothed by a factor 8, corresponding to a channel width of 0.8 km s^{-1} .

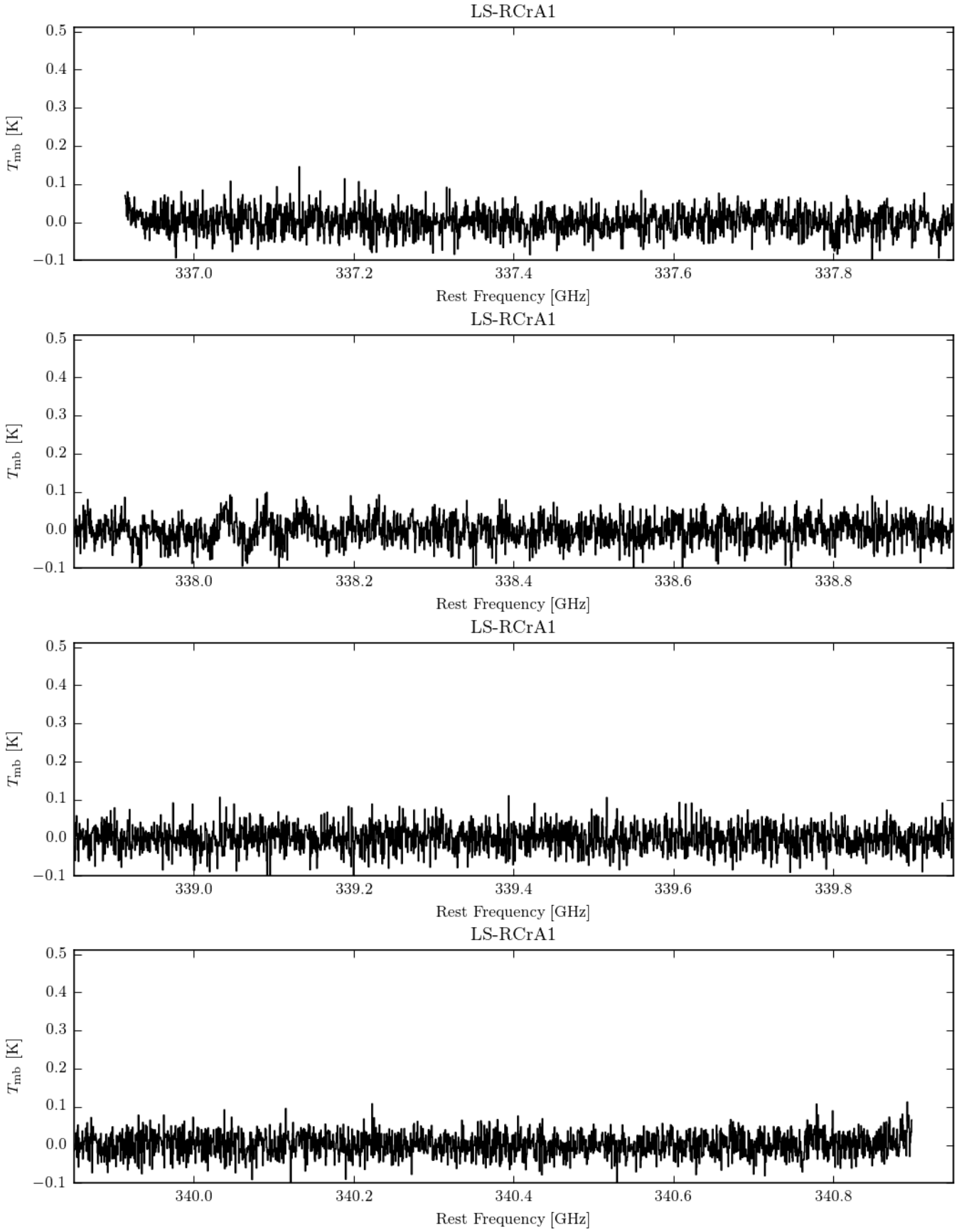


Fig. D.10. 0.9 mm spectrum of LS-RCrA1, smoothed by a factor 8, corresponding to a channel width of 0.6 km s^{-1} .

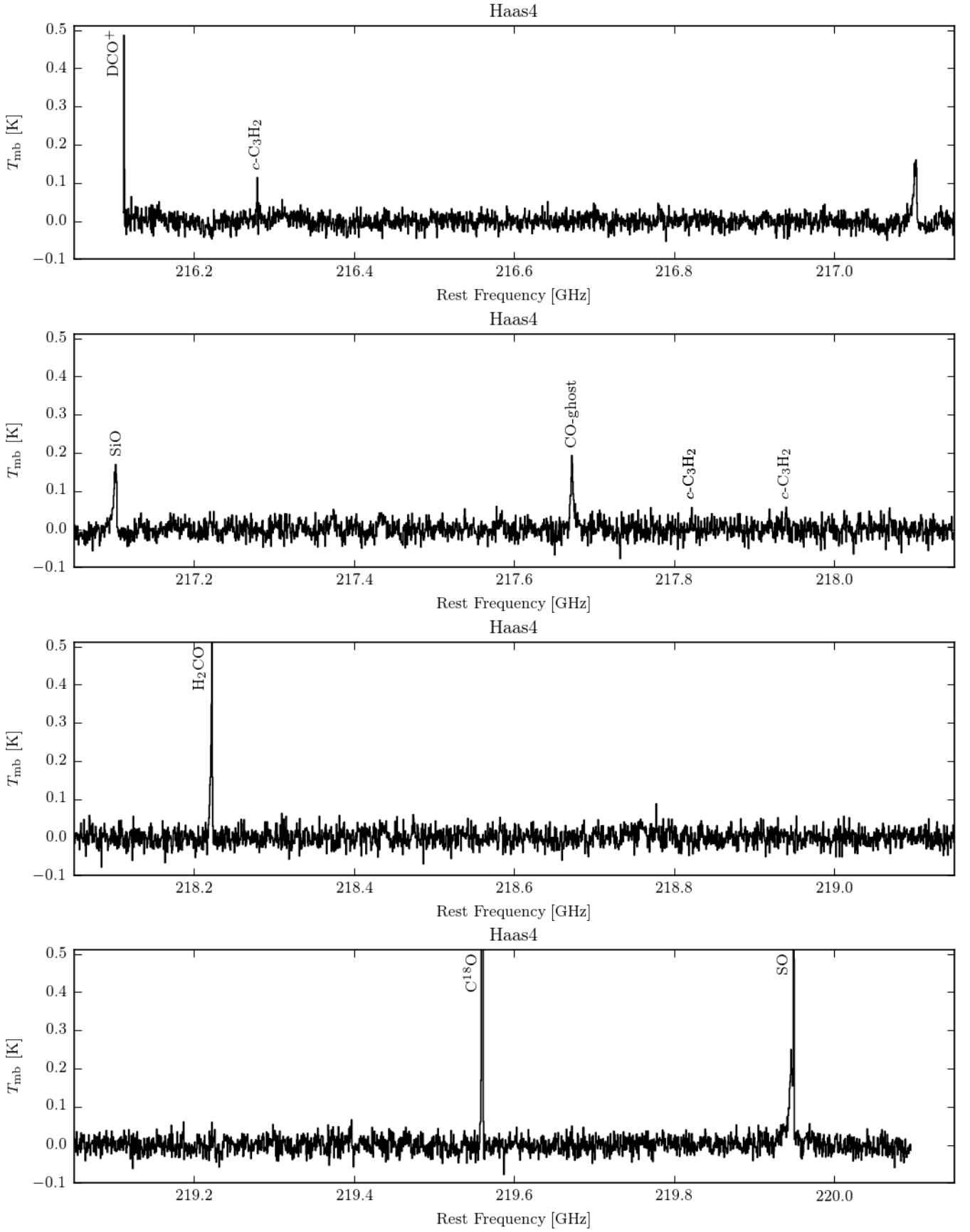


Fig. D.11. 1.4 mm spectrum of Haas4, smoothed by a factor 8, corresponding to a channel width of 0.8 km s^{-1} .

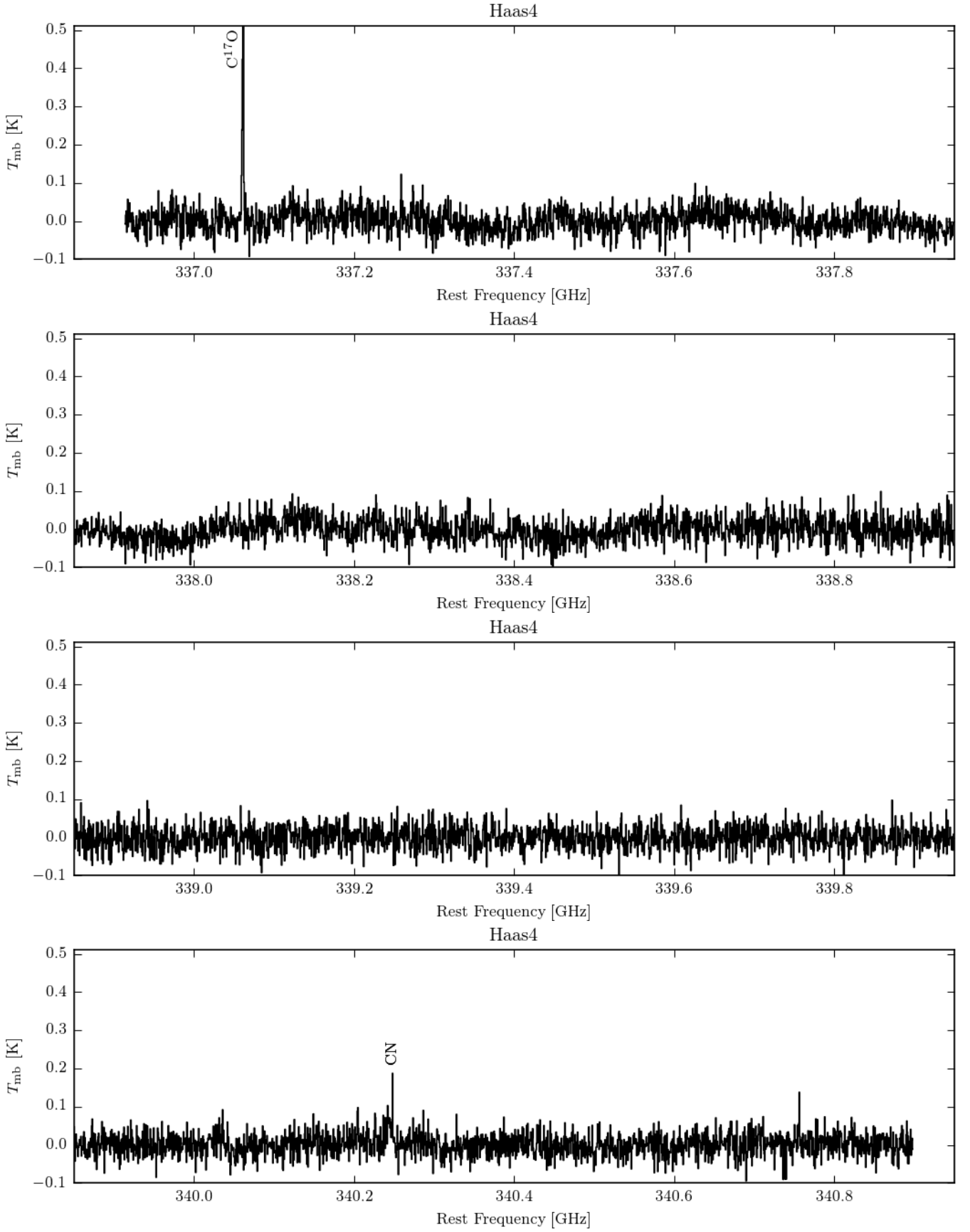


Fig. D.12. 0.9 mm spectrum of Haas4, smoothed by a factor 8, corresponding to a channel width of 0.6 km s^{-1} .

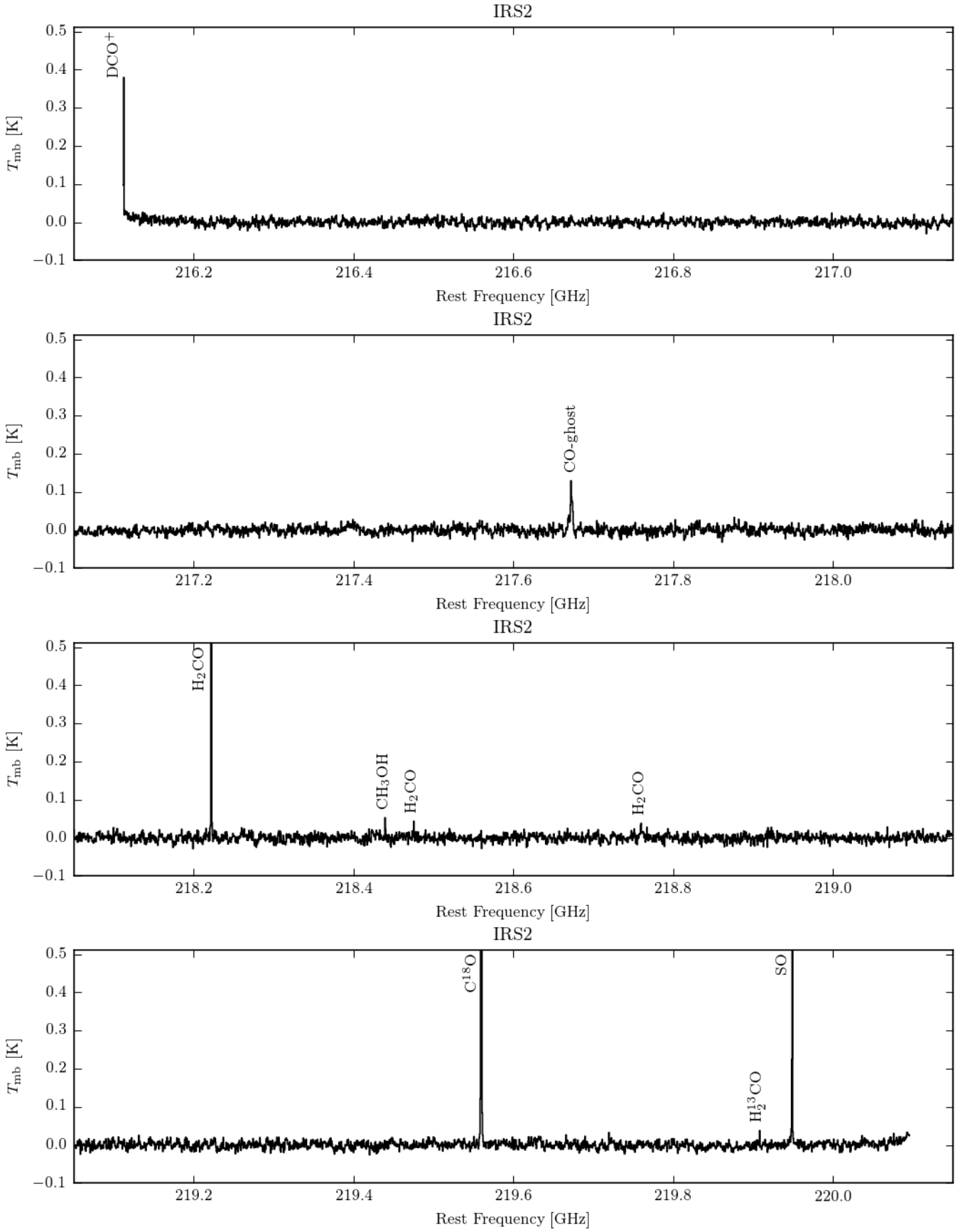


Fig. D.13. 1.4 mm spectrum of IRS2, smoothed by a factor 8, corresponding to a channel width of 0.8 km s^{-1} .

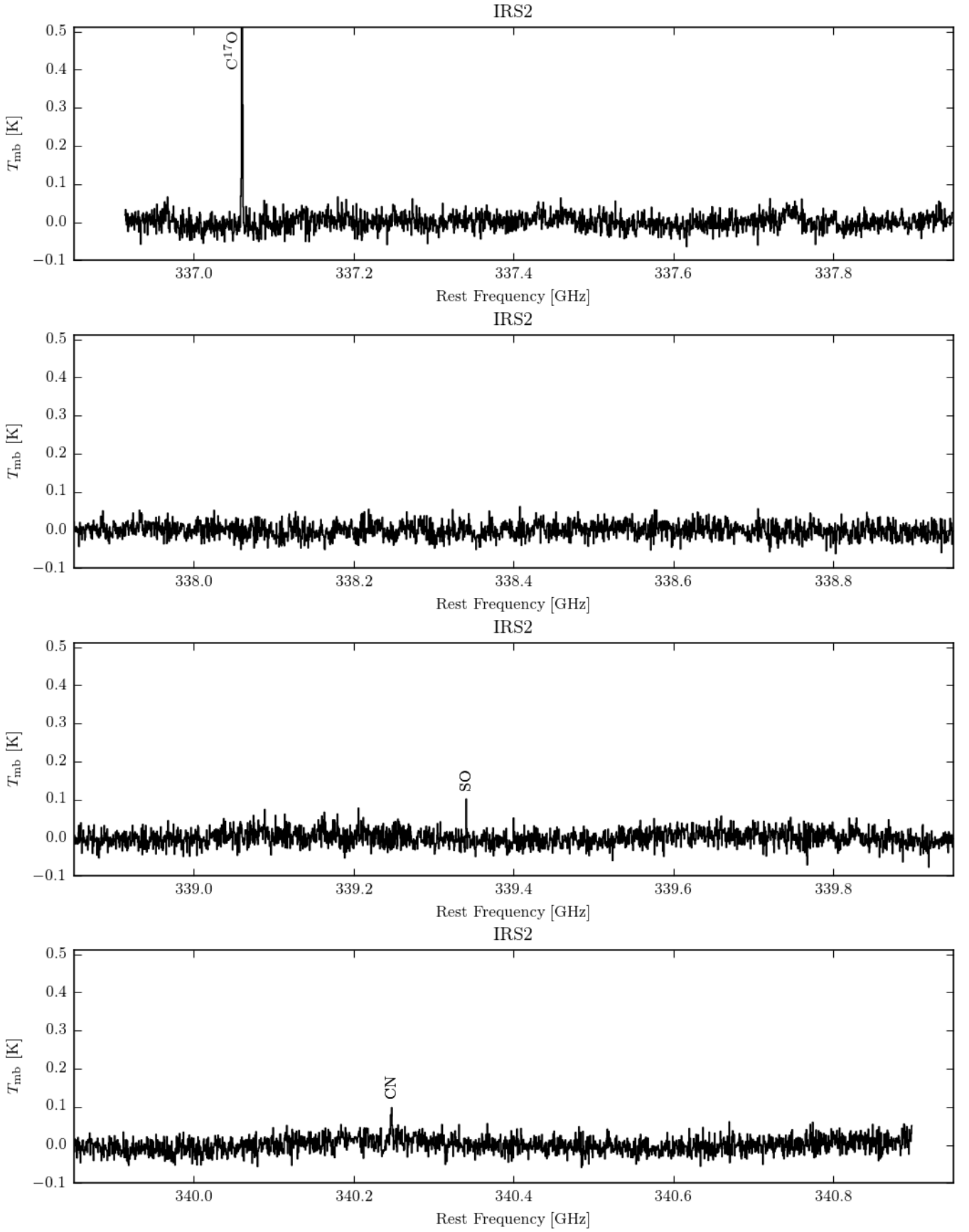


Fig. D.14. 0.9 mm spectrum of IRS2, smoothed by a factor 8, corresponding to a channel width of 0.6 km s^{-1} .

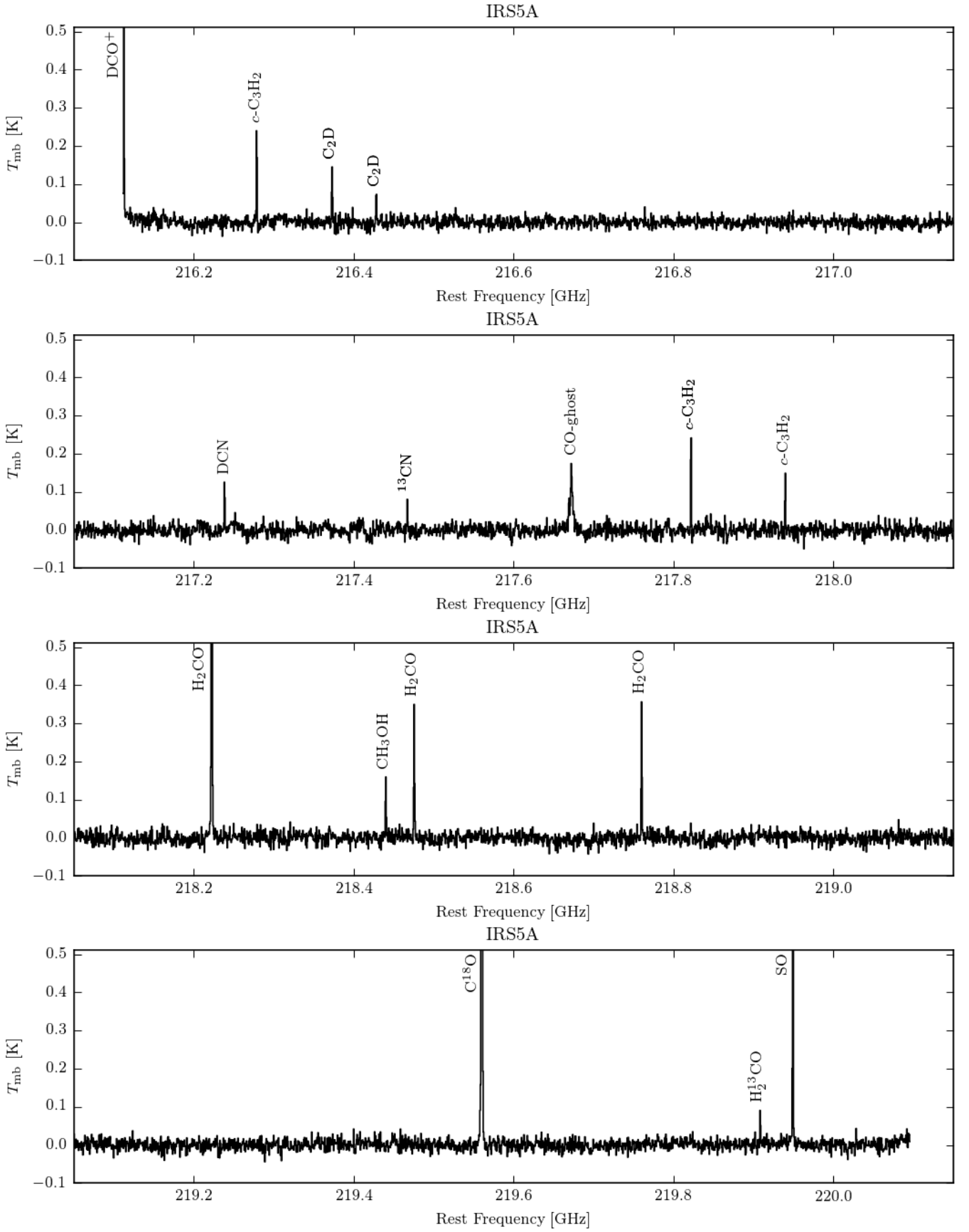


Fig. D.15. 1.4 mm spectrum of IRS5A, smoothed by a factor 8, corresponding to a channel width of 0.8 km s^{-1} .

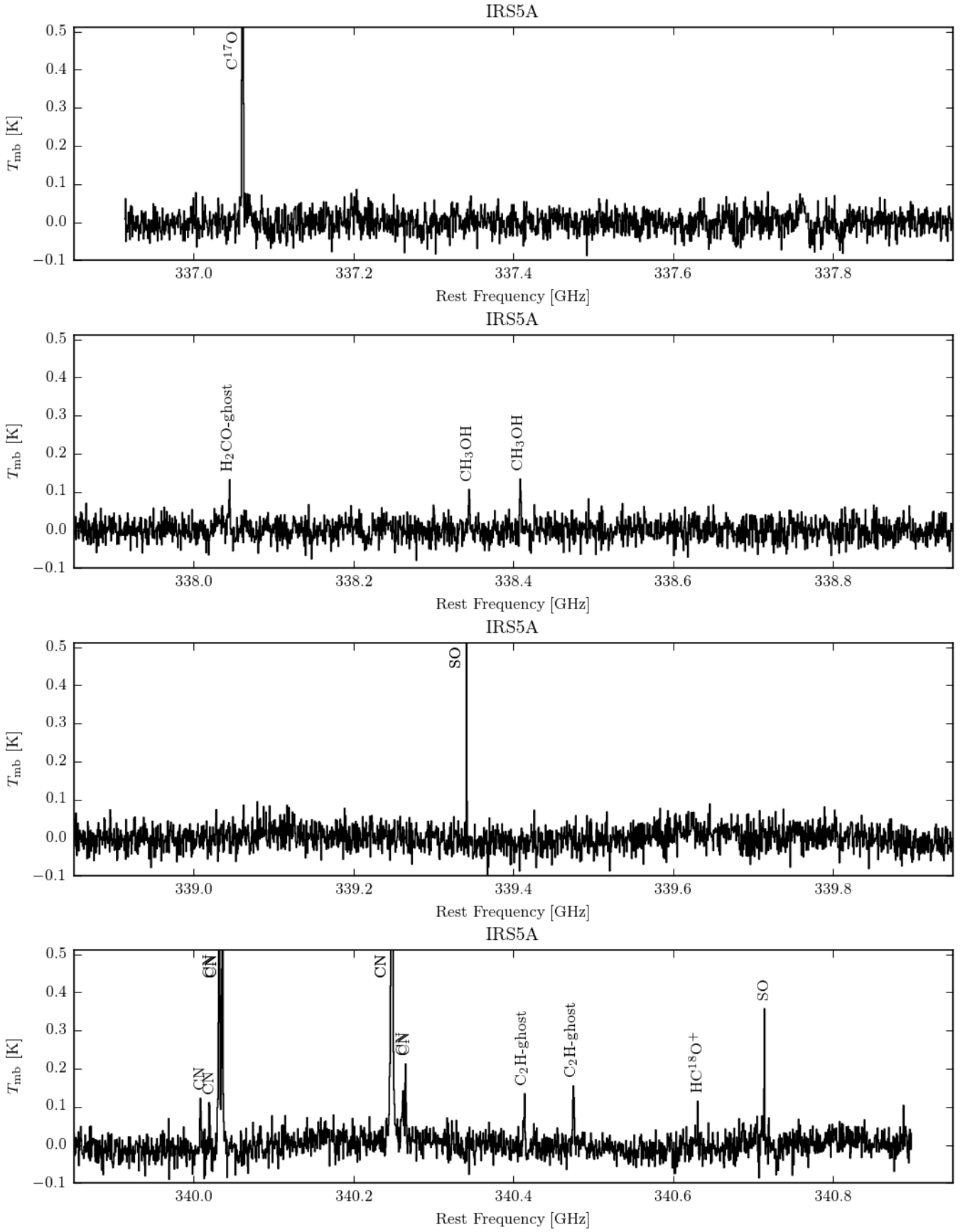


Fig. D.16. 0.9 mm spectrum of IRS5A, smoothed by a factor 8, corresponding to a channel width of 0.6 km s^{-1} .

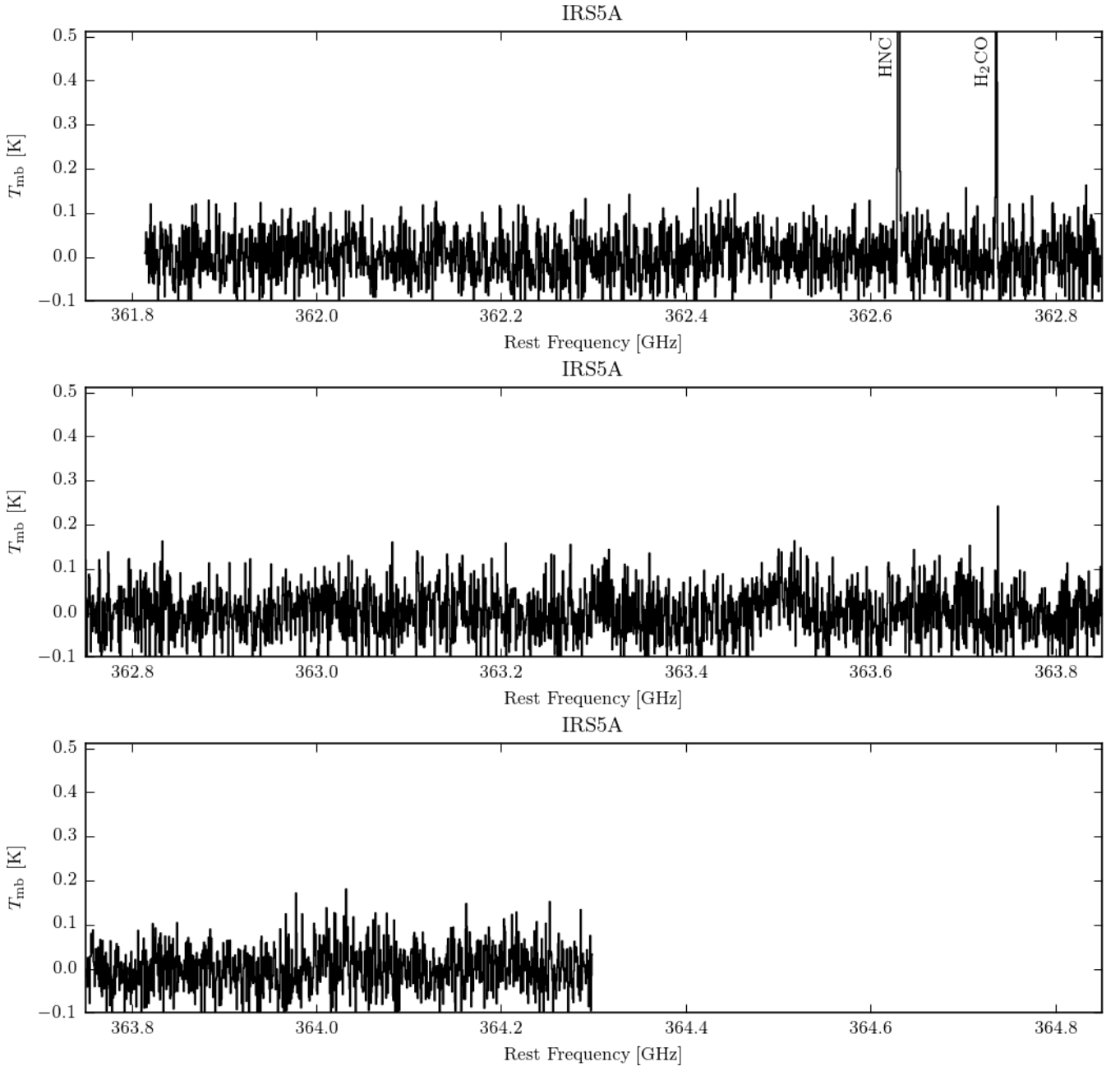


Fig. D.17. 0.8 mm spectrum of IRS5A, smoothed by a factor 8, corresponding to a channel width of 0.5 km s^{-1} .

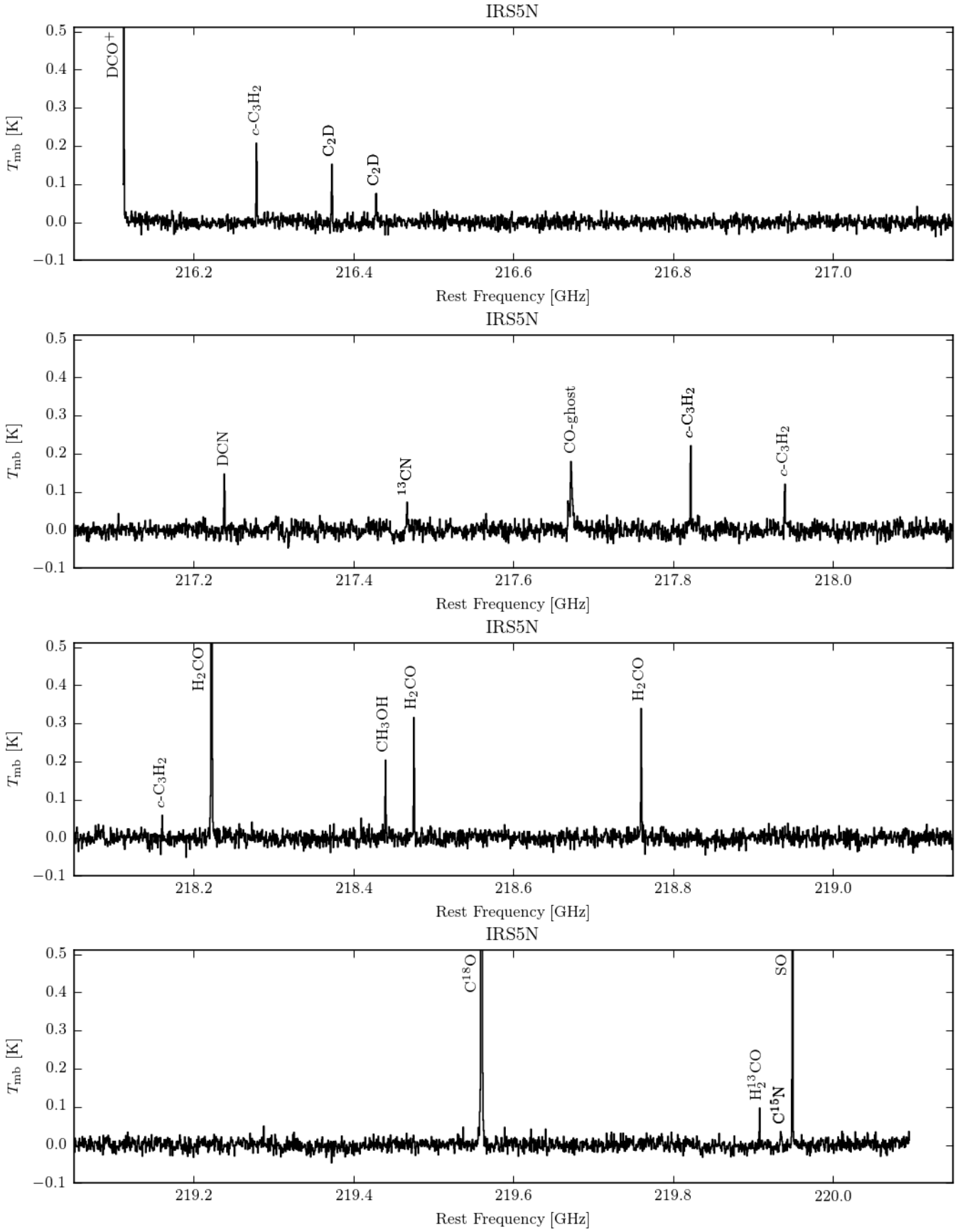


Fig. D.18. 1.4 mm spectrum of IRS5N, smoothed by a factor 8, corresponding to a channel width of 0.8 km s^{-1} .

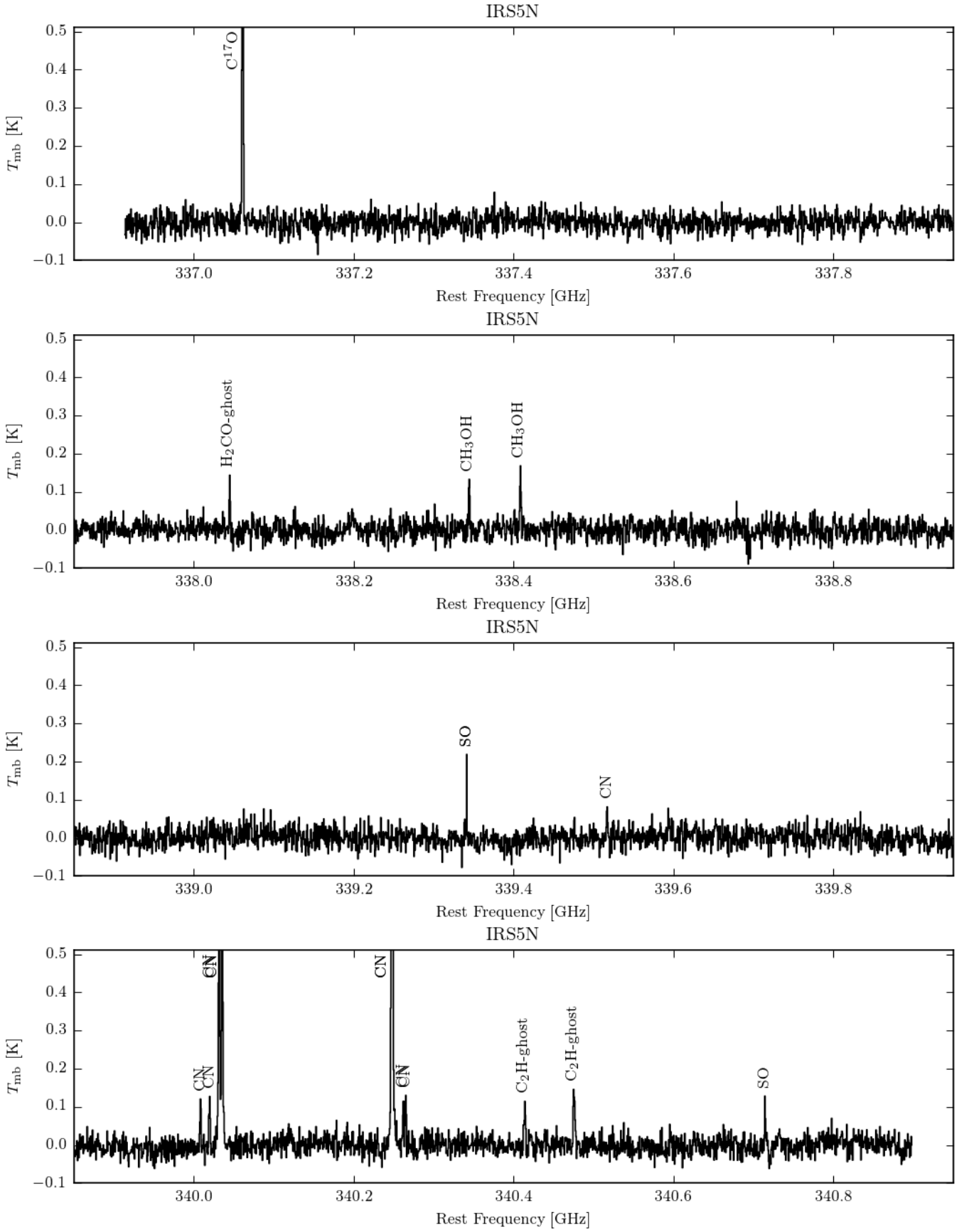


Fig. D.19. 0.9 mm spectrum of IRS5N, smoothed by a factor 8, corresponding to a channel width of 0.6 km s^{-1} .

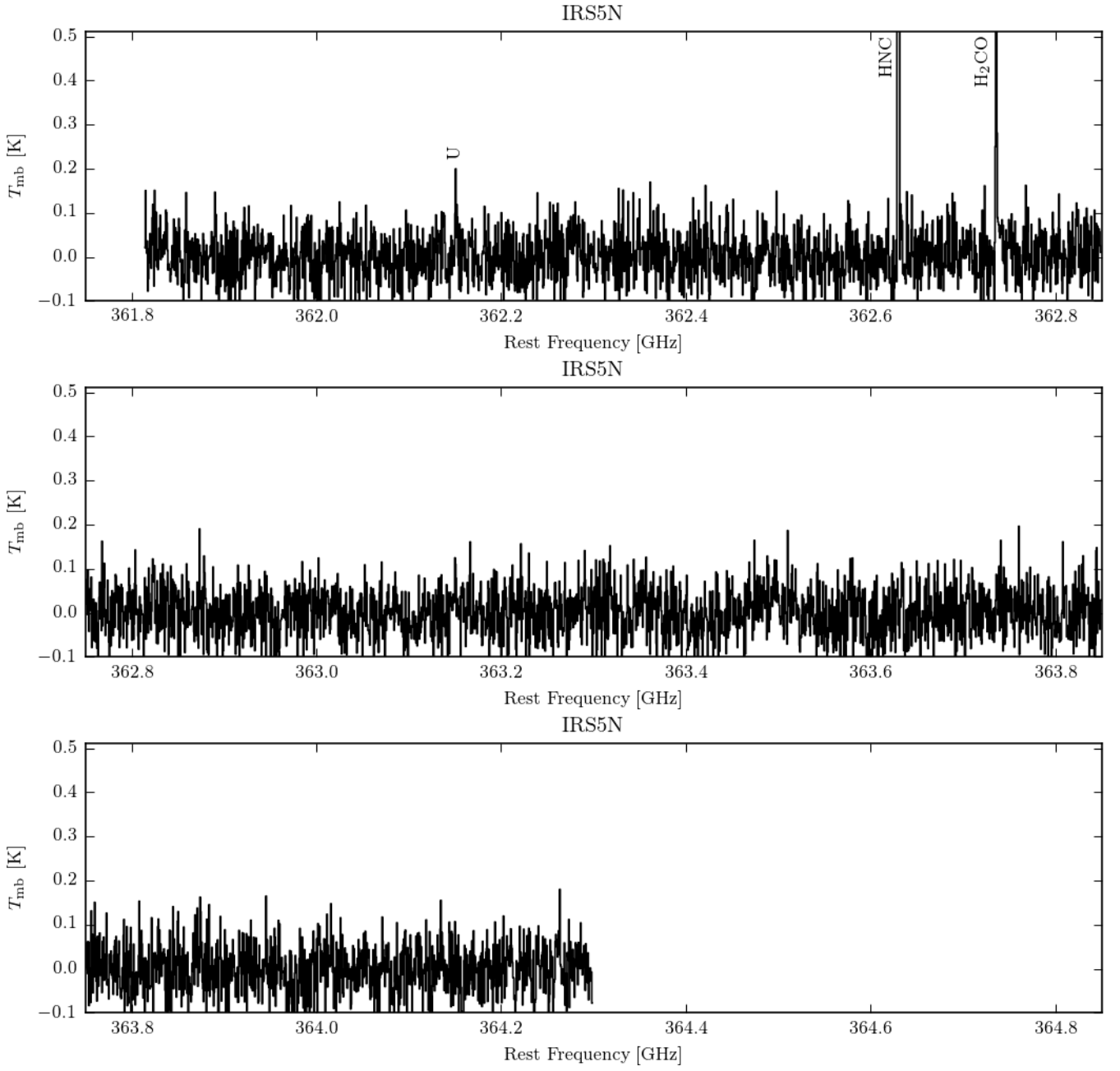


Fig. D.20. 0.8 mm spectrum of IRS5N, smoothed by a factor 8, corresponding to a channel width of 0.5 km s^{-1} .

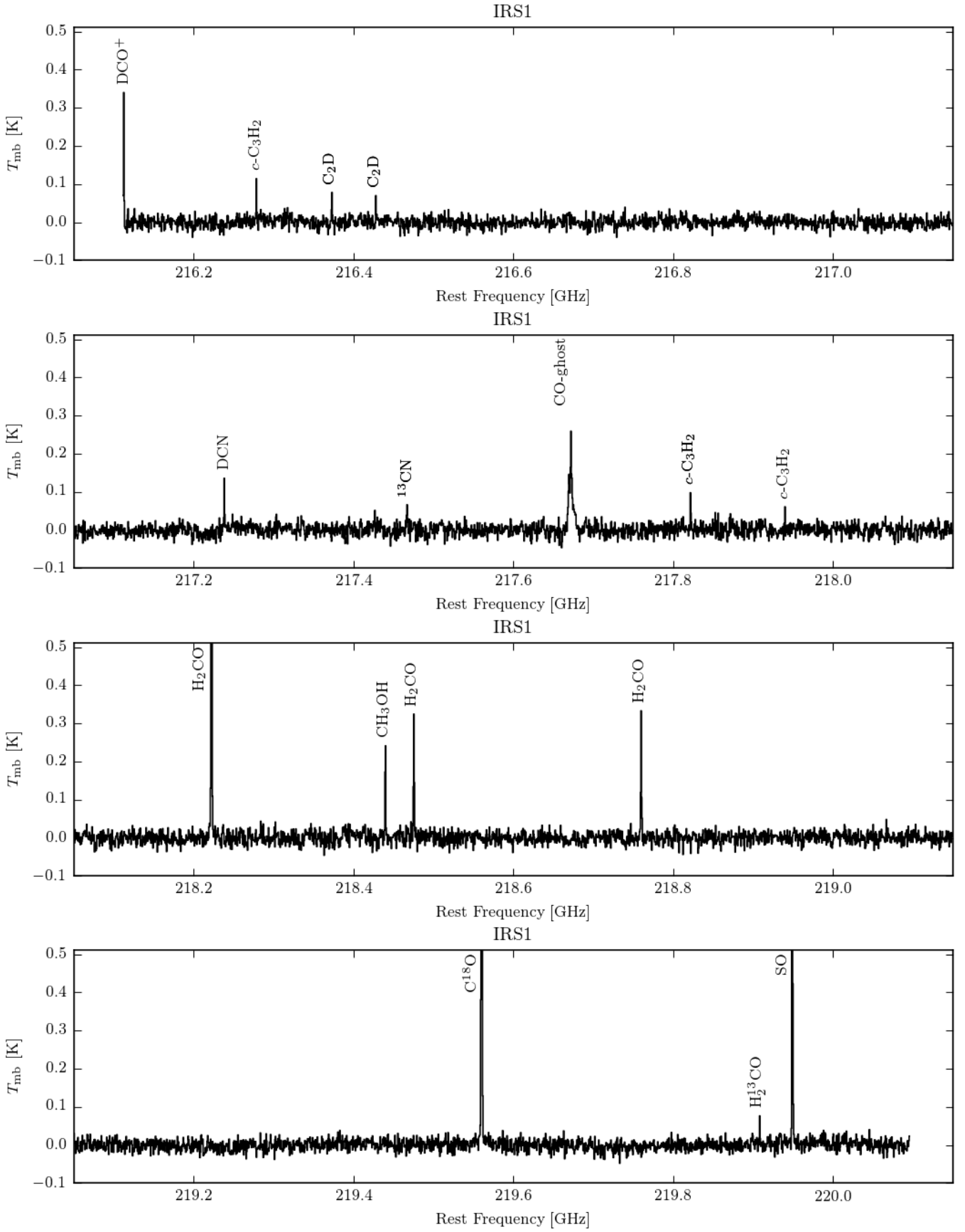


Fig. D.21. 1.4 mm spectrum of IRS1, smoothed by a factor 8, corresponding to a channel width of 0.8 km s^{-1} .

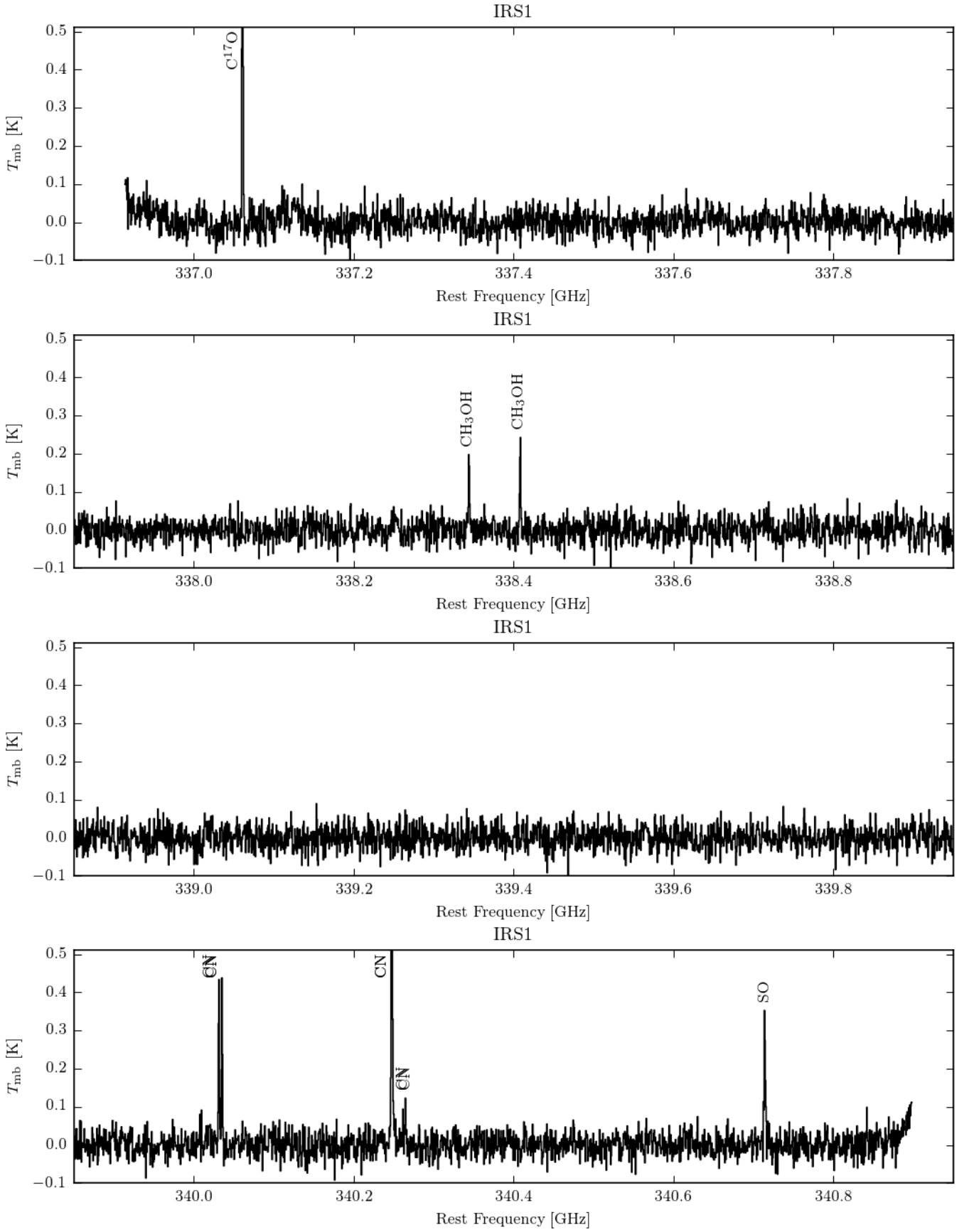


Fig. D.22. 0.9 mm spectrum of IRS1, smoothed by a factor 8, corresponding to a channel width of 0.6 km s^{-1} .

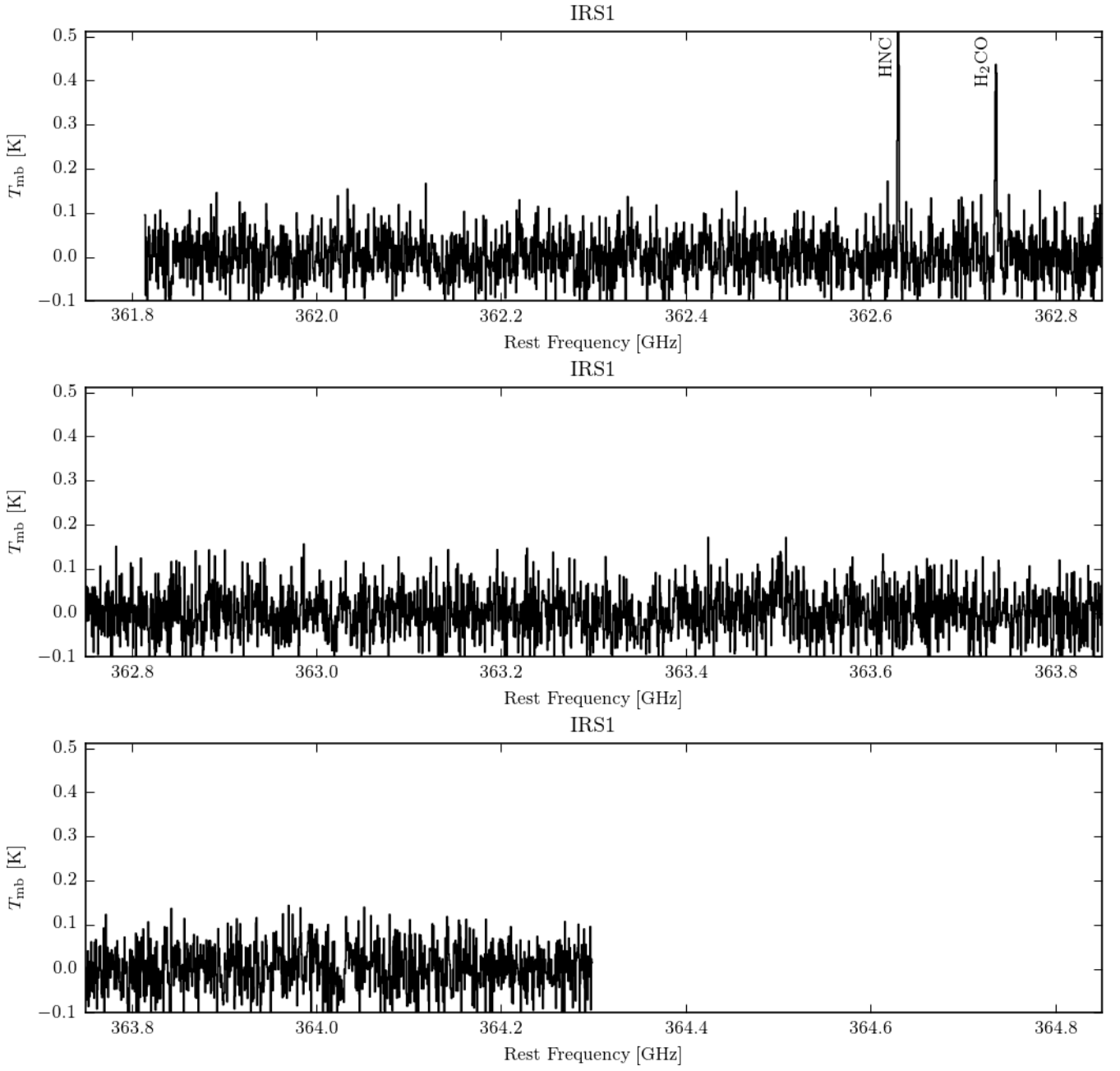


Fig. D.23. 0.8 mm spectrum of IRS1, smoothed by a factor 8, corresponding to a channel width of 0.5 km s^{-1} .

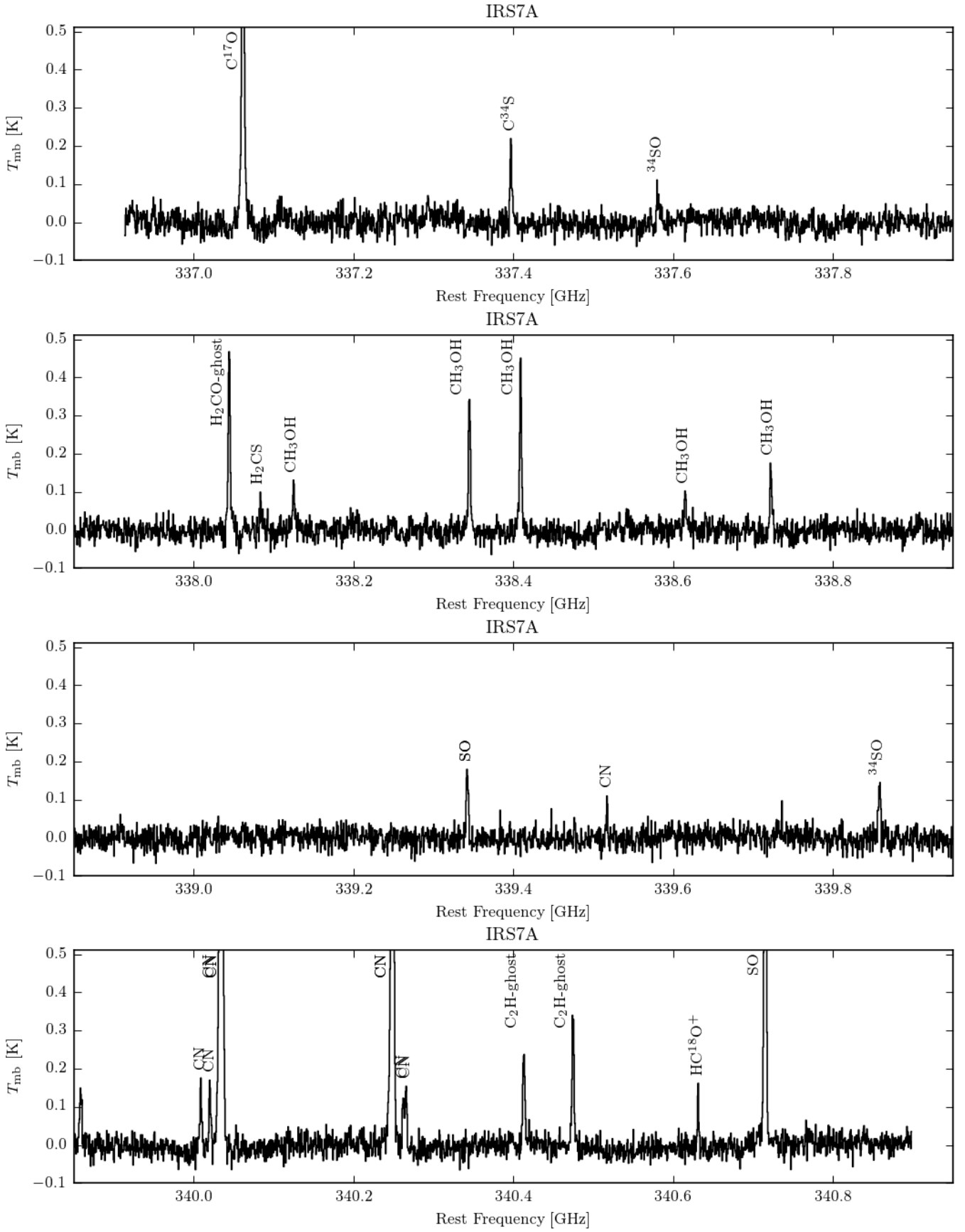


Fig. D.24. 0.9 mm spectrum of IRS7A, smoothed by a factor 8, corresponding to a channel width of 0.6 km s^{-1} .

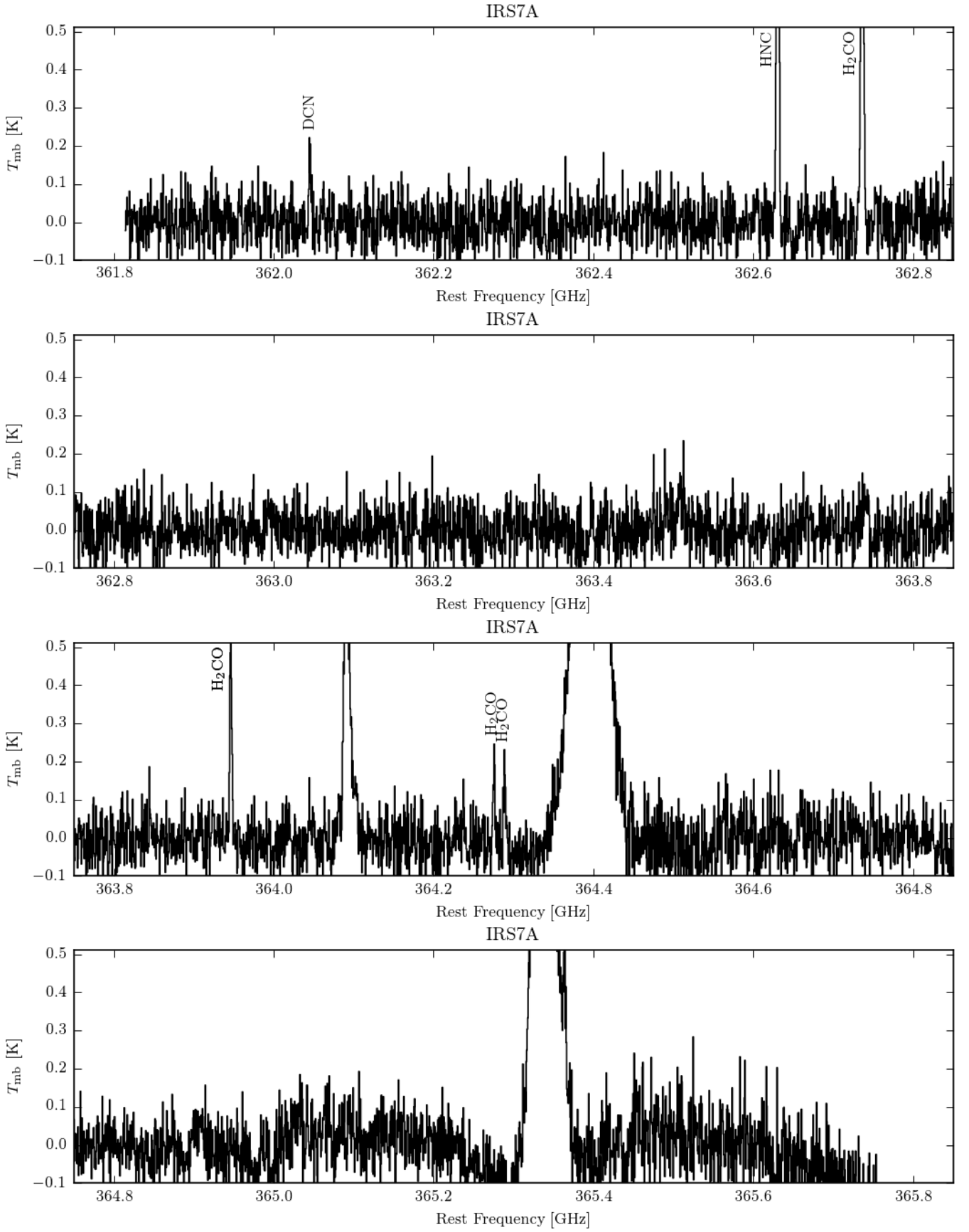


Fig. D.25. 0.8 mm spectrum of IRS7A, smoothed by a factor 8, corresponding to a channel width of 0.5 km s^{-1} . Strong atmospheric lines are visible at 364.1 GHz, 364.4 GHz, and 365.3 GHz.

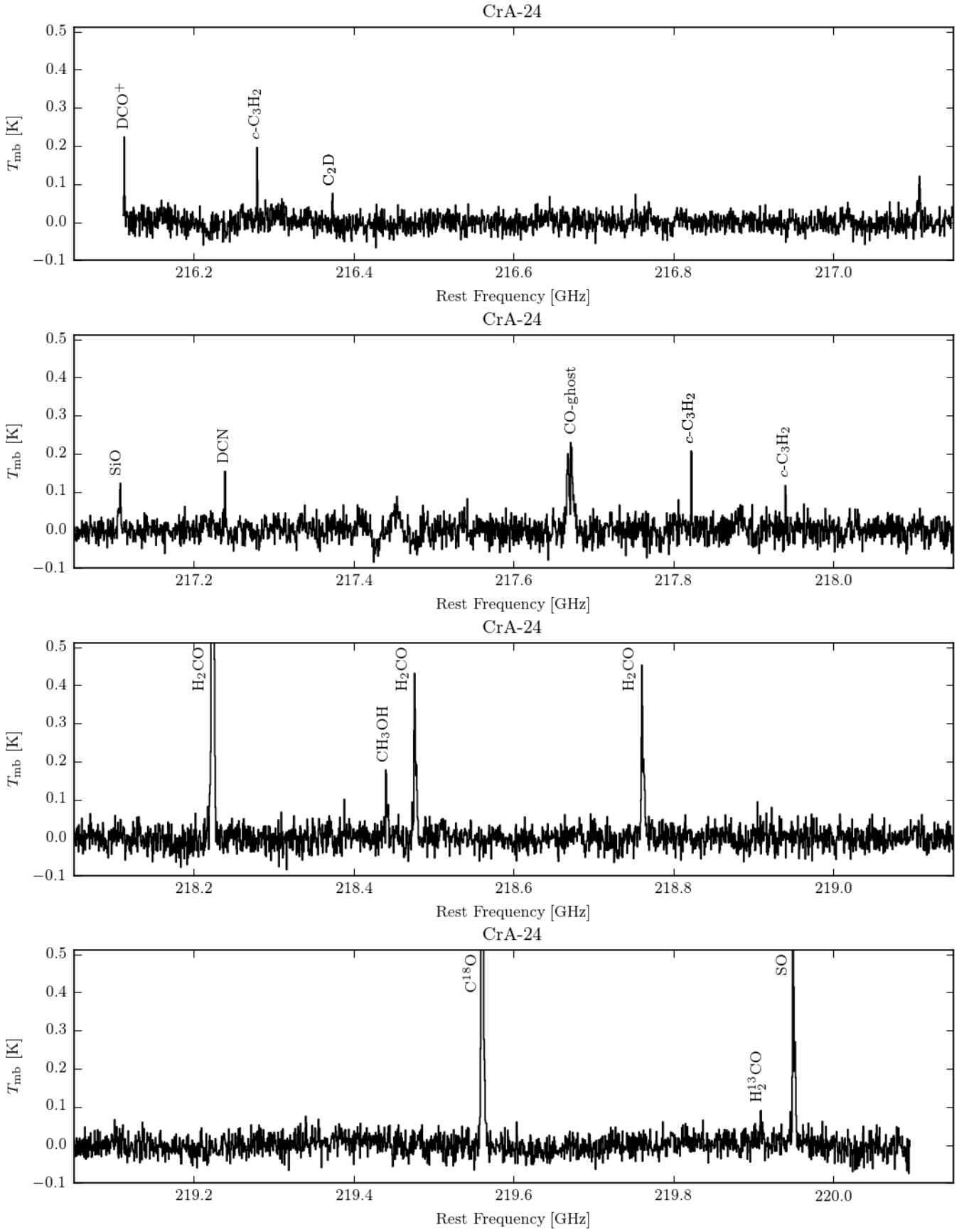


Fig. D.26. 1.4 mm spectrum of CrA-24, smoothed by a factor 8, corresponding to a channel width of 0.8 km s^{-1} . Atmospheric line at 217.7 GHz.

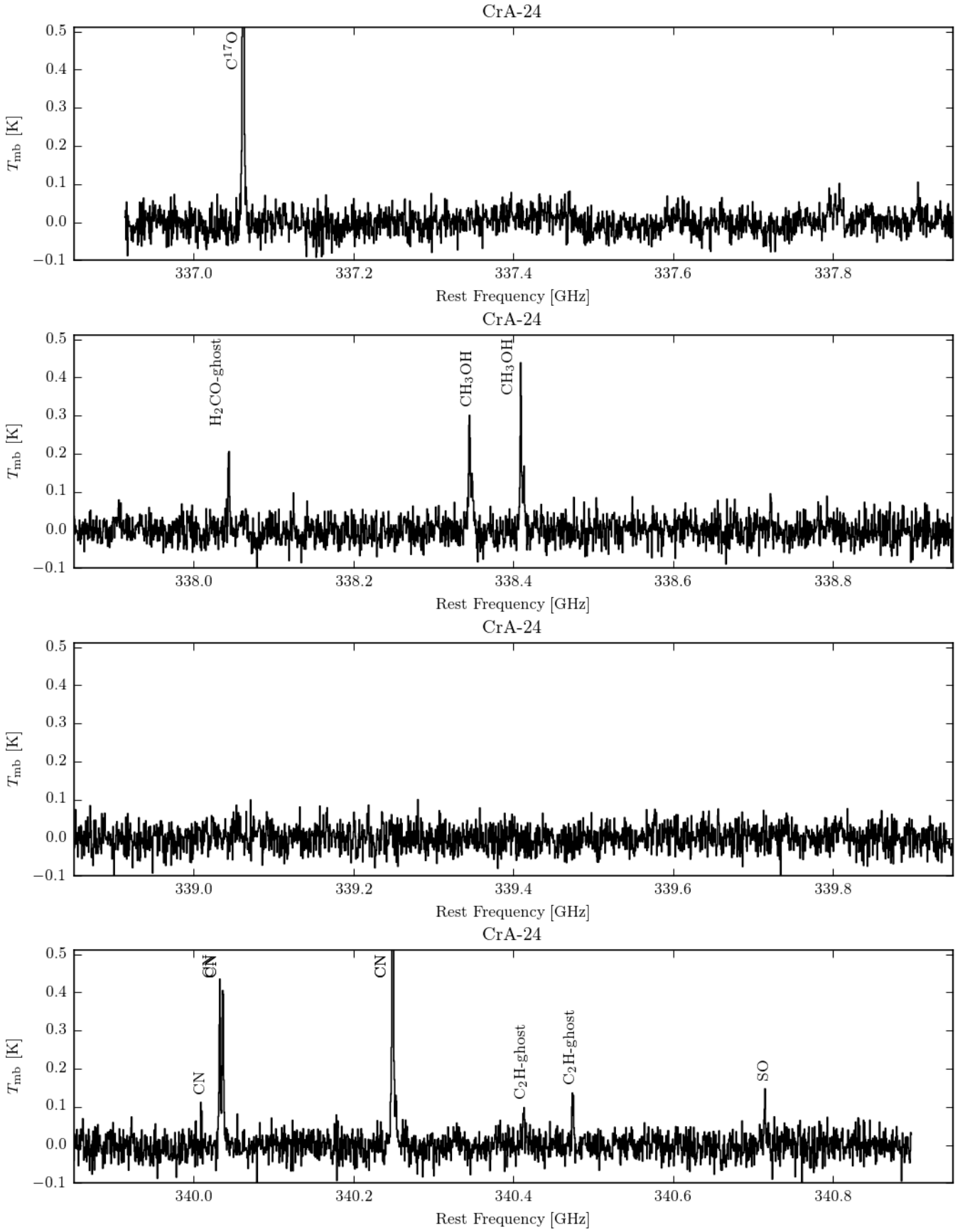


Fig. D.27. 0.9 mm spectrum of CrA-24, smoothed by a factor 8, corresponding to a channel width of 0.6 km s^{-1} .

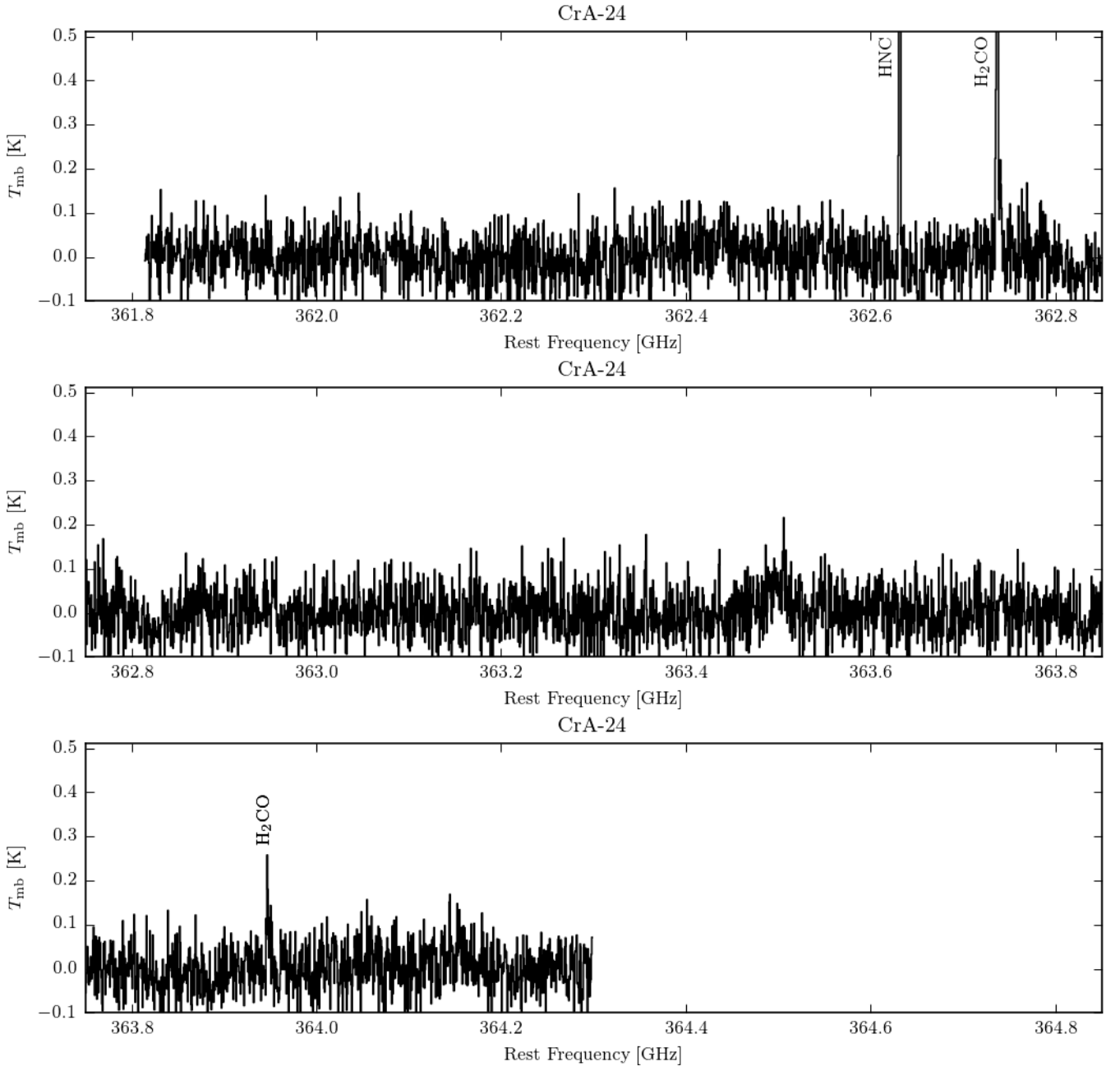


Fig. D.28. 0.8 mm spectrum of CrA-24, smoothed by a factor 8, corresponding to a channel width of 0.5 km s^{-1} .

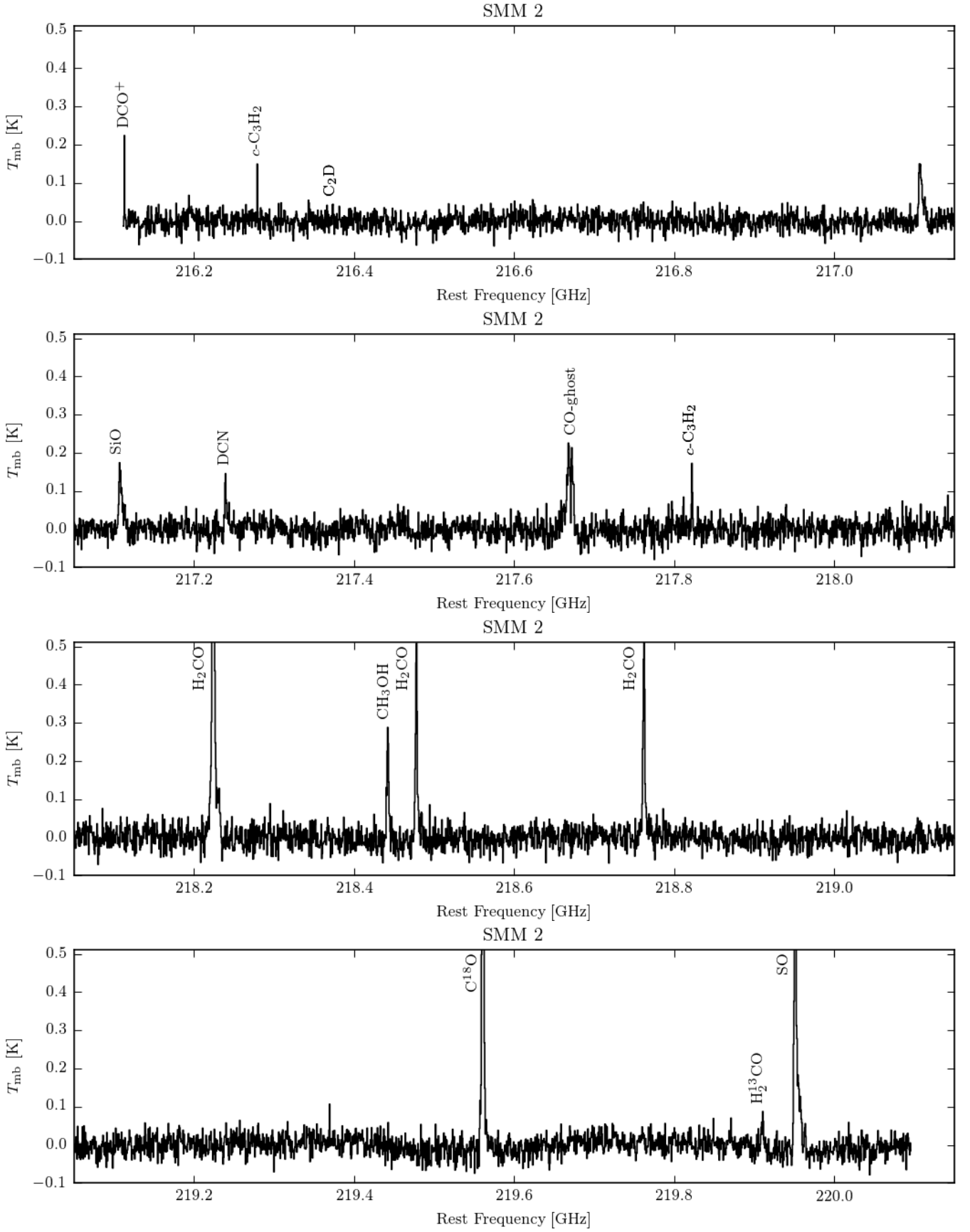


Fig. D.29. 1.4 mm spectrum of SMM 2, smoothed by a factor 8, corresponding to a channel width of 0.8 km s^{-1} .

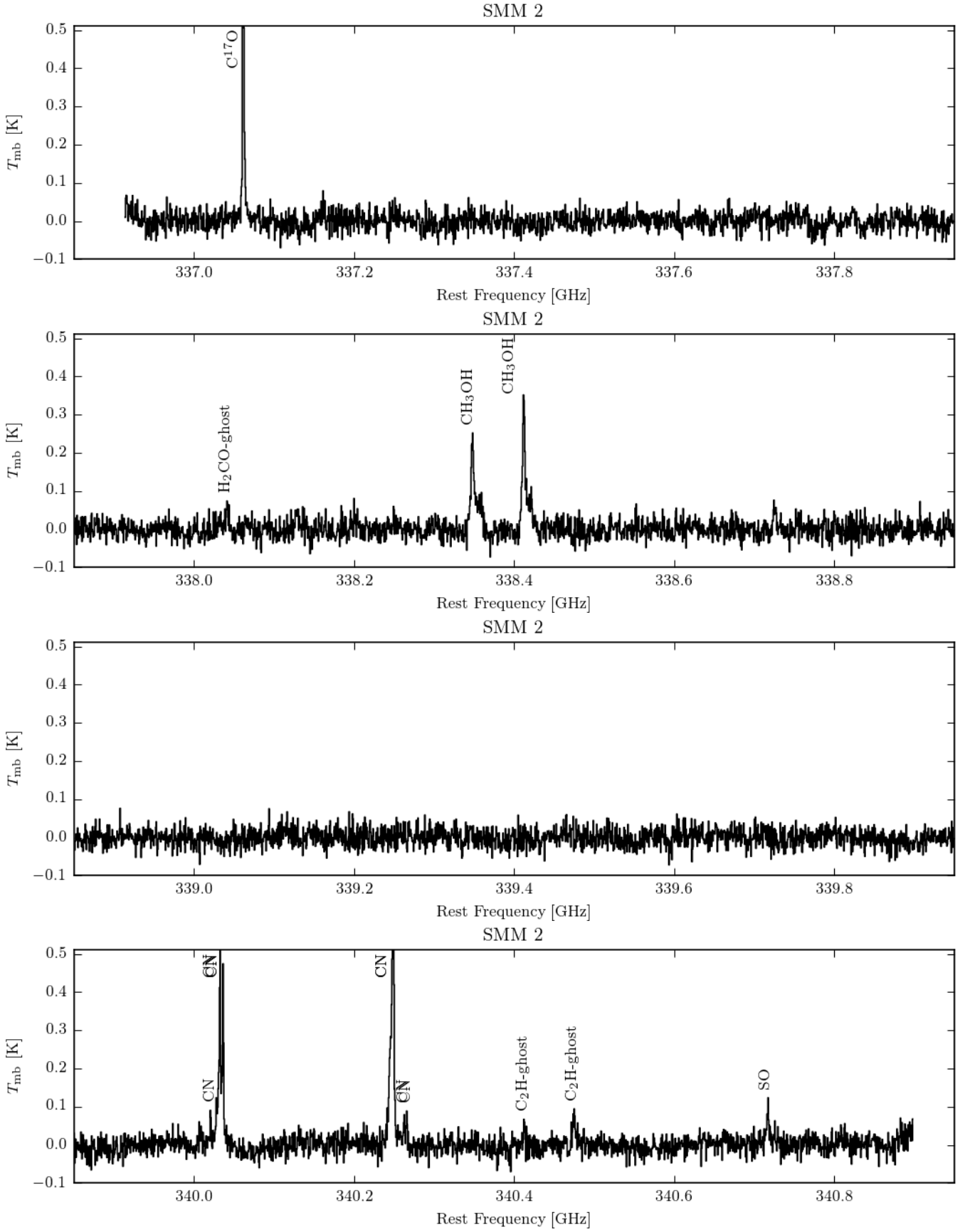


Fig. D.30. 0.9 mm spectrum of SMM 2, smoothed by a factor 8, corresponding to a channel width of 0.6 km s^{-1} .

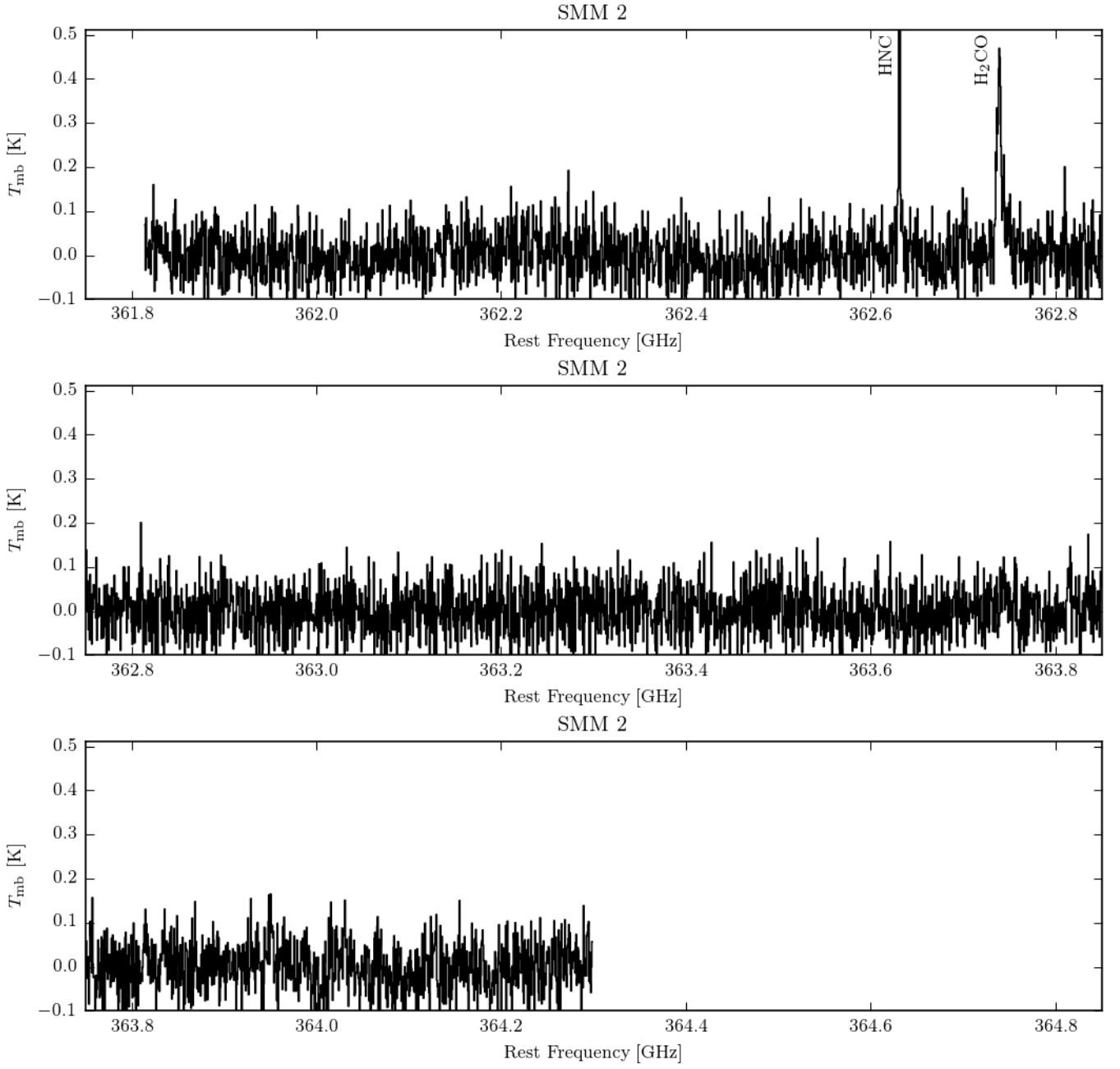


Fig. D.31. 0.8 mm spectrum of SMM 2, smoothed by a factor 8, corresponding to a channel width of 0.5 km s^{-1} .

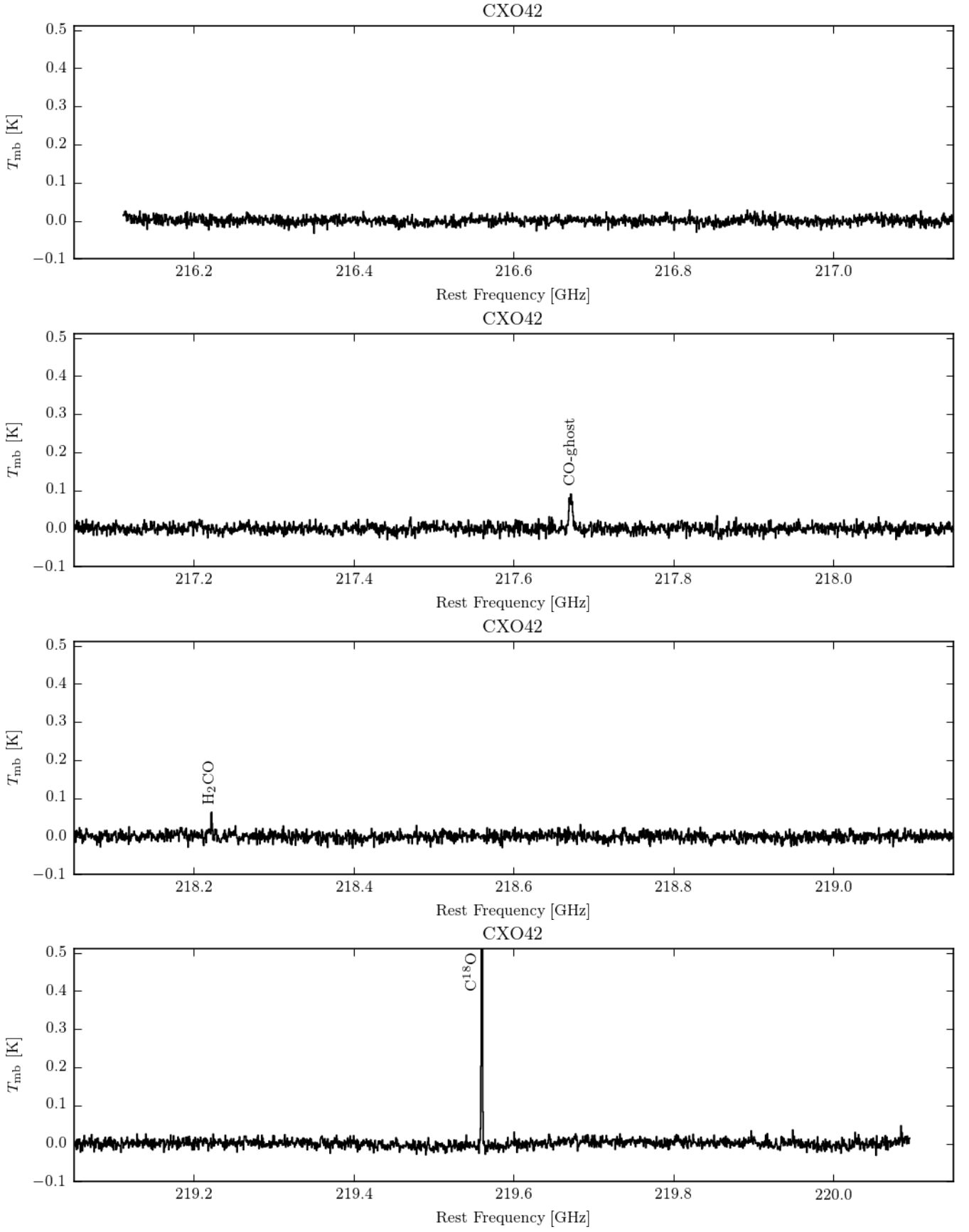


Fig. D.32. 1.4 mm spectrum of CXO42, smoothed by a factor 8, corresponding to a channel width of 0.8 km s⁻¹.

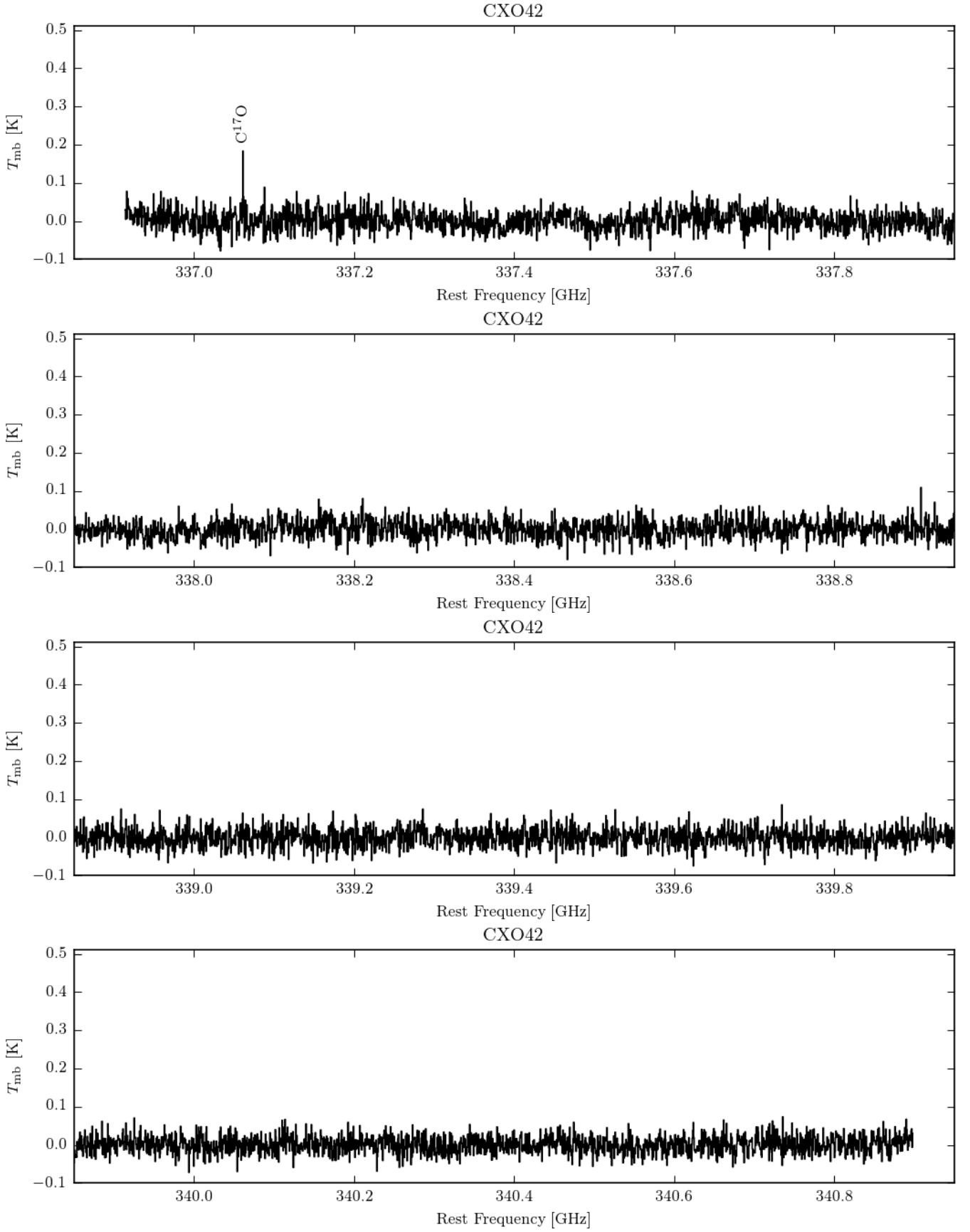


Fig. D.33. 0.9 mm spectrum of CXO42, smoothed by a factor 8, corresponding to a channel width of 0.6 km s^{-1} .

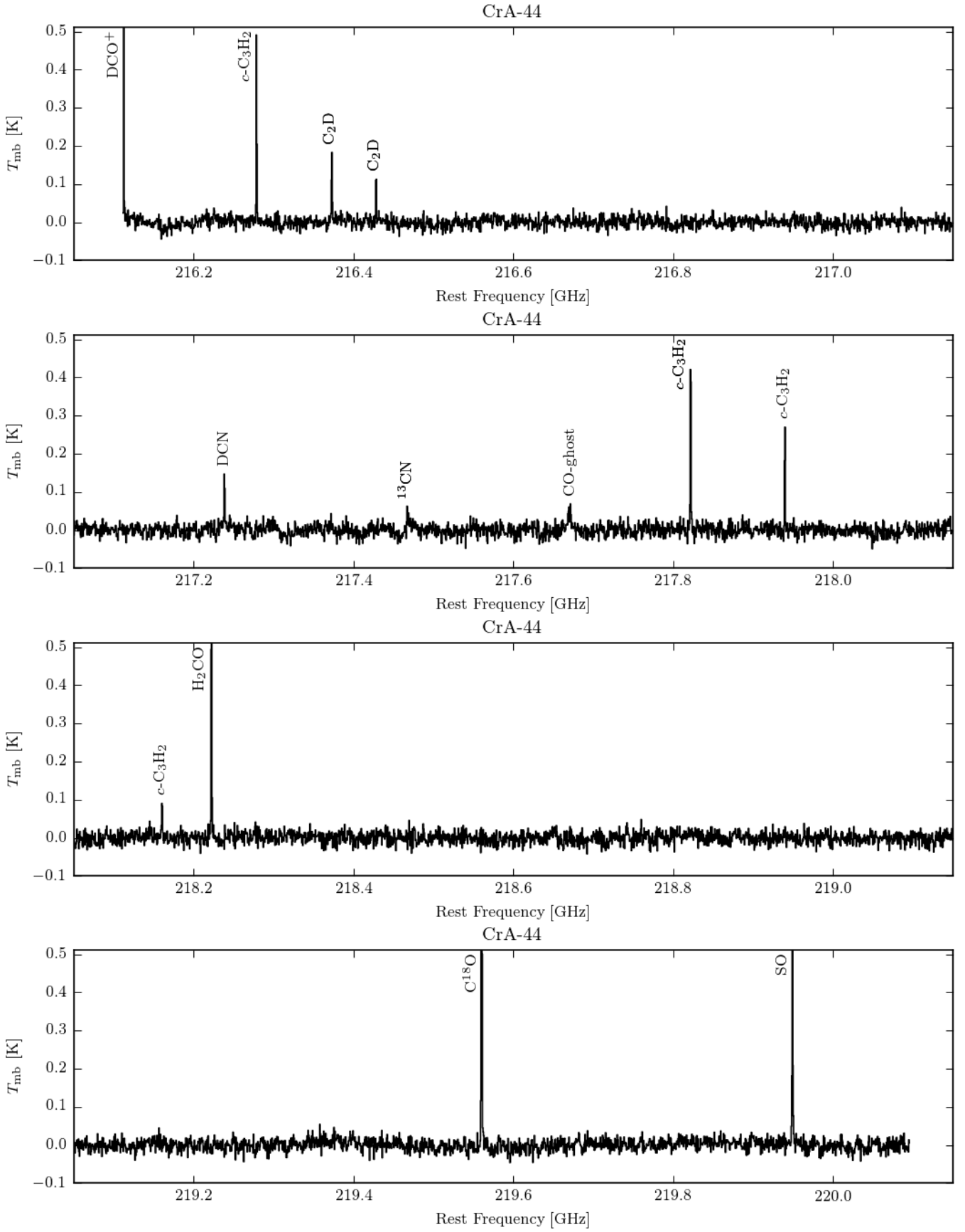


Fig. D.34. 1.4 mm spectrum of CrA-44, smoothed by a factor 8, corresponding to a channel width of 0.8 km s^{-1} .

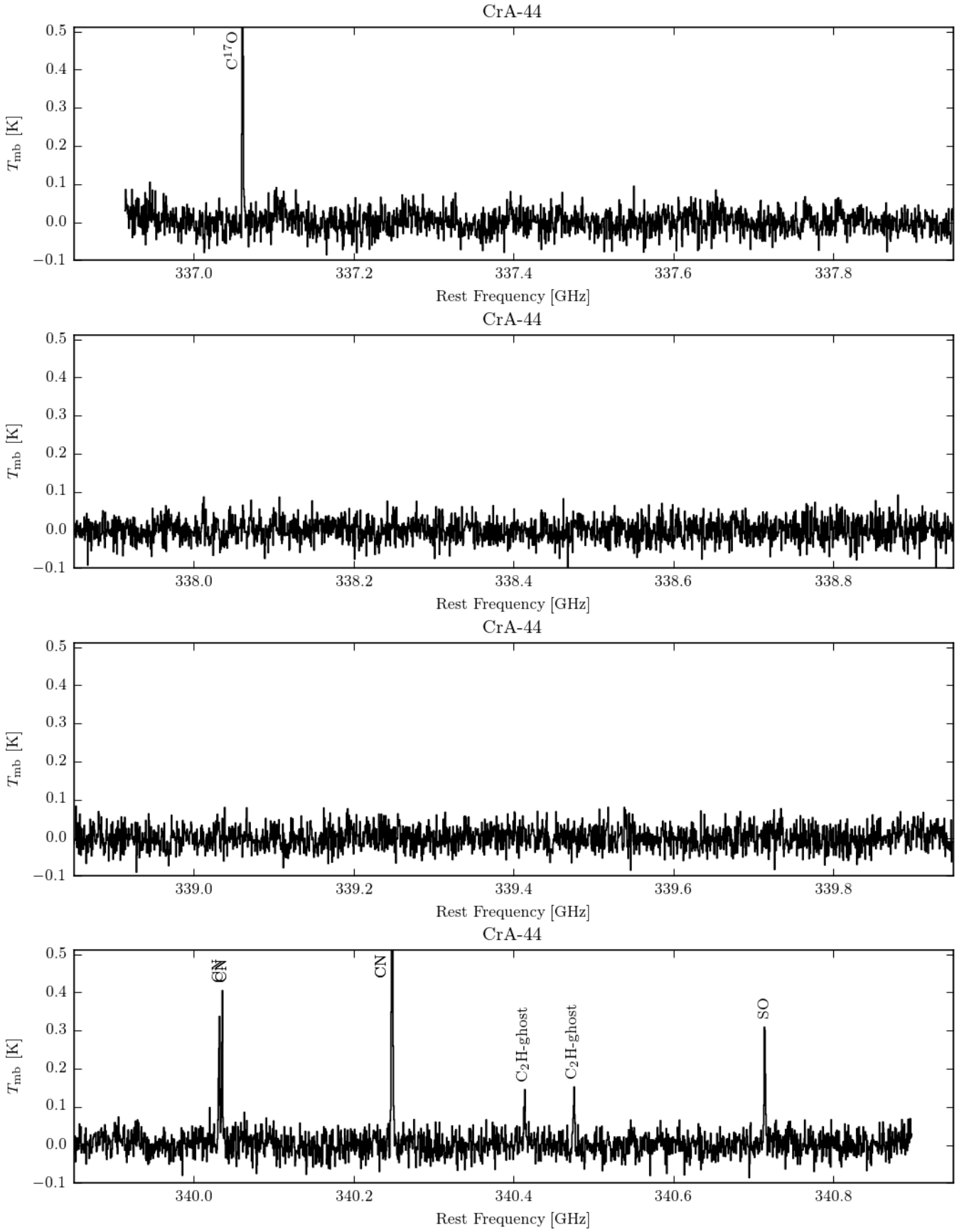


Fig. D.35. 0.9 mm spectrum of CrA-44, smoothed by a factor 8, corresponding to a channel width of 0.6 km s^{-1} .

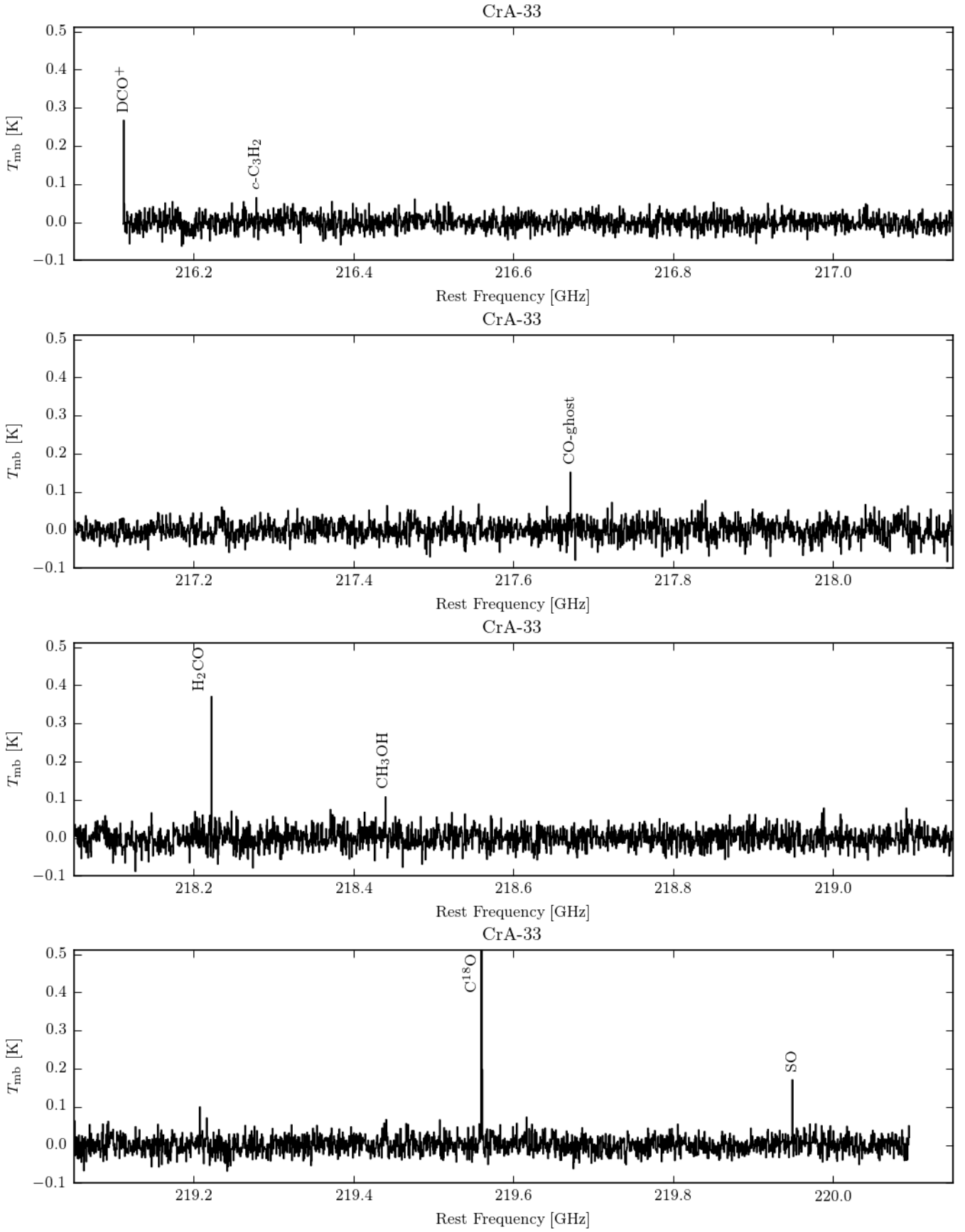


Fig. D.36. 1.4 mm spectrum of CrA-33, smoothed by a factor 8, corresponding to a channel width of 0.8 km s^{-1} .

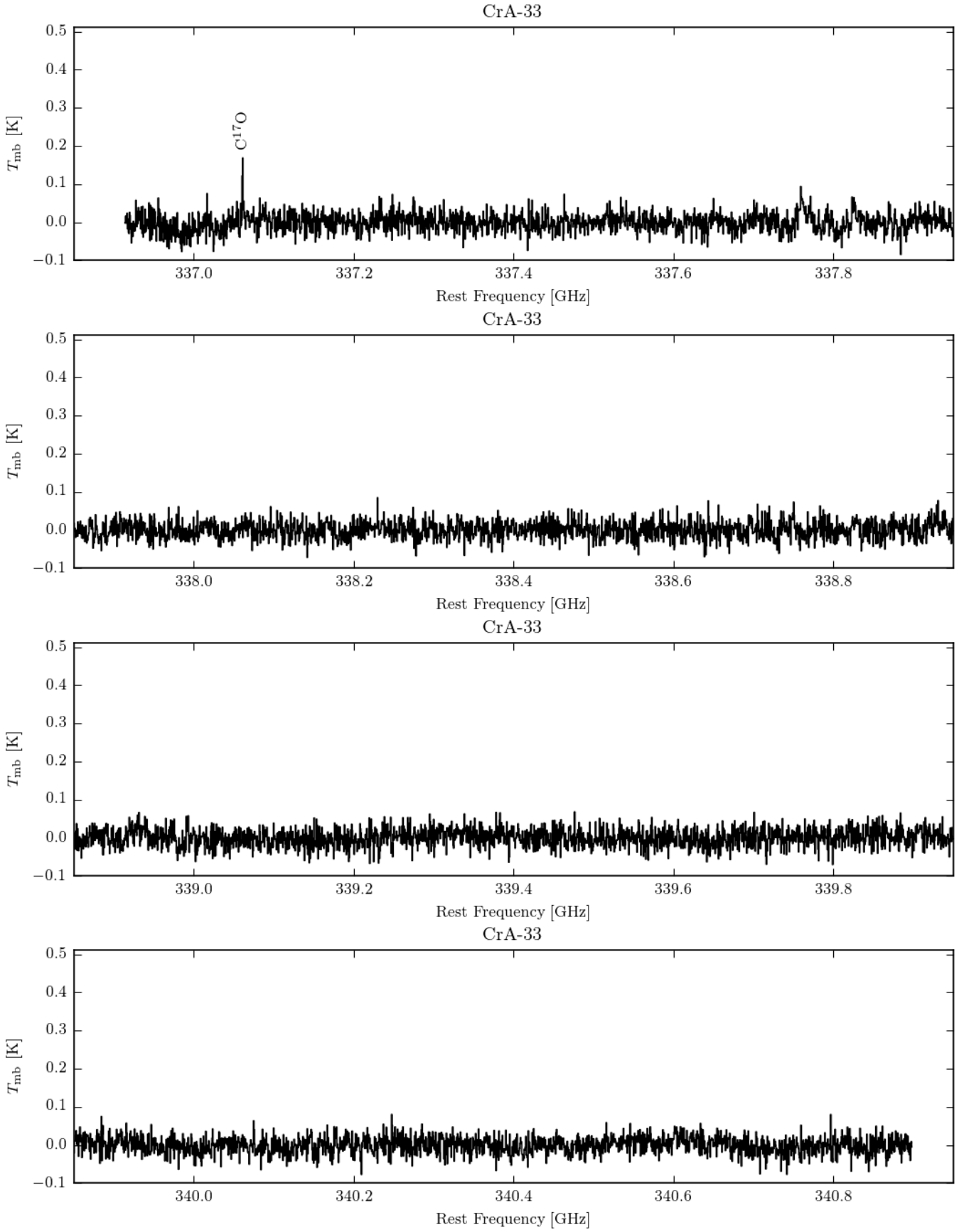


Fig. D.37. 0.9 mm spectrum of CrA-33, smoothed by a factor 8, corresponding to a channel width of 0.6 km s^{-1} .

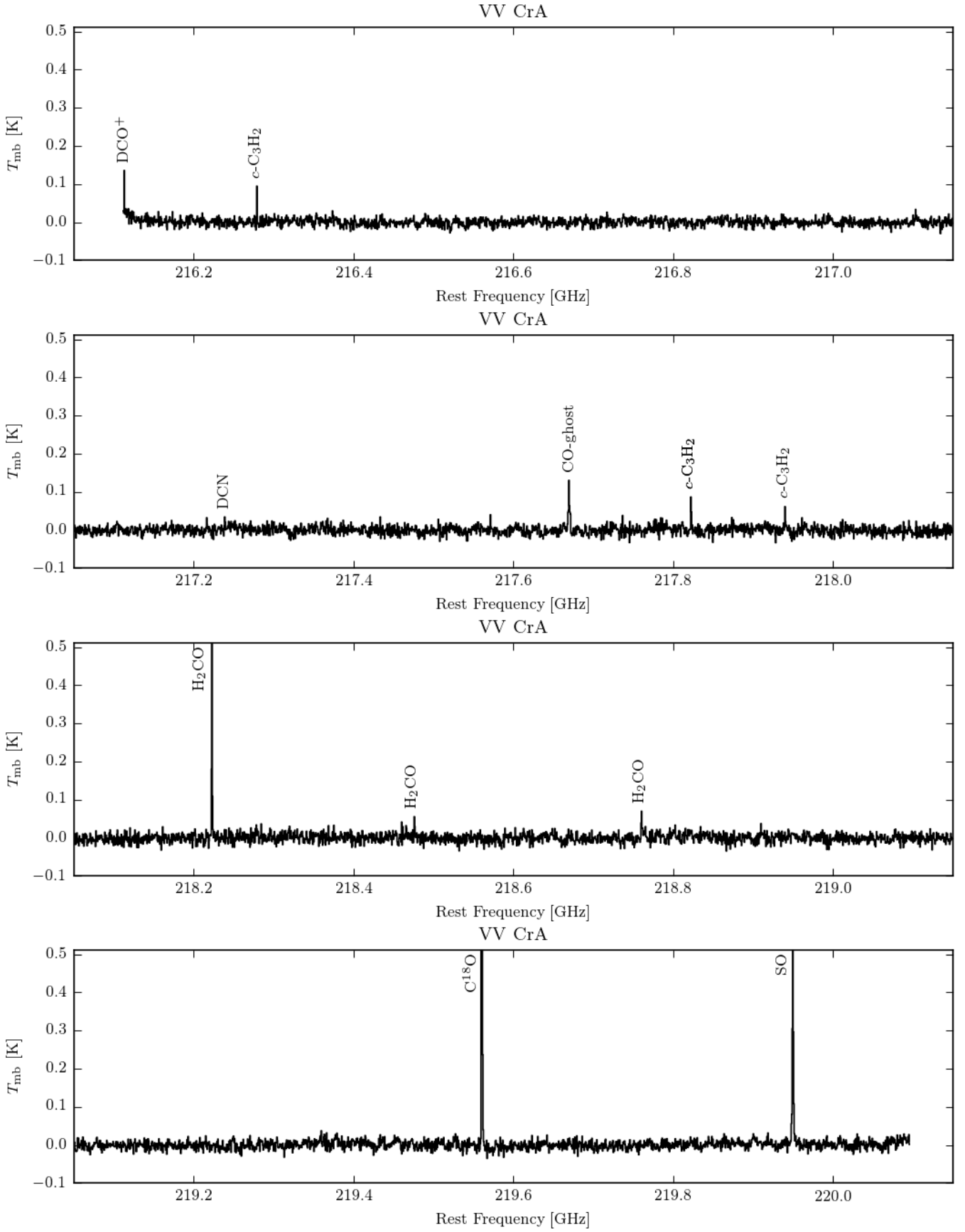


Fig. D.38. 1.4 mm spectrum of VV CrA, smoothed by a factor 8, corresponding to a channel width of 0.8 km s^{-1} .

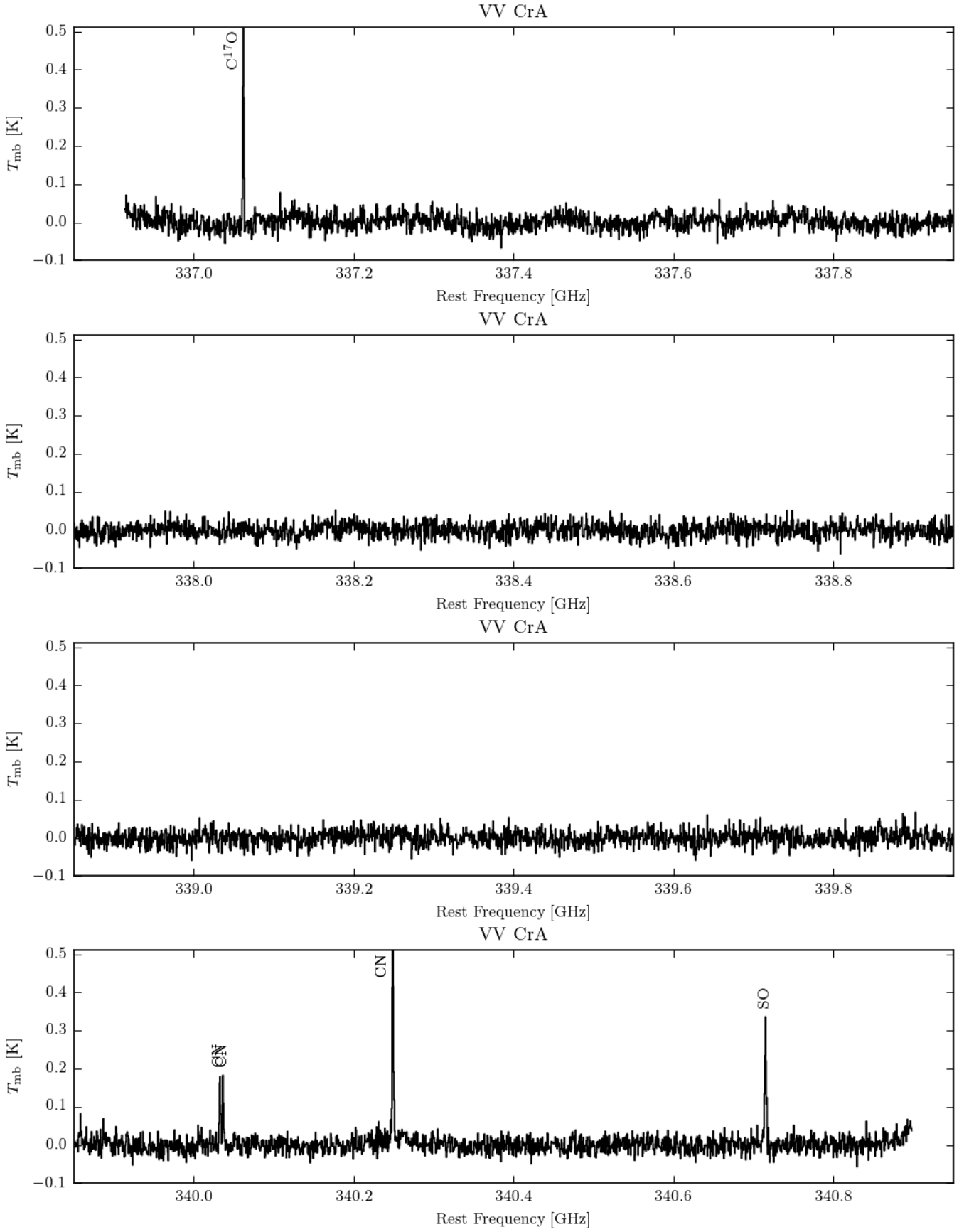


Fig. D.39. 0.9 mm spectrum of VV CrA, smoothed by a factor 8, corresponding to a channel width of 0.6 km s^{-1} .

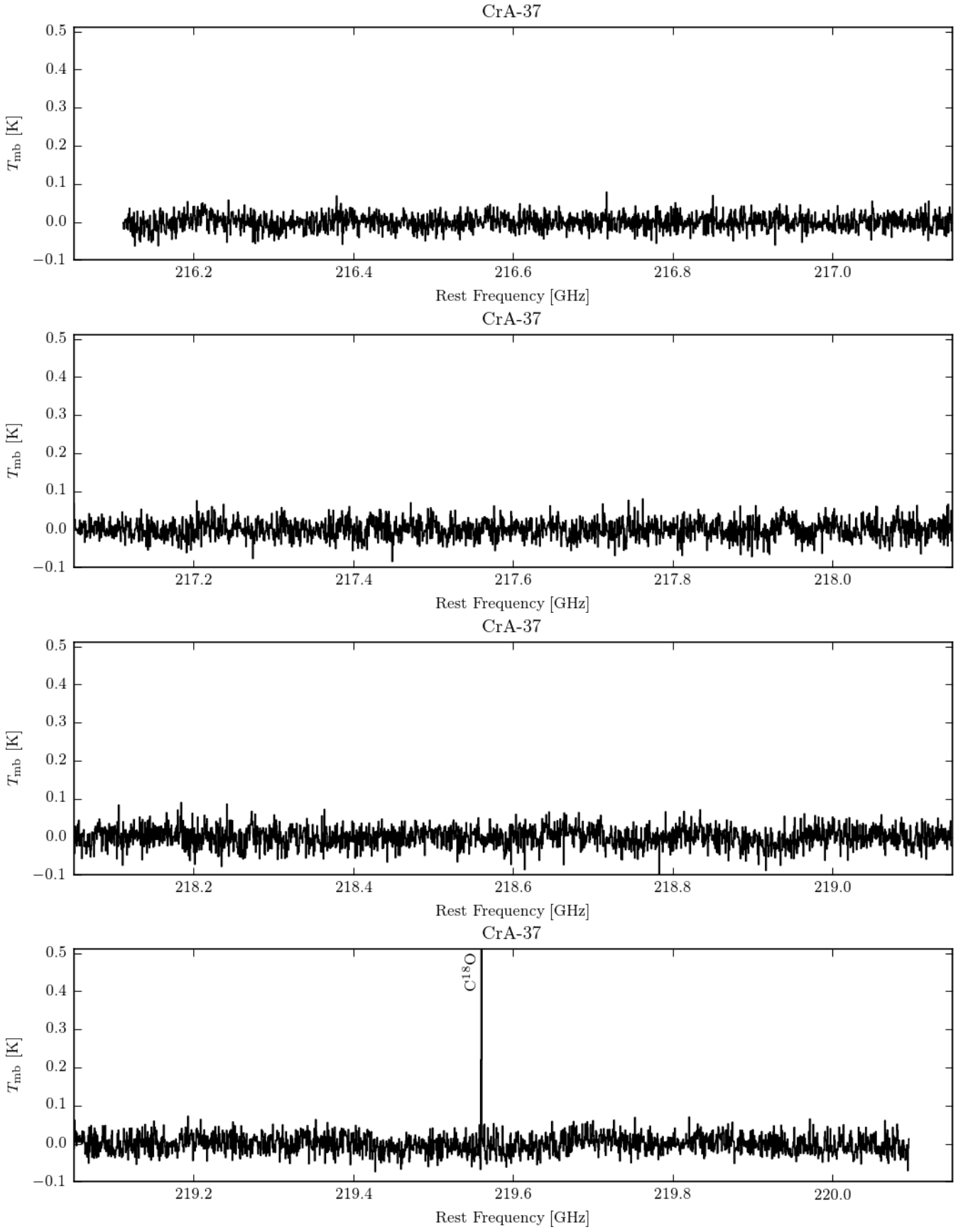


Fig. D.40. 1.4 mm spectrum of CrA-37, smoothed by a factor 8, corresponding to a channel width of 0.8 km s^{-1} .

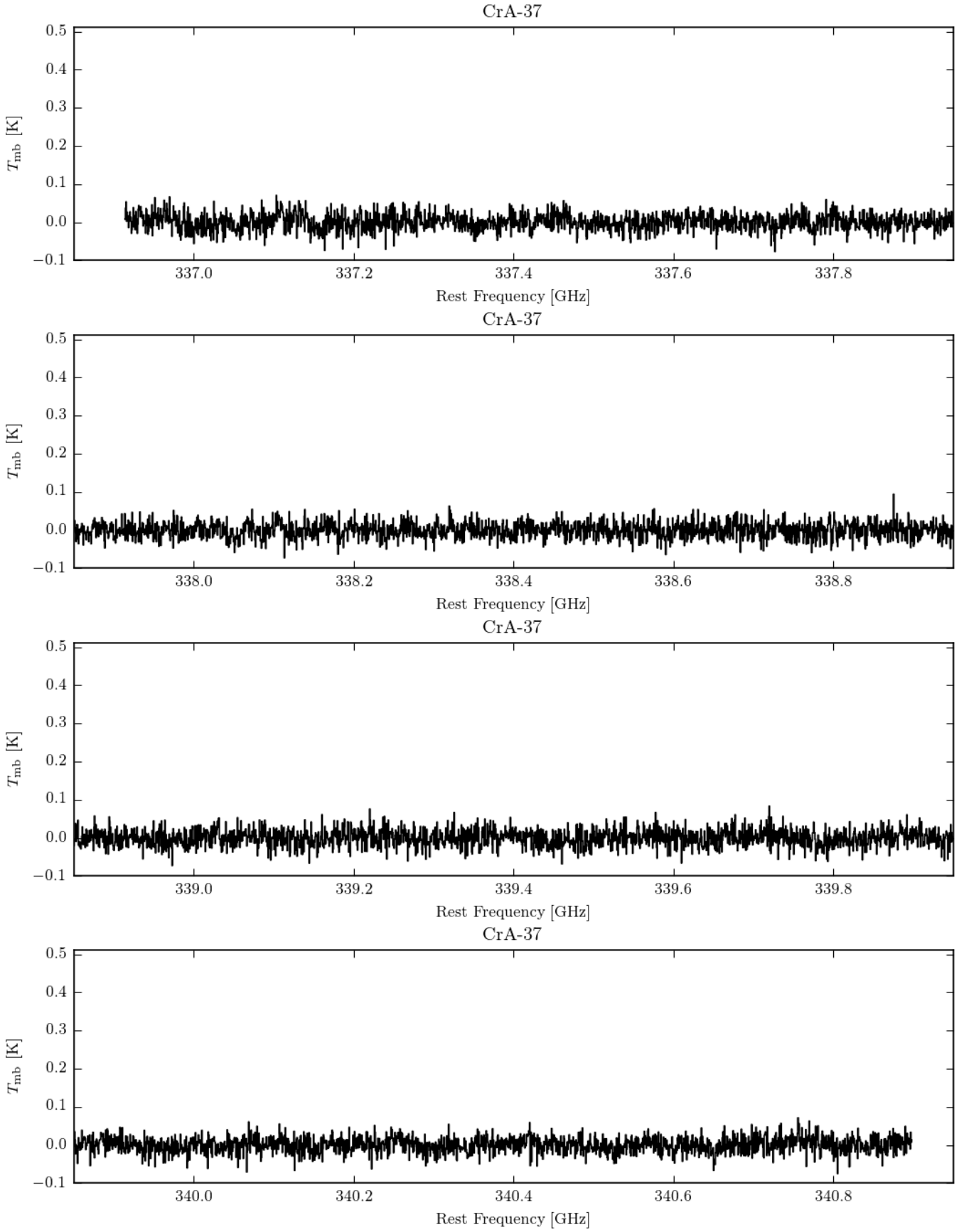


Fig. D.41. 0.9 mm spectrum of CrA-37, smoothed by a factor 8, corresponding to a channel width of 0.6 km s^{-1} .

Appendix E: Unidentified spectral lines

We here present our attempts to identify all U lines detected towards IRS7B: The faint line at 229.7760 GHz (assuming $v_{\text{LSR}} = 5.7 \text{ km s}^{-1}$) could be the CH_3CHO line at 229.7750 GHz, but that would give this line a $v_{\text{LSR}} = 4.5 \text{ km s}^{-1}$, which is 1.2 km s^{-1} lower than the median LSR velocity and 0.5 km s^{-1} lower than any other line, including the more certain CH_3CHO lines (also if taking the JPL uncertainty of 50 kHz on the measured laboratory line frequency into account). The line at 225.160 GHz coincides with a CH_3SH line, but this is not the strongest line expected from this species in the studied frequency range. The 237.998 GHz line is consistent with a $c\text{-H}^{13}\text{CCCH}$ line, but if this is a true detection, the $c\text{-H}^{13}\text{CCCH}$ abundance would be of the same order as the $c\text{-C}_3\text{H}_2$ abundance, which is very unlikely. The remaining U lines do not align with any spectral lines found in Splatalogue of species expected to be present at this rms level. Two of the detected lines agree with known U lines at 223.756 GHz and 233.456 GHz. As a result of incomplete image-band rejection, a few so-called ghost lines appear at the image frequencies of the strongest spectral lines (CO isotopologue lines and strong H_2CO , CH_3OH , and CN lines). We did not tabulate these ghost lines, but they are labelled in the spectra in Appendix C. For all identified and unidentified lines, the image frequencies were investigated to exclude the possibility that any reported line would be such a ghost line.

Appendix F: Non-LTE models of H_2CO emission

Mangum & Wootten (1993) showed that ratios of H_2CO transitions involving the same J_u -level but from different K -ladders (such as the $3_{03} \rightarrow 2_{02}/3_{22} \rightarrow 2_{21}$ and $5_{05} \rightarrow 4_{04}/5_{24} \rightarrow 4_{23}$ ratios) are excellent tracers of the kinetic temperature of the gas because they only operate through collisional excitation. However, at densities $n \lesssim 10^8 \text{ cm}^{-3}$, the different J_u -levels are not fully thermalised, which means that ratios of transitions involving different J_u -levels (such as $3_{03} \rightarrow 2_{02}/5_{05} \rightarrow 4_{04}$) are sensitive not only to the temperature, but also to the molecular density $n(\text{H}_2)$.

Mangum & Wootten (1993) used LVG models to derive a method for extracting temperature, density, and column density from H_2CO line observations. Jansen (1995) performed RADEX modelling of H_2CO line ratios to show which H_2CO line ratios can be used to trace the kinetic temperature at rather low column densities, investigating certain line ratios at a p- H_2CO column density of $N = 10^{12} \text{ cm}^{-2}$. In Fig. F.1 we show such plots at a p- H_2CO column density $N = 10^{14} \text{ cm}^{-2}$, which agrees better with the properties of the sources in this study. The $3_{03} \rightarrow 2_{02}/5_{05} \rightarrow 4_{04}$ ratio clearly is a particularly poor temperature probe, while the $3_{03} \rightarrow 2_{02}/3_{22} \rightarrow 2_{21}$, $3_{03} \rightarrow 2_{02}/3_{21} \rightarrow 2_{20}$, and $5_{05} \rightarrow 4_{04}/5_{23} \rightarrow 4_{22}$ ratios probe the temperature well at $T \lesssim 50 \text{ K}$ and $n \gtrsim 10^5 \text{ cm}^{-3}$, also at this relatively high column density. We used the p- H_2CO molecular data file from the LAMDA database (Schöier et al. 2005), which uses the collisional rates for p- $\text{H}_2\text{CO}\text{-H}_2$ from Wiesenfeld & Faure (2013). If we instead use the older Green (1991) p- $\text{H}_2\text{CO}\text{-He}$ collisional rates corrected to collisions with H_2 by correctional factors for pressure broadening and relative collision velocities the estimated $n(\text{H}_2)$ values become $\sim 50\%$ higher.

To acquire the H_2CO temperature T , column density N , and the H_2 density n towards the sources where we have measurements of both $J_u = 3$ and $J_u = 5$ transitions, we used the following recipe developed from the method of Mangum & Wootten (1993):

1. Measure the rotational temperatures of the $J_u = 3$ and $J_u = 5$ transitions separately and assume that the kinetic temperature is the weighted average of these two temperatures. If only the $J_u = 3$ transitions can be measured, we use this as the kinetic temperature (and conversely, we use only the $J_u = 5$ temperature in IRS7A, since the $J_u = 3$ transitions were not covered).
2. Use the non-LTE radiative transfer code RADEX (van der Tak et al. 2007) to calculate model line strengths of the $3_{03} \rightarrow 2_{02}$ and $5_{05} \rightarrow 4_{04}$ lines for the kinetic temperature and a grid of n and N (where N is the total H_2CO column density assuming an ortho-to-para ratio of 1.6).
3. On this (n, N) model grid, plot lines corresponding to the measured $3_{03} \rightarrow 2_{02}/5_{05} \rightarrow 4_{04}$ line ratio and the measured $3_{03} \rightarrow 2_{02}$ line strength. The values of n and N are determined from the intersection of these lines (see example in Fig. F.2).

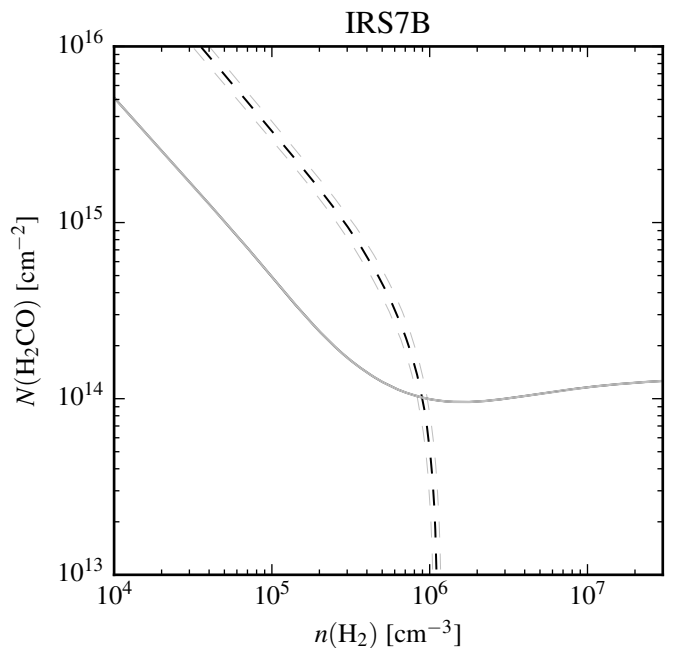


Fig. F.2. RADEX fit for H_2CO in IRS7B, given $T = 40 \text{ K}$ (from the rotational diagram fit of the full IRS7B survey). The solid line shows the measured $3_{03} \rightarrow 2_{02}$ line intensity, and the dashed line is the measured $3_{03} \rightarrow 2_{02}/5_{05} \rightarrow 4_{04}$ line ratio. 3σ errors are shown as grey lines, but can barely be distinguished from the measured values. When we estimate uncertainties, the errors on the fitted temperatures are also taken into account.

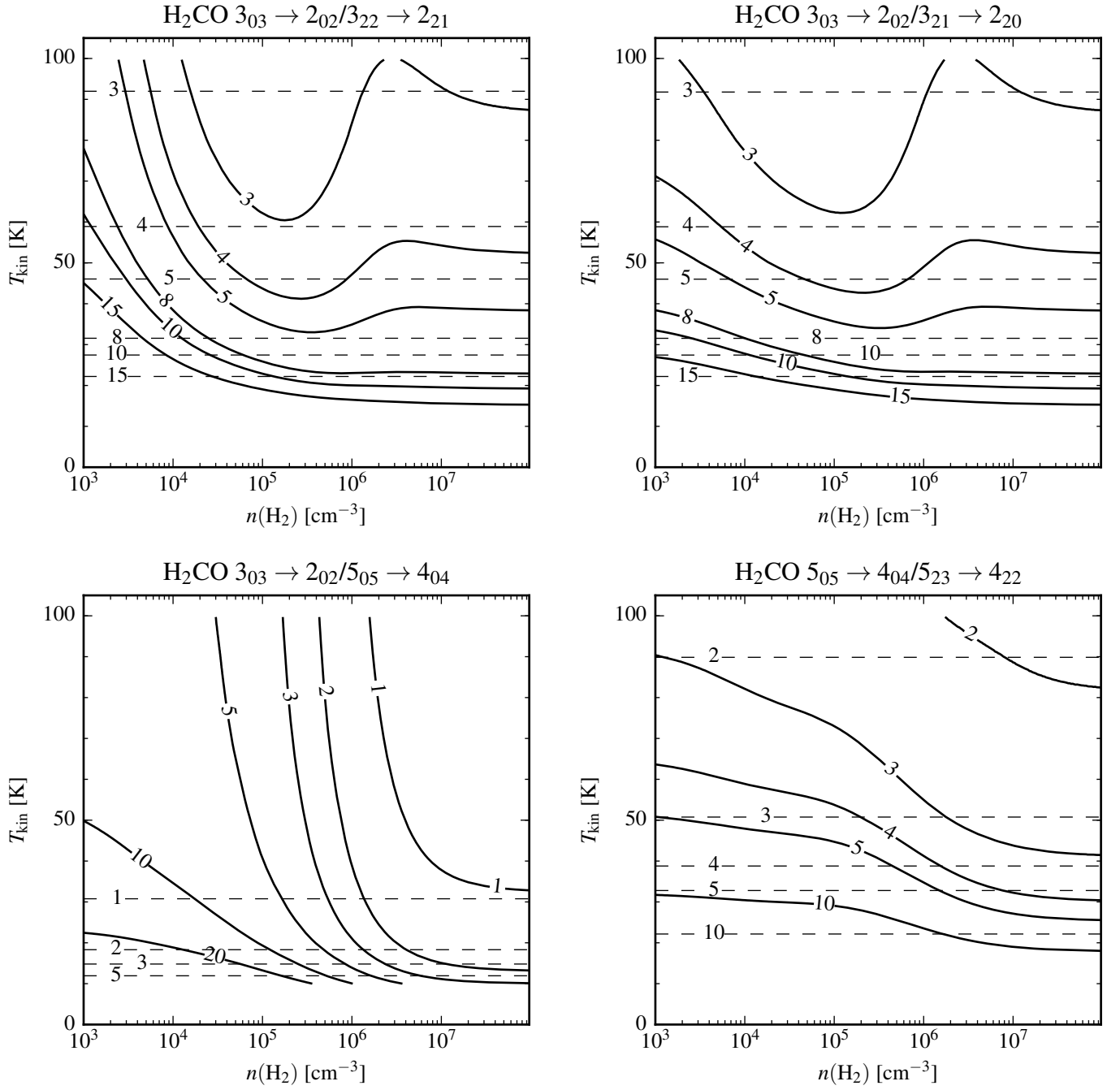


Fig. F.1. Ratios of H₂CO line intensities as modelled by RADEX (solid) and assuming LTE (dashed) with a column density $N = 10^{14} \text{ cm}^{-2}$ and line widths of 2 km s^{-1} .